

Novel Denoising Methods for Dynamic Positron Emission Tomography

By

John M. Floberg

A dissertation submitted in partial fulfillment
of the requirements for the degree of

Doctor of Philosophy
(Medical Physics)

at the

UNIVERSITY OF WISCONSIN-MADISON

2012

Date of final oral examination: 08/14/2012

This dissertation is approved by the following members of the Final Oral Committee:

Charles A. Mistretta, Professor, Medical Physics

Jamey P. Weichert, Associate Professor, Medical Physics

James E. Holden, Professor, Medical Physics

Bradley T. Christian, Associate Professor, Medical Physics

Lance T. Hall, Assistant Professor, Radiology

Robert D. Blank, Associate Professor, Endocrinology and Reproductive Physiology

Abstract

Positron emission tomography (PET) provides inherently quantitative information about physiological and molecular processes, endowing it with great clinical and research potential. This is particularly true of dynamic PET imaging. Unfortunately, PET, and especially dynamic PET, suffers from unfavorable noise properties, limiting it diagnostically and quantitatively. Denoising methods that improve image quality and thus increase diagnostic accuracy and improve estimates of quantitative parameters could be of great benefit, particularly if they are simple, accurate, and easily implemented on a wide range of PET tracer studies.

The aim of this thesis is to develop and evaluate two novel denoising methods for dynamic PET imaging: Highly constrained back-Projection-Local Reconstruction (HYPR-LR), which has recently been applied to dynamic PET data with promising results, and spatio-temporal expectation maximization (STEM) filtering, a newly developed 4-dimensional iterative filtering process.

An implementation of HYPR-LR is presented that provides the maximum amount of noise reduction that is possible without introducing any significant bias. This is accomplished using multiple time-dependent temporally summed composite images that account for the kinetics of the tracer being studied. The potential of HYPR-LR to improve dynamic PET imaging is demonstrated using phantom, simulated, and human data, with a focus on quantitative parametric images.

The newly proposed STEM filtering combines two well established image processing techniques: 4-dimensional Gaussian smoothing followed by EM deconvolution. In principle, this approach should provide substantial reductions in noise while introducing little bias. STEM

filtering is also evaluated using phantom, simulated, and human data, with a focus on parametric images.

The potential of HYPR-LR and STEM filtering to improve PET imaging of [I-124] labeled agents is also studied. [I-124] could be a valuable radionuclide for PET imaging, but its use is often limited by noise because of dosimetry concerns and relatively few decays by positron emission.

Finally, the impact of a more traditional means of controlling image noise at the cost of bias, varying the number of iterations performed during EM reconstruction, on the diagnosis of temporal lobe epilepsy is studied. This also serves as an illustration of how HYPR-LR and STEM filtering might be evaluated in a clinical context.

Acknowledgments

I feel like the graduate student it has taken a village to raise, and I have many people to thank for their help and support. First and foremost, I would like to thank my thesis committee members, who have really served as more of a mentorship committee. Chuck, you have had a profound impact on the way I think about medical physics from the time I arrived in the department. It was only a week or two after I found my desk that you gave the Cameron Lecture and encouraged the students in the audience to think about how they would have built the field if they started from scratch. I try and approach every problem I encounter with that perspective in mind. Jamey, you have shown me the importance of creativity, persistence, and enthusiasm in science, and I thank you for encouraging and indulging my ideas, and being there whether or not they worked out. Jim, thank you for teaching me to be so rigorous in all aspects of science, for pushing me when I needed to be pushed, and encouraging me when I needed encouragement. Brad, thank you for being so willing to help when I have needed you most, for leading the way on applying HYPR-LR to PET, and asking me hard questions that needed to be asked. Lance, thank you for giving me a clinical perspective on research that will be vital as I move forward, and thank you for the encouragement and guidance. Rob thank you for helping me grow as a physician and a scientist since the day that I interviewed.

Next, I would like to acknowledge my many sources of support for my endeavors: the NIH, Jamey, Lance and the Department of Radiology, and the Department of Medical Physics. I am so grateful for the investments so many have made in my future, and for the opportunity to pursue medical physics as an MD/PhD student.

I also need to thank all members of the Weichert lab, past and present: Joe, Mo, Sarah, Ben, Justin, Alice, and Matt. You have kept me entertained, challenged me, and have always been there as friends. Small animal imaging would not be there today without you all.

I would also like to recognize pretty much everyone who does PET research at UW: Jon Engle, Todd Barnhart, Jerry Nickles, Weibo Cai, Hao Hong, Yin Zhang, Dustin Wooten, Ansel Hilmer, Nick Vandehey, Alex Converse, Robert Jeraj, and the rest of the Cyclotron, Cai, Jeraj, and Christian Groups. I'd also like to recognize the MR and CT groups for their assistance and friendships. And I would especially like to thank Ian Rowland for his assistance. You have all helped make me a better scientist.

I also thank my MD/PhD classmates: Eric, Rene, Philip, Richard, Mike, Katie, and Chloe. You have all been true friends throughout my time in Madison. I am grateful to have you as companions in this long endeavor, and am looking forward to continuing it with you all.

And finally, but far from last or least, I would like to thank my family, especially my wonderful and beautiful fiancée Kristen, who is a constant source of support, strength, and wisdom in my life. My sisters, for being friends and confidants throughout all of my travels, adventures, and undertakings. And my parents, who have instilled in me a love for knowledge, and whose love and support have brought me to where I am today.

Table of Contents

Abstract.....	i
Acknowledgments	iii
Table of Contents	v
List of Figures.....	x
List of Tables	xiii
Chapter 1. Introduction	1
1.1 Noise Properties of PET Data	2
1.2 Current Denoising Methods	4
1.2.1 Spatial Filters	4
1.2.2 Wavelet Denoising	4
1.2.3 Iterative Reconstructions	5
1.2.4 4-Dimensional Reconstructions	6
1.2.5 Kinetic Analysis Methods for Reducing Variance	7
1.3 Potential for New PET Denoising Methods	7
1.4 Thesis Aims	8
References	9
Chapter 2. HYPR-LR Processing of Dynamic PET Data: Initial Application and Impact on Image Quality.....	14
2.1 Introduction.....	14
2.2 Chapter Aims	14
2.3 HYPR-LR Methodology.....	15
2.4 Methods	17
2.4.1 Derenzo Resolutions Phantom.....	17
2.4.2 Dual-Isotope Phantom	18
2.4.3 Digital Motion Phantom	19
2.4.4 [O-15]H ₂ O Human Study	20
2.5 Results.....	20
2.5.1 Derenzo Resolution Phantom	20
2.5.2 Dual-Isotope Phantom	21
2.5.3 Digital Motion Phantom	22
2.5.4 [O-15]H ₂ O Human Study	25
2.6 Discussion.....	25
2.7 Summary and Conclusions	26
References.....	27

Chapter 3. Optimized Implementation of HYPR-LR for Dynamic PET	28
3.1 Introduction.....	28
3.2 Chapter Aims	28
3.3 Theory and Methodology.....	29
3.4 Summary	33
References.....	33
Chapter 4. Improved Kinetic Analysis with Dynamic PET Data with HYPR-LR.....	35
4.1 Introduction.....	35
4.2 Chapter Aims	35
4.3 Methods	36
4.3.1 Creation of Numerical Phantoms.....	36
4.3.2 Acquisition of Real Data.....	38
4.3.3 HYPR-LR Processing and Smoothing.....	39
4.3.4 Kinetic Analysis.....	40
4.3.5 Data Evaluation.....	41
4.3.5.1 Bias and Variance in the Simulated Data	41
4.3.5.2 Evaluation of the Human Data.....	42
4.4 Results.....	43
4.4.1 Evaluation Bias and Variance in the Simulated Data	43
4.4.2 Evaluation of Human [C-11]PIB Data.....	47
4.5 Discussion.....	51
4.6 Conclusion	56
References.....	57
Chapter 5. Non-linear Spatio-temporal Filtering of Dynamic PET Data Using a Low-Pass Filter with Expectation-Maximization Deconvolution.....	59
5.1 Introduction.....	59
5.2 Chapter Aims	59
5.3 Theory.....	60
5.3.1 Initial Filtering	60
5.3.1 Filtering in the Image Frame Domain.....	61
5.3.3 Shift-Variant Convolution	62
5.3.4 EM Deconvolution.....	64
5.3.5 Filter Magnitude.....	64
5.3.6 Filter Parameter Selection.....	65
5.3.7 Effects of Temporal Sampling.....	67
5.4 Summary	68
References.....	68
Chapter 6. Evaluation of STEM and TEM Filtering	69
6.1 Chapter Aims	69
6.2 Methods	69

6.2.1 Dual-Isotope Phantom	69
6.2.2 [C-11]-Raclopride and [F-18]-FDOPA simulations	70
6.2.3 Kinetic analysis of simulated data	73
Human [C-11]Raclopride and [F-18]FDOPA scans.....	74
6.3 Results.....	75
6.3.1 Dual-Isotope Phantom	75
6.3.2 [C-11]Raclopride and [F-18]FDOPA simulations.....	77
6.3.3 Kinetic Analysis of [C-11]Raclopride and [F-18]FDOPA simulations.....	79
6.3.4 [C-11]Raclopride and [F-18]FDOPA Human Data.....	81
6.4 Discussion.....	85
6.5 Conclusions.....	88
References.....	89
Chapter 7. Application of HYPR-LR and STEM Filtering to [I-124] PET Imaging.	91
7.1 Introduction.....	91
7.2 Chapter Aims	93
7.3 Methods	93
7.3.1 HYPR-LR for Longitudinal [I-124]NM404 Scanning	93
7.3.2 HYPR-LR for Radiation Dose Reduction.....	95
7.3.3 STEM Filtering for Improved Image Quality, Reduced Scan Durations, and Reduced Radiation Dose.....	96
7.3.3.1 STEM Filtering [I-124] Phantom Study	96
7.3.3.2 STEM Filtering of [I-124]NM404 Human Brain Tumor Studies.....	98
7.4 Results.....	99
7.4.1. HYPR-LR for Longitudinal [I-124]NM404 Scanning	99
7.4.2 HYPR-LR for Radiation Dose Reduction.....	100
7.4.3 STEM Filtering [I-124] Phantom Results.....	103
7.4.4 STEM Filtering of [I-124]NM404 Human Brain Tumor Studies.....	105
7.5 Discussion.....	106
7.5.1 HYPR-LR Processing of [I-124]NM404 Studies	106
7.5.2 STEM Filtering of [I-124]NM404 Studies	107
7.5.3 Limitations of HYPR-LR Processing and STEM Filtering for Improving [I-124] Studies.....	109
7.6 Conclusions.....	109
References.....	110
Chapter 8. Impact of Expectation-Maximization Reconstru-ction Iterations on the Diagnosis of Temporal Lobe Epilepsy with PET	113
8.1 Introduction.....	113
8.2 Chapter Aims	114
8.3 Methods	115
8.3.1 Subject Selection.....	115
8.3.2 PET Image Acquisition and Reconstruction Protocols.....	117

8.3.3 Reader Study Design and Analysis.....	119
8.4 Results.....	120
8.4.1 Subject Selection.....	120
8.4.2 Reader Study Results.....	121
8.5 Discussion.....	124
8.6 Conclusions.....	127
References.....	127
Chapter 9. Conclusions and Future Directions.....	130
9.1 HYPR-LR Processing.....	130
9.2 STEM Filtering.....	131
9.3 Application of HYPR-LR Processing and STEM Filtering to [I-124] PET Imaging.....	131
9.4 Limitations of the Evaluation of HYPR-LR and STEM.....	132
9.5 Impact of EM Reconstruction Iterations on Temporal Lobe Epilepsy Diagnosis.....	133
9.6 Future Work.....	133
References.....	134
Appendix A. Kinetic Analysis Methods for PET Tracer Data.....	135
A.1 Kinetic Analysis of Tracers with Reversible Binding Behavior.....	135
A.1.1 Logan Graphical Analysis.....	137
A.1.2 Receptor Parametric Mapping.....	138
A.2 Irreversible Tracers.....	139
A.2.1 Patlak Graphical Analysis.....	139
References.....	140
Appendix B. A Kinetic Model for the Cancer Imaging and Therapy Agent NM404..	141
B.1 Introduction.....	141
B.2 Methods.....	142
B.2.1 Animal Preparation.....	142
B.2.2 Imaging Procedure.....	142
B.2.3 Data Analysis and Kinetic Modeling.....	143
B.2.4 Akaike Weights.....	144
B.3 Results.....	144
B.4 Discussion and Conclusions.....	145
References.....	148
Appendix C. Evaluation of the Diapetuc Agent NM404 in a Rat Glioma Model with PET and MRI.....	149
C.1 Introduction.....	149
C.2 Methods.....	150
C.2.1 Cancer Model.....	150
C.2.2 MRI Imaging.....	150

C.2.3 PET Imaging	150
C.2.3 Histology	151
C.3 Results	152
C.3.1 [I-124]NM404 Uptake versus CE-MRI	152
C.3.2 [I-124]NM404 versus [F-18]FLT Uptake	153
C.3.3 Longitudinal Scanning with [I-124]NM404	153
C.3.4 Histology	153
C.4 Discussion and Conclusions	155
References	157

List of Figures

Figure 1.1. An illustration of the frequencies that characterize signal and noise in PET images.	3
Figure 2.1. The Derenzo phantom used to study the effects of HYPR-LR on spatial resolution and image noise.....	21
Figure 2.2. The dual-isotope phantom used to study the potential of HYPR-LR to improve the estimation of simple kinetic parameters, and to study the effects of composite duration and kernel size on noise.....	22
Figure 2.3. An illustration of the effects of motion on HYPR-LR processing	23
Figure 2.4. An illustration of the effect of changing object size on HYPR-LR processing.	23
Figure 2.5. The human [O-15]H ₂ O study used to illustrate the reductions in noise possible with HYPR-LR in dynamic PET studies with high noise.....	24
Figure 3.1 Illustration of the errors HYPR-LR can cause.....	29
Figure 3.2 [C-11]PIB time activity curves (TACs) for regions of the brain from a [C-11]PIB positive human study, and the ratio of the activities of neighboring regions at each time point.	31
Figure 4.1. Evaluation of HYPR-LR with a noise-free simulated phantom	44
Figure 4.2. Parametric images of the noise-free simulated data generated with either the reference region Logan graphical method or RPM2.....	44
Figure 4.3. The relationship between bias and the COV in the simulated data for individual time frames, Logan parametric images, and RPM2 parametric images	46
Figure 4.4. An illustrative example from a human [C-11]PIB dataset showing the effects of HYPR-LR processing on parametric images.....	48
Figure 4.5. Bias in the [C-11]PIB human data.....	49
Figure 4.6. Voxel BP _{ND} values obtained with the Logan graphical method and RPM2 plotted against each other from a representative [C-11]PIB study	50
Figure 5.1. An illustration of the image frame domain component of STEM and TEM filtering.	61
Figure 5.2. The magnitude of the effective filter in frame frequency space.....	65

Figure 5.3. The spectral properties of an example [C-11]raclopride TAC and frame.....	66
Figure 5.4. The effects of temporal sampling on the ability of STEM filtering to restore the original signal.....	67
Figure 6.1. The results of the dual-isotope phantom.....	76
Figure 6.2. Example TACs and the bias-COV tradeoff seen with STEM filtering.....	77
Figure 6.3. Example TACs and the bias-COV tradeoff seen with TEM filtering.....	78
Figure 6.4. A single time frame from the human [C-11]raclopride study evaluated ($t = 32.5$ minutes), and example TACs from large ROIs of the striatum and frontal cortex.....	81
Figure 6.5. A single time frame from the human [F-18]FDOPA study evaluated ($t = 45$ minutes), and example TACs from large ROIs of the striatum and frontal cortex.....	82
Figure 6.6. RPM2 and Logan parametric images of the human [C-11]raclopride study, and Patlak parametric images of the human [F-18]FDOPA study.....	83
Figure 6.7. The inappropriately high or negative Logan BP_{ND} values following STEM filtering are due to TACs that start to flatten or trend positive at the end of the study because of the very high noise in the HRRT data.....	84
Figure 7.1. The Derenzo resolution phantom used to evaluate STEM filtering of [I-124] data.....	96
Figure 7.2. Example time frame images and TACs from the extended imaging time-point [I-124]NM404 study.....	100
Figure 7.3. Results from the radiopharmaceutical dose reduction study.....	101
Figure 7.4. Evaluation of spatial resolution and the temporal accuracy following STEM filtering.....	102
Figure 7.5. The NPS of the FBP and OSEM/MAP reconstructions before and after STEM filtering with 5 and 10 iterations.....	103
Figure 7.6. Example human images of [I-124]NM404 from 2 brain tumor patients.....	104
Figure 7.7. Tumor TACs from the 3 patients studied and bias and COV from the last frame ($t = 48$ hours) of each study.....	105
Figure 8.1. Example images of the reconstructions studied.....	118

Figure 8.2. Patient population diagnostic characteristics.....	121
Figure 8.3. Surgical candidacy ROC curves	122
Figure 8.4. The sensitivity of [F-18]FDG PET for predicting a positive surgical outcome for the two OSEM reconstructions studied	123
<p>Figure A.1. The kinetic models used in this thesis, including the two-tissue compartment model (a), the simplified one-tissue compartment model (b), and the model for the reference tissue that is used as an input in all the simplified analysis methods presented in this work (c).136</p>	
Figure B.1. A visual illustration of the pharmacokinetics of [I-124]-NM404.....	145
Figure B.2. Representative curves for image derived plasma input functions, measured tumor activities, and one and two-tissue compartment fits.	146
Figure C.1. A comparison of [I-124]NM404 uptake and gadolinium enhancement.....	152
Figure C.2. Comparison of [I-124]NM404 and [F-18]FLT uptake.....	154
Figure C.3. Longitudinal uptake of [I-124]NM404.....	154
Figure C.4. Example histologic specimen.	155

List of Tables

Table 4.1. A summary of HYPR-LR terminology used frequently in this chapter.....	39
Table 4.2. The mean and range of Pearson correlation coefficients obtained from a linear fit to the voxel-by-voxel comparisons of the reference region Logan method and RPM2 for each of the 8 human [C-11]PIB datasets.	51
Table 6.1. The average bias and COV of all voxels in the striatum of the parametric images created from the simulated data	80
Table 8.1. Reconstruction parameters for each scanner used in the epilepsy reconstruction study.	118
Table 8.2. The areas under the ROC curves from each reconstruction in the epilepsy study for the individual readers and with their results combined.	122
Table B.1. Appropriateness of the one and two-tissue compartment models for the kinetics of [I-124]NM404 as assessed by the AIC.	146
Table B.2. Rate constants from fits of the [I-124]NM404 data to the two-tissue compartment model.....	147

Chapter 1. Introduction

Positron emission tomography (PET) has tremendous potential as an imaging modality for both preclinical research and clinical practice because of its ability to provide quantitative information about biological processes *in vivo* and noninvasively. This is particularly true of dynamic PET imaging, which provides a means of measuring physiologically relevant parameters from the analysis of a radiotracer's dynamic behavior, for example the rate at which the tracer is metabolized or the availability of targeted receptors (Phelps *et al* 1979, Phelps *et al* 1982). The ability to obtain biological and molecular information through imaging has provided valuable insights into disease processes that have changed medical practice in a number of fields, most notably oncology, cardiology and neurology. PET imaging has also created new research opportunities in these fields, providing information that cannot be otherwise obtained noninvasively.

Unfortunately, PET data are limited by noise because of the finite amount of radiation that can acceptably be given to human subjects. This limits the number of radioactive decays that can be detected, resulting in high noise variance. Noise is especially limiting for dynamic PET imaging, as time frames must be of limited duration to accurately capture a tracer's kinetic behavior.

The noisy nature of PET data impacts both the quality of the images, which is critically important for accurate clinical diagnosis, and the quantitative kinetic analysis of the data. Noise impacts image quality by limiting the detectability of objects, dependent on objects' contrast and size. This is known as the Rose model, and holds true for both human observers and electronic imaging systems (Rose 1974). The spatial resolution of PET images is also limited by noise, as

PET scanners with high spatial resolution will have a greater number of detector elements and will therefore detect fewer positron decays per detector element (Wienhard *et al* 2002). Any gain in spatial resolution may therefore be offset by higher image noise. Noise in dynamic PET data affects quantitative kinetic analysis in two ways. First, for all kinetic analysis methods, noise in the dynamic PET data will result in variance in the estimated kinetic parameters. Second, some methods, namely the Logan graphical method, have a noise-dependent bias (Logan 2003, Slifstein and Laruelle 2000).

Strategies that reduce noise in PET data are thus of great potential value as they could both improve the accuracy of clinical diagnoses and reduce the variance of quantitative parameters estimated from the data. Improved kinetic parameter estimates could in turn improve the reliability and sensitivity of studies that utilize PET to detect changes in biological processes *in vivo*. Improved accuracy in diagnostic images and quantitative parameters could in turn increase the utility of PET, broadening its scope while minimizing the amount of radiation given to subjects.

1.1 Noise Properties of PET Data

Many of the approaches used to reduce noise in PET data take advantage of the fact that the underlying signal in PET images is relatively low frequency in both space and time, but noise is not. A PET image can be described as a signal with added noise:

$$y = x + \varepsilon \tag{1.1}$$

where y is the measured value of an image voxel, x is the true underlying signal, and ε is the added noise, which can be approximated as Gaussian with a mean value of zero and a standard deviation that will be scaled by the amount of activity in the object being imaged. The additive

noise will be powered at all frequencies as each measurement in a PET dataset will be statistically independent of all other measurements. In some reconstructions, for example filtered back-projection (FBP) with a ramp filter, noise will actually have excess power in the high spatial frequencies. The spectral characteristics of noise are thus very dissimilar to the relatively low spatial frequencies that characterize the signal (Figure 1.1). The same is true in the time domain, as time activity curves (TACs) from PET data tend to be relatively smooth and are therefore dominated by low frequencies.

The difference in the frequency characteristics of signal and noise is a compelling means of differentiating them from each other. However, in real PET data where the truth is unknown, it is not a trivial task to identify and suppress noise without altering the signal. Given that one of the greatest strengths of PET imaging is its ability to provide quantitative information, it is of vital importance that any method for reducing noise preserve the fidelity of the signal as best as possible. There have been many proposed means of reducing noise in PET data, each of

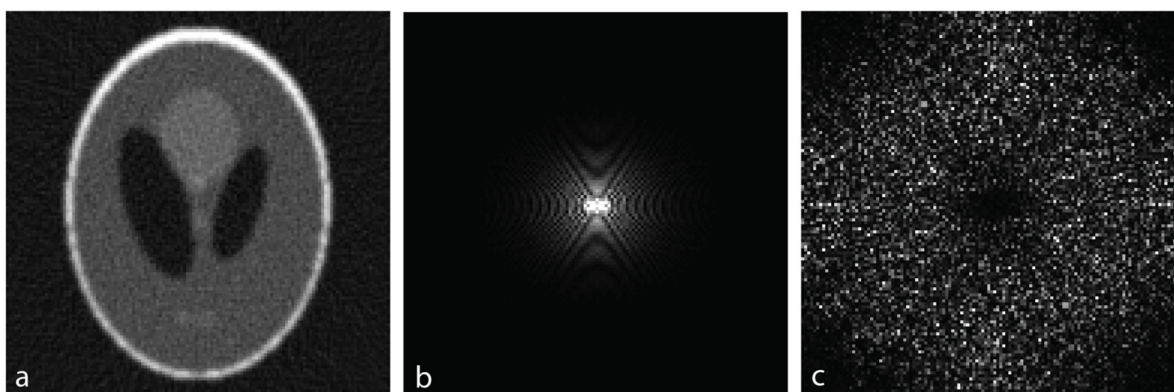


Figure 1.1. An illustration of the frequencies that characterize signal and noise in PET images. For an example image reconstructed with FBP with Poisson noise added in sinogram space (a), the underlying signal is dominated by relatively low spatial frequencies (b), and the noise power spectrum is overpowered at high spatial frequencies (c). The difference in the spectral characteristics of the signal and noise is a compelling means of reducing noise.

which has strengths and weaknesses in terms of the degree to which they suppress noise, the accuracy of the resulting data for a given level of noise suppression, and the simplicity of their implementation.

1.2 Current Denoising Methods

1.2.1 Spatial Filters

One of the simplest, and still most widely used, means of reducing noise in PET data is simply filtering the data in space. This can alternatively be thought of as spatial averaging or as filtering in the spatial frequency domain. There are a number of approaches to spatial filtering, the simplest of which is simply spatially smoothing the data. There are also several other spatial filtering methods that have been developed, such as the median filter, Wiener filters, the Metz filter, and the Herholz filter (Miller and Sampathkumaran 1982, King *et al* 1983, King *et al* 1988, Varga *et al* 1997, Herholz 1988). All of these methods rest on the principle that the power of the frequencies that represent signal and noise can be differentiated. While all of these methods can be very effective at reducing noise, they invariably suppress frequencies important to the signal, resulting in a loss of spatial resolution or other bias. Nevertheless, spatially filtering the data, particularly simple spatial smoothing, remains one of the most used means of reducing noise in PET images.

1.2.2 Wavelet Denoising

PET data can also be filtered in the wavelet domain. Transforming data to a wavelet domain gives a representation of frequency and spatial (and/or temporal) information simultaneously. Wavelet transforms can therefore be thought of as localizing frequencies in space and time. This is a potential advantage for non-stationary signals, such as those in PET, where the frequencies

that dominate the signal change in space and time. Wavelet transforms will therefore compress the signal more than a non-localizing transform (e.g. a Fourier transform). However, noise will still be dispersed (Donoho and Johnstone 1994, Unser and Aldroubi 1996). This allows for easier identification and suppression of noise. The most extensive work of applying wavelet denoising PET data has been done by Turkheimer *et al.* (Turkheimer *et al* 1999, Turkheimer *et al* 2000, Turkheimer *et al* 2003, Turkheimer *et al* 2003). This body of work and other studies utilizing wavelets have demonstrated significant improvements in dynamic PET data following wavelet denoising, with an emphasis on improvements in quantitative parameter estimates (Lin *et al* 2001, Cselenyi *et al* 2002). However, the proper application of wavelet denoising to dynamic PET data is relatively complicated and difficult to implement. A filter must still be designed to suppress wavelet coefficients associated with noise and preserve those associated with the signal; this is not a trivial task.

1.2.3 Iterative Reconstructions

Iterative reconstructions have had one of the greatest impacts on reducing noise in PET images. In particular, ordered subset expectation-maximization (OSEM) reconstructions are now widely used in both clinical practice and research (Shepp and Vardy 1982, Hudson and Larkin 1994). OSEM reconstruction has been shown to have superior noise properties to FBP (Barrett *et al* 1994, Wilson *et al* 1994, Wilson and Tsui 1993), and the improvements in diagnostic accuracy gained with OSEM have been demonstrated in many imaging tasks (Gilland *et al* 1992, Wells *et al* 1999, Wells *et al* 2000, LaCroix *et al* 2000, Gifford *et al* 2000). While the use of OSEM reconstruction has become standard practice and has undoubtedly improved clinical diagnosis, there is still a trade-off between bias and variance seen with the number of iterations performed that can influence measurements made from PET data (Jaskowiak *et al* 2005). In addition,

OSEM reconstructions can still be very noisy, particularly when activity levels are low or scanning times are short.

Maximum a posteriori (MAP) reconstructions have also proven to be an effective means of reducing noise in reconstructed PET images (Miller and Butler 1993). Unlike OSEM, MAP reconstructions impose an explicit penalty on the degree to which neighboring voxels vary. Therefore, they can degrade spatial resolution, similar to simple spatial smoothing (Nuyts and Fessler 2003). Nevertheless, their utility has been demonstrated in a number of applications (Qi and Leahy 1999, Cheng *et al* 2012).

1.2.4 4-Dimensional Reconstructions

In addition to the iterative reconstructions already described, a number of reconstruction methods have been developed that take advantage of information in the time domain to reduce noise (Rahmim *et al* 2009). Some strategies include smoothing between time-frames within reconstruction (Lalush and Tsui 1998, Walledge *et al* 2004), principal component analysis (Wernick *et al* 1999, Narayanan *et al* 1999), and the direct reconstruction of parametric images from sinograms (Carson and Lange 1985, Kamasak *et al* 2005, Tsoumpas *et al* 2008, Meikle *et al* 1998). While 4-dimensional reconstructions are an active field of research and show much promise, they must make some assumption about the temporal behavior of a tracer that may not be true, at least for some parts of the image object. For example, these reconstructions often make assumptions about a kinetic model that the tracer follows, the degree to which neighboring frames will be similar, or the measured signal components that will be most important to the true (noise-free) signal.

1.2.5 Kinetic Analysis Methods for Reducing Variance

Because the primary motivation of acquiring dynamic PET data is to perform kinetic analysis, there are also a number of analysis methods that have been developed to minimize the variance of calculated kinetic parameters. Unlike 4-dimensional reconstructions, these methods still use data acquired as individual time-frames. They do, however, use assumptions about the expected temporal behavior of PET tracers, or impose limits on the data based on theoretical truths, to minimize the effects of noise present in the measured data. These strategies include the use of temporal basis functions (Koeppel *et al* 1985, Gunn *et al* 1997, Gunn *et al* 2001, Gunn *et al* 2002), fitting the data in an alternative domain (e.g. the wavelet domain) (Cselenyi *et al* 2002), and using initial results to fix parameters that theoretically should not vary at different locations in the image object (e.g. the reference region efflux constant, k_2^{REF} , in simplified models can be fixed rather than being fit at each voxel, (Wu and Carson 2002). These strategies have proven effective in a number of imaging tasks (Yaqub *et al* 2008, Cselenyi *et al* 2006). However, their assumptions can limit their use and accuracy, and their implementation can be more complicated than simple graphical methods, requiring more initial parameters to be defined. And, although these methods improve the variance of calculated parameters, very noisy data will still produce parameters with high variance.

1.3 Potential for New PET Denoising Methods

Many methods have been developed to reduce noise in PET data, and an overview has been presented here. Each of these methods has proven effective, but each has limitations. These limitations typically arise from assumptions that are made about the nature of the data in an attempt to distinguish underlying signal from noise (Equation 1.1). For example, filtering

methods must make an assumption, implicit or explicit, about what components of the measured data are most important to the signal. Although these assumptions may be based upon reasonable premises, they are not necessarily true. In addition, more sophisticated methods of denoising can be limited by the complexity of their implementation.

Potential exists for the development of novel denoising methods, particularly methods that are data driven in the sense that they attempt to distinguish signal from noise in a manner that is specific to the data being studied. New denoising methods could also prove useful if they are easy to implement, can be applied across a wide range of PET imaging applications, and can complement existing and established denoising methods. Denoising methods that possess these traits will be much more likely to have a meaningful impact on PET image quality and quantification in both clinical and research applications, and may have the potential to broaden the scope of PET imaging.

1.4 Thesis Aims

The primary purpose of this work is to develop two novel denoising methods for dynamic PET data: Highly constrained back-Projection-Local Reconstruction (HYPR-LR) (Mistretta *et al* 2006, Johnson *et al* 2008) and spatiotemporal expectation-maximization (STEM) filtering. These methods attempt to fulfill the criteria of being data driven, easy to implement, applicable to a wide range of dynamic PET studies, and complementary to other denoising techniques. This work also aims to rigorously evaluate the performance of these algorithms on dynamic PET tracer data, and to show how these new methods and more traditional methods might be evaluated in a clinical context.

The specific aims of this thesis are:

1. To develop an implementation of HYPR-LR that can be tailored to different PET tracer behaviors, or even individual studies such that it provides the maximum amount of noise reduction possible without introducing any bias.
2. To develop a novel 4-dimensional filtering method that combines Gaussian smoothing with expectation maximization (EM) deconvolution (Richardson 1972, Lucy 1974).
3. To evaluate the potential of HYPR-LR processing and STEM filtering to improve the kinetic analysis of PET tracer data. In particular, to improve parametric images of quantitative parameters. This is done in separate chapters for HYPR-LR and STEM filtering.
4. To evaluate the potential of HYPR-LR and STEM filtering to improve the longitudinal imaging (i.e. several day time-course) of [I-124] labeled tracers.
5. To evaluate a more traditional denoising method, altering the number of iterations performed in EM reconstruction, in the context of a real diagnostic imaging task. This is intended to serve as an example of how both established and new denoising methods might be evaluated in a clinical context.

References

- Barrett, H H, Wilson, D W and Tsui, B M 1994 Noise properties of the EM algorithm: I. Theory *Phys. Med. Biol.* **39** 5 833-46
- Carson, R E and Lange, K 1985 The EM parametric image reconstruction algorithm *J. Am. Stat. Assoc.* **80** 20,21-22
- Cheng, J C, Shoghi, K and Laforest, R 2012 Quantitative accuracy of MAP reconstruction for dynamic PET imaging in small animals *Med. Phys.* **39** 2 1029-41

Cselenyi, Z, Olsson, H, Farde, L and Gulyas, B 2002 Wavelet-aided parametric mapping of cerebral dopamine D2 receptors using the high affinity PET radioligand [^{11}C]FLB 457 *Neuroimage* **17** 1 47-60

Cselenyi, Z, Olsson, H, Halldin, C, Gulyas, B and Farde, L 2006 A comparison of recent parametric neuroreceptor mapping approaches based on measurements with the high affinity PET radioligands [^{11}C]FLB 457 and [^{11}C]WAY 100635 *Neuroimage* **32** 4 1690-708

Donoho, D L and Johnstone, I M 1994 Ideal spatial adaptation by wavelet shrinkage *Biometrika* **81** 425-55

Gifford, H C, King, M A, Wells, R G, Hawkins, W G, Narayanan, M V and Pretorius, P H 2000 LROC analysis of detector-response compensation in SPECT *IEEE Trans. Med. Imaging* **19** 5 463-73

Gilland, D R, Tsui, B M, Metz, C E, Jaszczak, R J and Perry, J R 1992 An evaluation of maximum likelihood-expectation maximization reconstruction for SPECT by ROC analysis *J. Nucl. Med.* **33** 3 451-7

Gunn, R N, Gunn, S R and Cunningham, V J 2001 Positron emission tomography compartmental models *J. Cereb. Blood Flow Metab.* **21** 6 635-52

Gunn, R N, Gunn, S R, Turkheimer, F E, Aston, J A and Cunningham, V J 2002 Positron emission tomography compartmental models: a basis pursuit strategy for kinetic modeling *J. Cereb. Blood Flow Metab.* **22** 12 1425-39

Gunn, R N, Lammertsma, A A, Hume, S P and Cunningham, V J 1997 Parametric imaging of ligand-receptor binding in PET using a simplified reference region model *Neuroimage* **6** 4 279-87

Herholz, K 1988 Non-stationary spatial filtering and accelerated curve fitting for parametric imaging with dynamic PET *Eur. J. Nucl. Med.* **14** 9-10 477-84

Hudson, H M and Larkin, R S 1994 Accelerated image reconstruction using ordered subsets of projection data *IEEE Trans. Med. Imaging* **13** 4 601-9

Jaskowiak, C J, Bianco, J A, Perlman, S B and Fine, J P 2005 Influence of reconstruction iterations on ^{18}F -FDG PET/CT standardized uptake values *J. Nucl. Med.* **46** 3 424-8

Johnson, K M, Velikina, J, Wu, Y, Kecskemeti, S, Wieben, O and Mistretta, C A 2008 Improved waveform fidelity using local HYPR reconstruction (HYPR LR) *Magn. Reson. Med.* **59** 3 456-62

Kamasak, M E, Bouman, C A, Morris, E D and Sauer, K 2005 Direct reconstruction of kinetic parameter images from dynamic PET data *IEEE Trans. Med. Imaging* **24** 5 636-50

- King, M A, Doherty, P W, Schwinger, R B and Penney, B C 1983 A Wiener filter for nuclear medicine images *Med. Phys.* **10** 6 876-80
- King, M A, Penney, B C and Glick, S J 1988 An image-dependent Metz filter for nuclear medicine images *J. Nucl. Med.* **29** 12 1980-9
- Koepppe, R A, Holden, J E and Ip, W R 1985 Performance comparison of parameter estimation techniques for the quantitation of local cerebral blood flow by dynamic positron computed tomography *J. Cereb. Blood Flow Metab.* **5** 2 224-34
- LaCroix, K J, Tsui, B M, Frey, E C and Jaszczak, R J 2000 Receiver operating characteristic evaluation of iterative reconstruction with attenuation correction in ^{99m}Tc-sestamibi myocardial SPECT images *J. Nucl. Med.* **41** 3 502-13
- Lalush, D S and Tsui, B M 1998 Block-iterative techniques for fast 4D reconstruction using a priori motion models in gated cardiac SPECT *Phys. Med. Biol.* **43** 4 875-86
- Lin, J W, Laine, A F and Bergmann, S R 2001 Improving PET-based physiological quantification through methods of wavelet denoising *IEEE Trans. Biomed. Eng.* **48** 2 202-12
- Logan, J 2003 A review of graphical methods for tracer studies and strategies to reduce bias *Nucl. Med. Biol.* **30** 8 833-44
- Lucy, L B 1974 An iterative technique for the rectification of observed distributions *AJ* **79** 6 745-754
- Meikle, S R, Matthews, J C, Cunningham, V J, Bailey, D L, Livieratos, L, Jones, T and Price, P 1998 Parametric image reconstruction using spectral analysis of PET projection data *Phys. Med. Biol.* **43** 3 651-66
- Miller, M I and Butler, C S 1993 3-D maximum a posteriori estimation for single photon emission computed tomography on massively-parallel computers *IEEE Trans. Med. Imaging* **12** 3 560-5
- Miller, T R and Sampathkumaran, K S 1982 Digital filtering in nuclear medicine *J. Nucl. Med.* **23** 1 66-72
- Mistretta, C A, Wieben, O, Velikina, J, Block, W, Perry, J, Wu, Y, Johnson, K and Wu, Y 2006 Highly constrained backprojection for time-resolved MRI *Magn. Reson. Med.* **55** 1 30-40
- Narayanan, M V, King, M A, Soares, E J, Byrne, C L, Pretorius, P H and Wernick, M N 1999 Application of the Karhunen-Loeve transform to 4D reconstruction of cardiac gated SPECT images *IEEE Trans Nucl Sci* **46** 4 1001,1002-1008

- Nuyts, J and Fessler, J A 2003 A penalized-likelihood image reconstruction method for emission tomography, compared to postsmoothed maximum-likelihood with matched spatial resolution *IEEE Trans. Med. Imaging* **22** 9 1042-52
- Phelps, M E, Huang, S C, Hoffman, E J, Selin, C, Sokoloff, L and Kuhl, D E 1979 Tomographic measurement of local cerebral glucose metabolic rate in humans with (F-18)2-fluoro-2-deoxy-D-glucose: validation of method *Ann. Neurol.* **6** 5 371-88
- Phelps, M E, Mazziotta, J C and Huang, S C 1982 Study of cerebral function with positron computed tomography *J. Cereb. Blood Flow Metab.* **2** 2 113-62
- Qi, J and Leahy, R M 1999 A theoretical study of the contrast recovery and variance of MAP reconstructions from PET data *IEEE Trans. Med. Imaging* **18** 4 293-305
- Rahmim, A, Tang, J and Zaidi, H 2009 Four-dimensional (4D) image reconstruction strategies in dynamic PET: beyond conventional independent frame reconstruction *Med. Phys.* **36** 8 3654-70
- Richardson, W H 1972 Bayesian-Based Iterative Method of Image Restoration *JOSA* **62** 1 55-59
- Rose, A 1974 *Vision: Human and Electronic* (New York: Plenum Press)
- Shepp, L A and Vardy, Y 1982 Maximum Likelihood Reconstruction for Emission Tomography *IEEE Trans. Med. Imaging* **1** 113
- Slifstein, M and Laruelle, M 2000 Effects of statistical noise on graphic analysis of PET neuroreceptor studies *J. Nucl. Med.* **41** 12 2083-8
- Tsoumpas, C, Turkheimer, F E and Thielemans, K 2008 Study of direct and indirect parametric estimation methods of linear models in dynamic positron emission tomography *Med. Phys.* **35** 4 1299-309
- Turkheimer, F E, Aston, J A, Banati, R B, Riddell, C and Cunningham, V J 2003 A linear wavelet filter for parametric imaging with dynamic PET *IEEE Trans. Med. Imaging* **22** 3 289-301
- Turkheimer, F E, Banati, R B, Visvikis, D, Aston, J A, Gunn, R N and Cunningham, V J 2000 Modeling dynamic PET-SPECT studies in the wavelet domain *J. Cereb. Blood Flow Metab.* **20** 5 879-93
- Turkheimer, F E, Brett, M, Visvikis, D and Cunningham, V J 1999 Multiresolution analysis of emission tomography images in the wavelet domain *J. Cereb. Blood Flow Metab.* **19** 11 1189-208

Turkheimer, F E, Hinz, R and Cunningham, V J 2003 On the undecidability among kinetic models: from model selection to model averaging *J. Cereb. Blood Flow Metab.* **23** 4 490-8

Unser, M and Aldroubi, A 1996 A review of wavelets in biomedical applications *Proceedings of the IEEE* **84** 4 626,627-638

Varga, J, Bettinardi, V, Gilardi, M C, Riddell, C, Castiglioni, I, Rizzo, G and Fazio, F 1997 Evaluation of pre- and post-reconstruction count-dependent Metz filters for brain PET studies *Med. Phys.* **24** 9 1431-40

Walledge, R J, Manavaki, R, Honer, M and Reader, A J 2004 Inter-frame filtering for list-mode EM reconstruction in high-resolution 4-D PET *IEEE Trans Nucl Sci* **51** 3 705,706-711

Wells, R G, King, M A, Simkin, P H, Judy, P F, Brill, A B, Gifford, H C, Licho, R, Pretorius, P H, Schneider, P B and Seldin, D W 2000 Comparing filtered backprojection and ordered-subsets expectation maximization for small-lesion detection and localization in ⁶⁷Ga SPECT *J. Nucl. Med.* **41** 8 1391-9

Wells, R G, Simkin, P H, Judy, P F and King, M A 1999 Maximizing the detection and localization of Ga-67 tumors in thoracic SPECT MLEM(OSEM) reconstructions *IEEE Trans Nucl Sci* **46** 4 1191-8

Wernick, M N, Infusino, E J and Milosevic, M 1999 Fast spatio-temporal image reconstruction for dynamic PET *IEEE Trans. Med. Imaging* **18** 3 185-95

Wienhard, K *et al* 2002 The ECAT HRRT: performance and first clinical applications at the new High Resolution Research Tomograph *IEEE Trans Nucl Sci* **49** 104-10

Wilson, D W and Tsui, B M 1993 Noise Properties of Filtered-Backprojection and ML-EM Reconstructed Emission Tomographic-Images *IEEE Trans Nucl Sci* **40** 1198-203

Wilson, D W, Tsui, B M and Barrett, H H 1994 Noise properties of the EM algorithm: II. Monte Carlo simulations *Phys. Med. Biol.* **39** 5 847-71

Wu, Y and Carson, R E 2002 Noise reduction in the simplified reference tissue model for neuroreceptor functional imaging *J. Cereb. Blood Flow Metab.* **22** 12 1440-52

Yaqub, M, Tolboom, N, Boellaard, R, van Berckel, B N, van Tilburg, E W, Luurtsema, G, Scheltens, P and Lammertsma, A A 2008 Simplified parametric methods for [¹¹C]PIB studies *Neuroimage* **42** 1 76-86

Chapter 2. HYPR-LR Processing of Dynamic PET Data: Initial Application and Impact on Image Quality

2.1 Introduction

The first novel denoising method for dynamic positron emission tomography (PET) explored in this thesis is Highly constrained back-PRojection (HYPR). HYPR is a family of image reconstruction and post-processing algorithms that have made a dramatic impact on magnetic resonance angiography (MRA), allowing for under sampling factors on the order of several hundred fold and dramatic signal-to-noise ratio (SNR) improvements in dynamic datasets (Mistretta *et al* 2006, Johnson *et al* 2008, Wu *et al* 2009). The central idea of HYPR is to estimate individual frames in a dynamic study by weighting a temporally summed composite image. In the ideal case, individual frames will take on the noise properties of the composite image. It is the potential improvement in SNR that makes HYPR an attractive tool for other imaging modalities, and the post-processing version, HYPR-LR (for Local Reconstruction), has recently been applied to positron emission tomography (PET) with promising results (Christian *et al* 2010).

2.2 Chapter Aims

The aim of this chapter is to introduce the HYPR-LR methodology for dynamic PET imaging and generally illustrates the algorithm's impact on image quality measures first studied in the initial work applying HYPR-LR to PET (Christian *et al* 2010). In particular, the effects HYPR-LR has on image noise, resolution, time-activity curves (TACs), and the calculation of simple kinetic parameters are explored. This is done with phantom data. Human [O-15]H₂O data is also studied to evaluate the potential impact of HYPR-LR in a study with very high levels of noise.

Later chapters propose an optimized implementation of the HYPR-LR that can be tailored to different PET tracer behaviors and even individual studies, and rigorously evaluate the algorithm in the context of quantitative kinetic analysis of dynamic PET tracer data.

2.3 HYPR-LR Methodology

All of the formulations of HYPR make use of a temporally summed composite image in a dynamic set of images to provide a low-noise estimate of the true image at an individual time frame. This composite is weighted by a low resolution spatial comparison of each frame and the composite image. In the initial implementation of HYPR, this spatial comparison was made by means of unfiltered back-projection of acquired projection data (i.e. sinograms):

$$H_{x,t} = C_{x,t} \cdot W_{x,t} = C_{x,t} \cdot \sum_y \frac{P_{y,t}}{P_y^C} B_{x,y} \quad (2.1)$$

where $H_{x,t}$ is the HYPR estimate of an individual frame, $C_{x,t}$ is the composite image, $W_{x,t}$ is the weighting image, $P_{y,t}$ and P_y^C are the projections of an individual frame and the composite, respectively, and $B_{y,x}$ is the unfiltered back-projection operator. Note that t is a discrete time index of the reconstructed frames.

The unfiltered back-projection operation can create temporal errors in images that are not sufficiently sparse, blurring the comparison between $P_{y,t}$ and P_y^C and creating inappropriate weights (Mistretta *et al* 2006). Johnson *et al* (2008) recognized that any filtering process could serve as a valid means of comparing individual frames to the composite image, and that convolving the data in image space could minimize or eliminate temporal errors while still

providing substantial improvements in noise. They developed the LR implementation of HYPR which can be written as:

$$H_{x,t} = C_{x,t} \cdot W_{x,t} = C_x \cdot \frac{I_{x,t} \otimes F_x}{C_{x,t} \otimes F_x} \quad (2.2)$$

where F_x is the spatial filtering kernel and \otimes represents convolution. Careful selection of a filtering kernel, such that regions of differing temporal behavior do not overlap within the kernel during the convolution process, will result in completely accurate processing of the data. It is also important to note that some protection against small numbers must be implemented in the HYPR-LR algorithm as it involves a division. In this work, this is done by identifying all voxels in the blurred composite image whose values fall below 1% of the maximum of the unblurred composite image. These voxels are then assigned a value of zero in the weighting image.

Iterative HYPR methods have also been proposed to reduce temporal errors (Griswold 2007, O'Halloran *et al* 2008). However, the iterative methods suffer from increasing noise with increasing numbers of iterations, and as a post-processing tool, HYPR-LR is easily implemented on any image, and can complement other denoising techniques. HYPR-LR is thus the focus of both this work.

The formation of the composite image will be an important focus of this thesis. It can be described as:

$$C_{x,t} = \sum_{t'} I_{x,t'} \cdot \Delta_{t'} \quad (2.3)$$

where t' indexes the temporal range over which the composite image is integrated, and $\Delta_{t'}$ is the duration of frame t' . The initial implementation of HYPR-LR for dynamic PET described below

uses all time frames in the formation of the composite image ($t'=0$ to $t'=t_{\max}$, where t_{\max} is the final frame of the study). The optimized implementation of HYPR-LR uses a different range for t' for different phases of a dynamic PET study, as described in the next chapter. It is important to note that data should not be decay corrected so that each frame is weighted proportional to the measured signal in its contribution to the composite image.

2.4 Methods

2.4.1 Derenzo Resolutions Phantom

The effect of HYPR-LR processing on spatial resolution and noise was assessed using a custom made miniature Derenzo phantom. The phantom had 6 groups of fillable rods with diameters of 0.8, 1.0, 1.25, 1.5, 2.0, and 2.5 mm. The center-to-center distance for each group of rods was equal to their respective diameters. The phantom was filled with aqueous [F-18] (1.5 MBq/mL) and scanned for 60 minutes using a microPET P4 scanner (Concorde Microsystems Inc.). The acquired data were reconstructed into 60x1 minute frames using filtered back-projection (FBP) with a ramp filter (at the Nyquist frequency cutoff) to a matrix size of $128 \times 128 \times 63$ with voxel dimensions of $0.47 \times 0.47 \times 1.21$ mm. Corrections for normalization, dead time, random coincidences, attenuation, scatter, and decay of radioactivity were applied using the system software. HYPR-LR was applied with a composite image using all the frames in the study and a relatively large filtering kernel ($2.35 \times 2.35 \times 2.35$ mm³ FWHM Gaussian). The large kernel was used as it should have a greater potential impact on spatial resolution. HYPR-LR processing was compared to spatial smoothing using a Gaussian with the same dimensions as the HYPR-LR filtering kernel. Resolution was assessed using a line profile through the 2.5 and 1.5

mm rods. Noise was assessed by measuring the standard deviation of the voxels in the profile over the course of the decay corrected study.

2.4.2 Dual-Isotope Phantom

The temporal accuracy of HYPR-LR and its impact on the estimation of simple parameters were evaluated using another phantom study. In this study, a NEMA IEC body phantom with hollow spherical inserts 10, 13, 17, 22, and 28 mm in diameter was filled with two isotopes and scanned using a Discovery VCT PET/CT (GE Healthcare). The background of the phantom was filled with aqueous [F-18] (13.1 kBq/mL at the start of the emission scan) and the spherical inserts were filled with aqueous [C-11] (96.4 kBq/ml at the start of the emission scan). PET data were acquired over 150 minutes and reconstructed into 30x5 minute frames with FBP using a ramp filter (0.104 mm^{-1} cutoff frequency) to an image matrix size of 128x128x47 with voxel sizes of $3.125 \times 3.125 \times 3.27 \text{ mm}^3$. Corrections for deadtime, normalization, and scatter were applied using the system software, and attenuation correction was applied using the CT data. Decay correction was not applied. HYPR-LR was applied using composite images of varying durations and a Gaussian filtering kernels with varying widths.

Regions of interest (ROIs) were placed over [C-11] (57 voxels) and [F-18] (5471 voxels) regions in the reconstructed images. The standard deviation of the large and uniform [F-18] ROI at a single frame in the middle of the study ($t = 47.5$ minutes) was used to evaluate the impact of composite duration and kernel size on noise.

The time-activity curves (TACs) of all voxels within the phantom were also fit to a single decay exponential (Equation 2.4) using non-linear least-squares:

$$C(t)=C_0 \exp(-\lambda t) \quad (2.4)$$

where $C(t)$ is the radioactivity concentration at time t , C_0 is the initial radioactivity concentration of the voxel, and λ is the radioactive decay constant. The mean and standard deviation of the radioactive decay constant were evaluated in the [C-11] ROI before and after HYPR-LR processing to study the algorithm's impact on the estimation of simple kinetic parameters.

2.4.3 Digital Motion Phantom

A simple digital phantom was used to study the effects of motion and objects that change in size on HYPR-LR processing. Such information will be important, as motion is often an issue in PET acquisitions, and objects that change in size are seen in some PET applications, for example cardiac imaging. The phantom used consisted of a small circle within a larger circle. The contrast between the small circle and its background was 60%. The effects of motion on HYPR-LR processing were studied in two situations. In the first, the location of the small circle was simply translated relative to the rest of the image. In the HYPR-LR composite image, the shape of the small circle thus becomes a superposition of these two locations. In the second motion situation, the location of the small circle was varied sinusoidally over time, and the small circle's shape in the composite image thus becomes an average of its location over time. In order to study the effects objects of changing sizes have on HYPR-LR processing, the diameter of the smaller circle was linearly increased from 16 to 19 pixels over the course of 4 frames. The composite image is therefore an average of these sizes. In all of these studies, all frames were given equal weight in the formation of the composite image.

2.4.4 [O-15]H₂O Human Study

A human [O-15]H₂O study was processed with HYPR-LR to evaluate the algorithm's performance in an application with very noisy individual frames. The human study was acquired over 2 minutes on an Advance PET scanner (GE Healthcare Ltd.), starting at the time of injection of 2.78 GBq of tracer. Data were acquired in 2D mode, as specified by the NIH-sponsored Carotid Occlusion Surgery Study, and reconstructed using FBP (ramp filter) to a matrix size of $128 \times 128 \times 63$, with voxel dimensions of $2.34 \times 2.34 \times 4.25$ mm. HYPR-LR processing was applied to a single slice using all of the frames in the study to form the composite image and with a relatively large 21.1 mm FWHM 2-dimensional Gaussian filtering kernel.

2.5 Results

2.5.1 Derenzo Resolution Phantom

A single frame from the Derenzo resolution phantom study before and after HYPR-LR processing visually demonstrates improvement in noise with effectively no loss of spatial resolution (Figure 2.1 a & b). Spatial smoothing does significantly reduce noise, but also results in a significant loss of spatial resolution (Figure 2.1c). A profile drawn through the 2.5 and 1.5 mm diameter rods confirms that there is little to no loss of spatial resolution following HYPR-LR processing, but a significant reduction in noise, as measured by the standard deviation of the value of each voxel over the 60 frames of the study (Figure 2.1d & e). Spatial smoothing reduces the standard deviation of the voxels along the profile to a similar degree as HYPR-LR processing, but there is significant smoothing (Figure 2.1f).

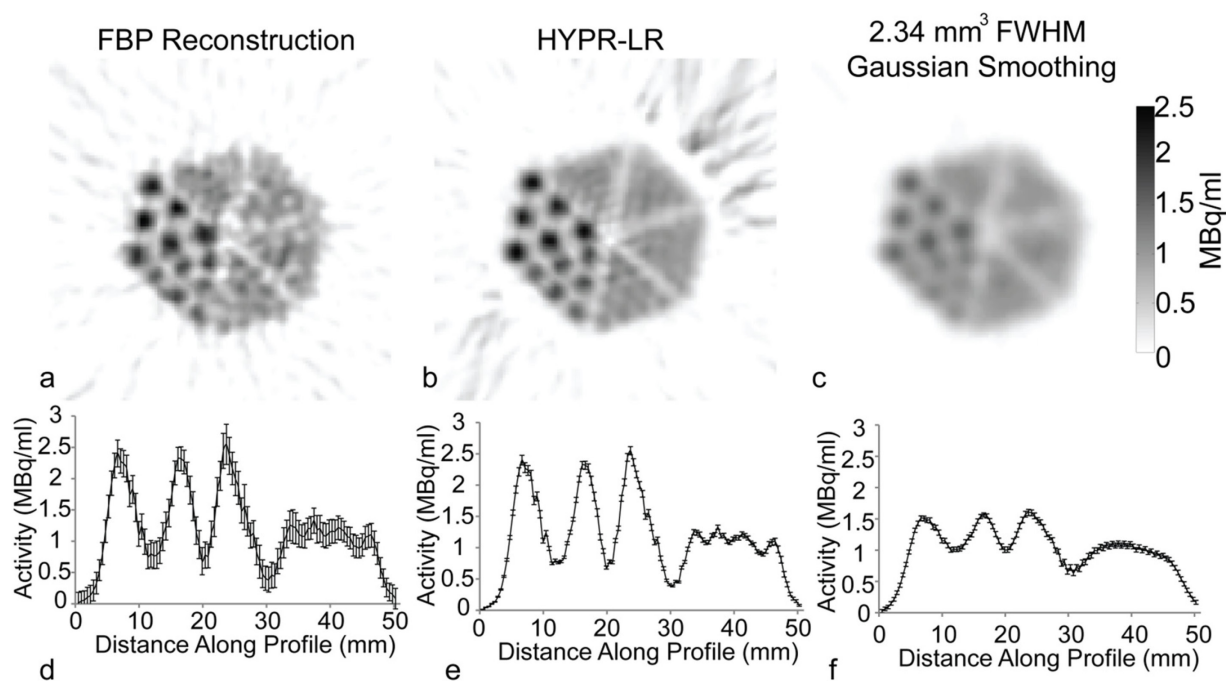


Figure 2.1. The Derenzo phantom used to study the effects of HYPR-LR on spatial resolution and image noise. Example image frames and profiles through the 2.5 and 1.5 mm diameter rods drawn on temporally summed images show that HYPR-LR processing results in little to no loss of spatial resolution. Image noise, as measured by the standard deviation of each voxel in the profile over all 60 time frames, is significantly reduced by HYPR-LR. Spatial smoothing reduces noise to a similar degree, but results in a significant loss of spatial resolution.

2.5.2 Dual-Isotope Phantom

Example images from the dual-isotope phantom study showing the calculated half-life at each voxel demonstrate how HYPR-LR can improve kinetic parameter estimates (Figure 2.2a & c). The voxel half-life estimates from the [C-11] ROI show that HYPR-LR processing improves both the accuracy and the precision of the estimated [C-11] decay constants (Figure 2.2b & d). This is a simple, but powerful illustration of the improvements in kinetic analysis that can be achieved with HYPR-LR processing.

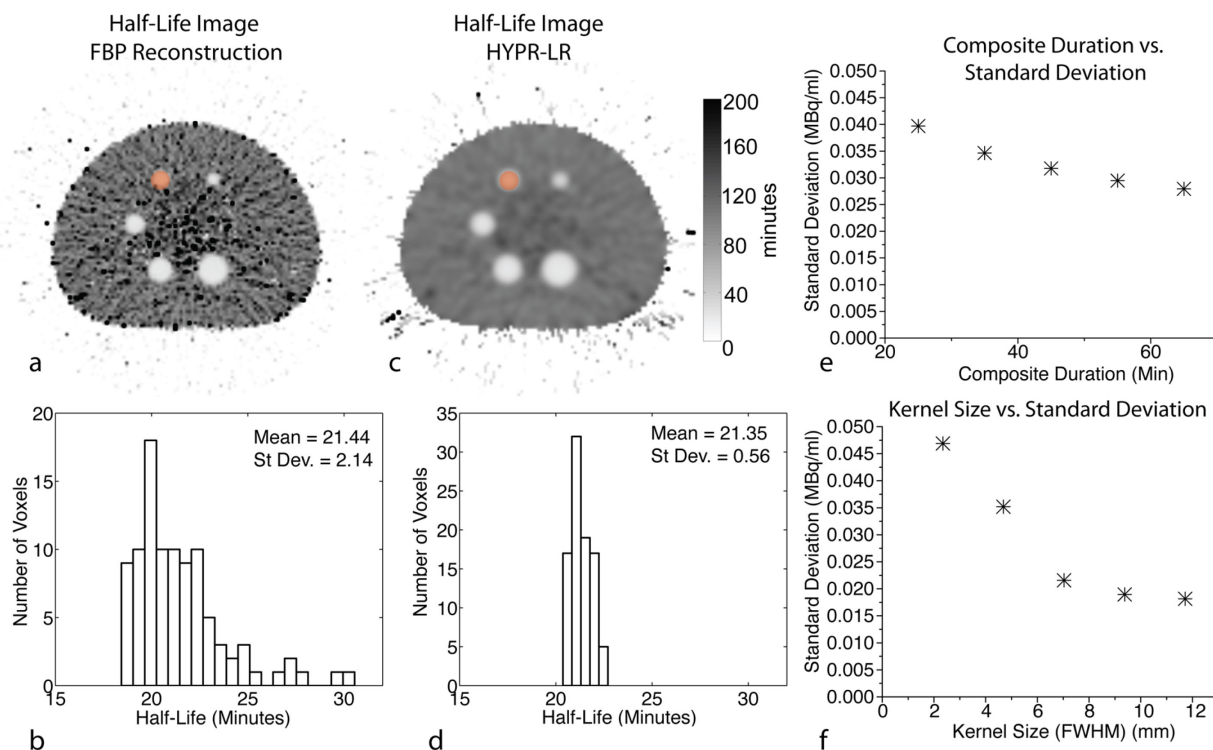


Figure 2.2. The dual-isotope phantom used to study the potential of HYPR-LR to improve the estimation of simple kinetic parameters, and to study the effects of composite duration and kernel size on noise. Half-life images show the improvements in the variance of the parameters following processing (a & c). Histograms of the voxels in the [C-11] ROI (orange circle in a & b) show this quantitatively, and demonstrate that HYPR-LR does not bias the voxels values (b & d). Noise improves as a function of the square root of the length of the composite image (e), and improvements in noise level off as larger filtering kernels are used (f).

The improvements in noise gained with HYPR-LR processing are dependent on the size of the filtering kernel used, and the duration of the composite image. Noise improves as a function of the square root of the duration of the composite image (Figure 2.2e), and improvements in noise level out as larger filtering kernels are used.

2.5.3 Digital Motion Phantom

The digital motion phantom shows that if objects move relative to the rest of the image in the course of the study, a shadow artifact will appear in HYPR-LR estimates of the individual

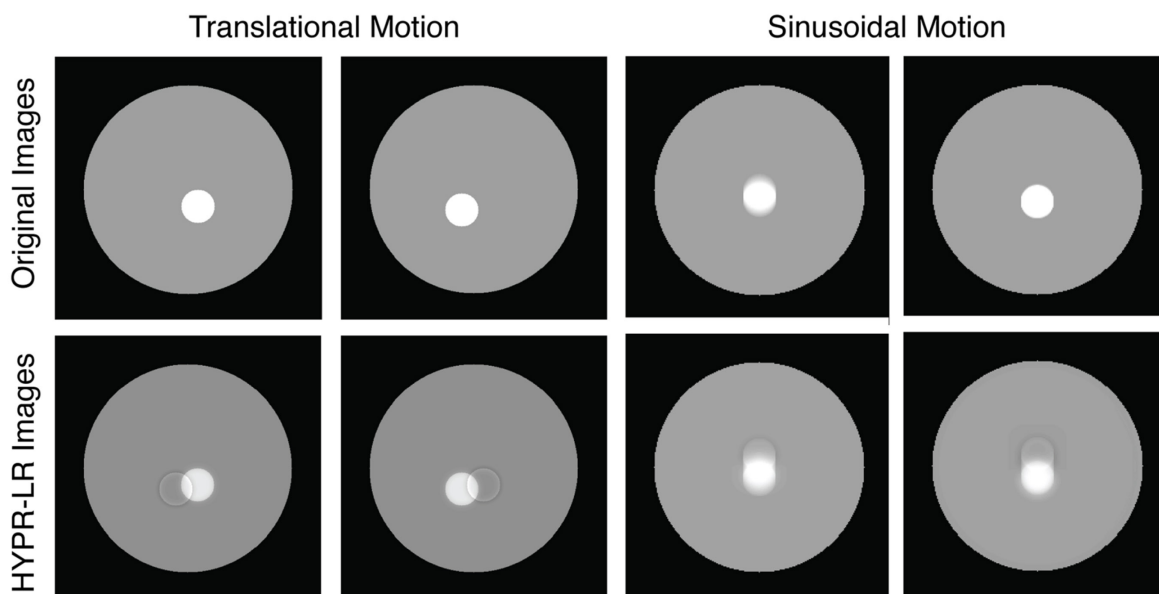


Figure 2.3. An illustration of the effects of motion on HYPR-LR processing. Objects whose position shifts in the course of a study (translational motion) create shadow artifacts in the HYPR-LR images. Objects undergoing sinusoidal motion show a similar artifact.

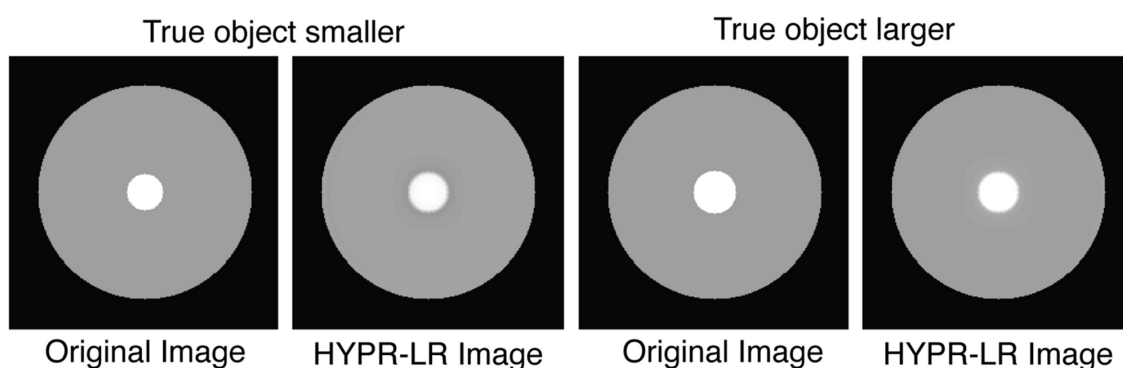


Figure 2.4. An illustration of the effects of changing object size on HYPR-LR processing. At the earliest frame, when the interior circle is smallest, the HYPR-LR image overestimates the size of the object, introduces a blur, and underestimates the values of pixels surrounding the object. Opposite effects are seen in the HYPR-LR image of the last frame, when the interior circle is at its largest.

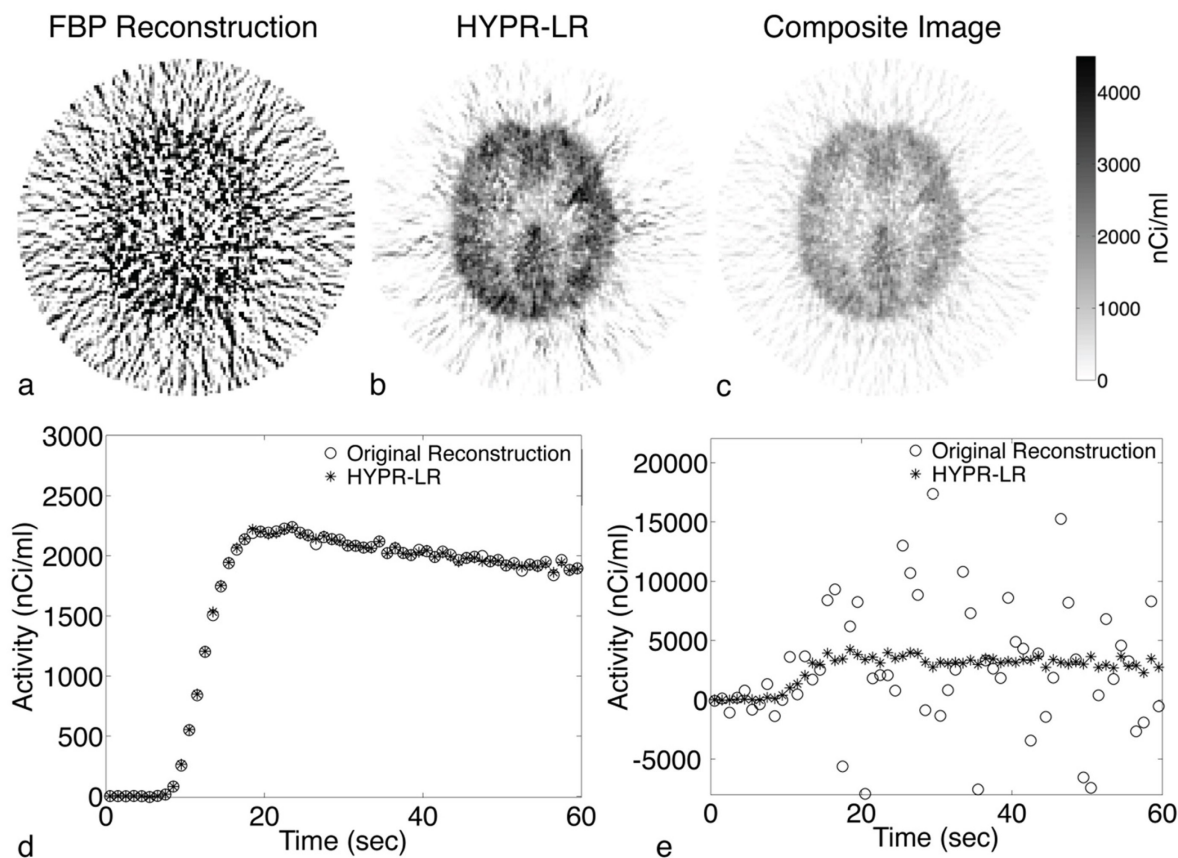


Figure 2.5. The human $[O-15]H_2O$ study used to illustrate the reductions in noise possible with HYPR-LR in dynamic PET studies with high noise. An example slice from the human $[O-15]H_2O$ study is shown from the original reconstruction (a), the data processed with HYPR-LR (b), and the composite image (c). A whole brain TAC shows that on average HYPR-LR introduces little bias (e). A single voxel TAC from the cortex shows a dramatic reduction in noise following HYPR-LR processing (f).

frames. This is true for both objects that change their location once, and objects whose location varies sinusoidally (Figure 2.3). In the case where an object changes its size over the course of a study, the size of the object in the HYPR-LR images essentially becomes an average of its size over time (Figure 2.4).

Objects whose true size is smaller or larger than the composite average are also blurred. Voxels surrounding the object in the HYPR-LR images are either underestimated in the case when the true size is smaller, or overestimated in the case where the true size is larger

2.5.4 [O-15]H₂O Human Study

A single frame from the [O-15]H₂O human study shows dramatic improvements in noise following HYPR-LR processing, and has noise properties much closer to those of the composite image (Figure 2.5a-c). A whole-brain TAC from the study shows that over a large averaged area, HYPR-LR introduces effectively no temporal bias into the data (Figure 2.5d). A single voxel TAC demonstrates the dramatic improvements in noise obtained with HYPR-LR, while the overall temporal behavior of the TAC appears to be preserved (Figure 2.5e).

2.6 Discussion

This chapter has introduced the HYPR-LR methodology for dynamic PET imaging, and explored the algorithm's effect on image quality measures, including noise, spatial resolution, temporal resolution, the effects of motion, and the estimation of simple kinetic parameters.

The Derenzo phantom shows that HYPR-LR processing has essentially no effect on spatial resolution, provided that the image object changes very little over the course of the study (Figure 2.1) As previously described, errors caused by HYPR-LR are thus due to changes in the image over time (Mistretta *et al* 2006). Errors will be influenced by spatial distributions of activity, but are not truly due to degradation of spatial resolution.

The dual-isotope phantom demonstrates the impact of composite duration and kernel size on the noise improvements seen with HYPR-LR. Noise varies as a function of the square root of the composite image, and improvements in noise level off as larger filtering kernels are used (Figure 2.2). These results are consistent with previously published descriptions of HYPR and HYPR-LR (Mistretta *et al* 2006, Johnson *et al* 2008), and verify these properties of the algorithm in the context of dynamic PET imaging.

The dual-isotope phantom also demonstrates how HYPR-LR can improve the estimation of kinetic parameters, the half-lives of two different isotopes in this case (Figure 2.2). The potential of HYPR-LR to improve the estimation of kinetic parameters from dynamic PET tracer data is explored in more detail in a later chapter.

The digital motion phantom shows that motion during a study, or changes in an objects size, will degrade the HYPR-LR estimates of individual time frames. The artifacts seen with motion and changing object size arise from the fact that all study frames were used and given equal weight in the formation of the composite image. As a result, the composite image is an inaccurate estimate of the true image, and the true image cannot be restored with the simple weighting image used in HYPR-LR.

Finally, this chapter used an $[O-15]H_2O$ study to show how HYPR-LR processing might dramatically improve PET imaging applications with very high noise. In this example, the 2 second frames essentially take on the noise properties of the 2 minute composite while little or no bias is introduced to the whole-brain or single voxel TACs studied. Studies with short frames and high noise may particularly benefit from HYPR-LR processing, provided that the image object does not change dramatically over the course of the study.

2.7 Summary and Conclusions

The results presented in this chapter are promising, and show that HYPR-LR can improve noise in individual time frames significantly and improve the precision of simple kinetic parameter estimates. The potential of HYPR-LR to improve kinetic parameter estimates from real dynamic PET tracer data will be explored in the next chapters. In addition, this chapter has not fully explored potential errors that might be caused by HYPR-LR. PET images are not

sparse, and HYPR-LR processing therefore has the potential to introduce temporal errors that might bias kinetic parameter estimates. These errors are explored in more detail in the next two chapters, and the next chapter introduces and implementation of the algorithm to limit them.

References

Christian, B T, Vandehey, N T, Floberg, J M and Mistretta, C A 2010 Dynamic PET Denoising with HYPR Processing *J. Nucl. Med.*

Griswold, M A 2007 More optimal HYPR reconstructions using a combination of HYPR and conjugate-gradient minimization *Proceedings of the 15th Annual Meeting of the ISMRM : ISMRM)*

Johnson, K M, Velikina, J, Wu, Y, Kecskemeti, S, Wieben, O and Mistretta, C A 2008 Improved waveform fidelity using local HYPR reconstruction (HYPR LR) *Magn. Reson. Med.* **59** 3 456-62

Mistretta, C A, Wieben, O, Velikina, J, Block, W, Perry, J, Wu, Y, Johnson, K and Wu, Y 2006 Highly constrained backprojection for time-resolved MRI *Magn. Reson. Med.* **55** 1 30-40

O'Halloran, R L, Wen, Z, Holmes, J H and Fain, S B 2008 Iterative projection reconstruction of time-resolved images using highly-constrained back-projection (HYPR) *Magn. Reson. Med.* **59** 1 132-9

Wu, Y, Korosec, F R, Mistretta, C A and Wieben, O 2009 CE-MRA of the lower extremities using HYPR stack-of-stars *J. Magn. Reson. Imaging* **29** 4 917-23

Chapter 3. Optimized Implementation of HYPR-LR for Dynamic PET

3.1 Introduction

The previous chapter gives examples of the significant improvements in noise that can be obtained with HYPR-LR. However, HYPR-LR still requires relatively sparse images such that regions with different temporal behaviors do not overlap within filtering kernel used to form the weighting image (Johnson *et al* 2008). Failing this HYPR-LR can distort the temporal signals of neighboring regions in the same way as the original implementation of HYPR (Mistretta *et al* 2006). This is potentially problematic for PET imaging, where regions of different temporal behavior can lie in close proximity.

3.2 Chapter Aims

The aim of this chapter is to propose an optimized implementation of HYPR-LR that limits bias while maximizing noise reduction in the context of dynamic PET imaging. This implementation uses multiple time-dependent composite images that are formed based on the kinetics of the tracer being studied. These composites use the maximum amount of temporal data (i.e. long integration times) that is possible without introducing any bias. If composite images are shorter than this, they will provide no benefit in terms of reduced bias, and less noise reduction will be achieved; if they are made larger additional noise improvements will come at the cost of bias. Such an approach is less arbitrary than the traditional method for minimizing bias of using a sliding composite window of some fixed duration (Mistretta *et al* 2006). This implementation is introduced in this chapter and explored in more detail in the context of quantitative kinetic analysis in the next chapter.

3.3 Theory and Methodology

The only way for the HYPR-LR estimate of a PET frame to be perfectly accurate is if the contrast between objects present in the frame is the same as the contrast between those objects in the frame's composite image. Failing this, errors at boundary regions will depend on the difference in contrast between neighboring regions and the size of the kernel used (Figure 3.1).

Quantitatively accurate application of HYPR-LR to PET data may still be possible because of the predictable behavior of PET tracers. This predictable behavior can be used to form composite images that more closely fulfill the criteria of having the same contrast between objects as their corresponding frames, and the proposed optimized implementation of HYPR-LR for PET data attempts to achieve this.

A typical PET tracer's behavior can be divided into three phases: uptake, specific retention, and equilibrium. Immediately after a tracer's injection, during the brief uptake phase, the activity in all regions will be increasing at a relatively constant rate. During the specific retention phase, regions distinguish themselves from each other in a predictable manner. Finally, the tracer will reach a state of equilibrium, at a time frequently referred to as t^* , the attainment of which is

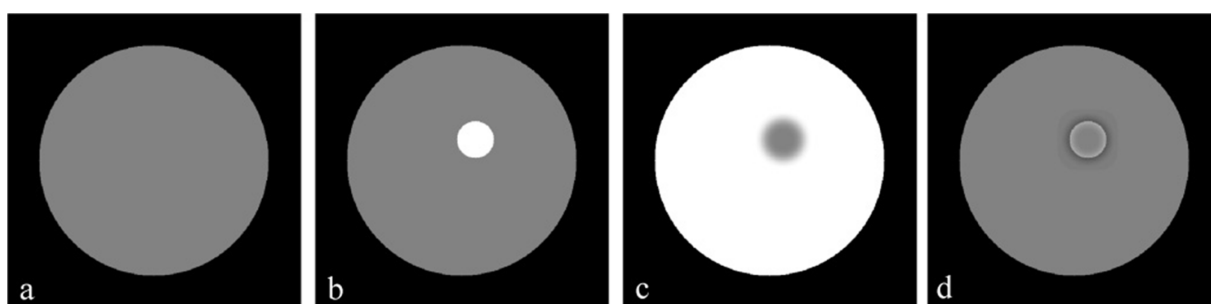


Figure 3.1. Illustration of the errors HYPR-LR can cause. The original image in this case is uniform (a), but a region of high uptake is revealed in the composite image (b). As a result, the weighting image (c) is inappropriately blurred, creating errors in the HYPR-LR result (d).

required for application of graphical analysis methods and after which the image changes very little (Patlak *et al* 1983, Patlak and Blasberg 1985, Logan *et al* 1990, Logan *et al* 1996). Figure 3.2 illustrates these behaviors for [C-11]PIB, a tracer of interest, for different regions of the brain. Composite images can thus be formed for the uptake and equilibrium phases by summing all the frames in these phases. A sliding composite can be used during the retention phase such that the change in contrast is nearly linear for the frames used, creating a composite very similar to the individual frame being processed. This approach is similar to recently proposed scatter correction methods that take into account the different counting rates seen in the different phases of a dynamic PET study (Cheng *et al* 2007).

The formation of these multiple composite images can be expressed as:

$$\text{For } t = 1 \text{ to } t_{\text{uptake}} \quad C_{x,t} = \sum_{t'=1}^{t_{\text{uptake}}} I_{x,t'} \cdot \Delta_{t'} \quad (\text{a})$$

$$\text{For } t = t_{\text{uptake}}+1 \text{ to } t^*-1 \quad C_{x,t} = \sum_{t'=t-\alpha}^{t+\alpha} I_{x,t'} \cdot \Delta_{t'} \quad (\text{b}) \quad (3.1)$$

$$\text{For } t = t^* \text{ to } t_{\text{max}} \quad C_{x,t} = \sum_{t'=t^*}^{t_{\text{max}}} I_{x,t'} \cdot \Delta_{t'} \quad (\text{c})$$

The phases of the study are demarcated here by t_{uptake} , the frame at which the uptake phase ends, t^* , the frame at which the steady state begins, and t_{max} , the final frame of the study. The parameter α determines the number of frames to be used in the sliding composite during the specific retention phase.

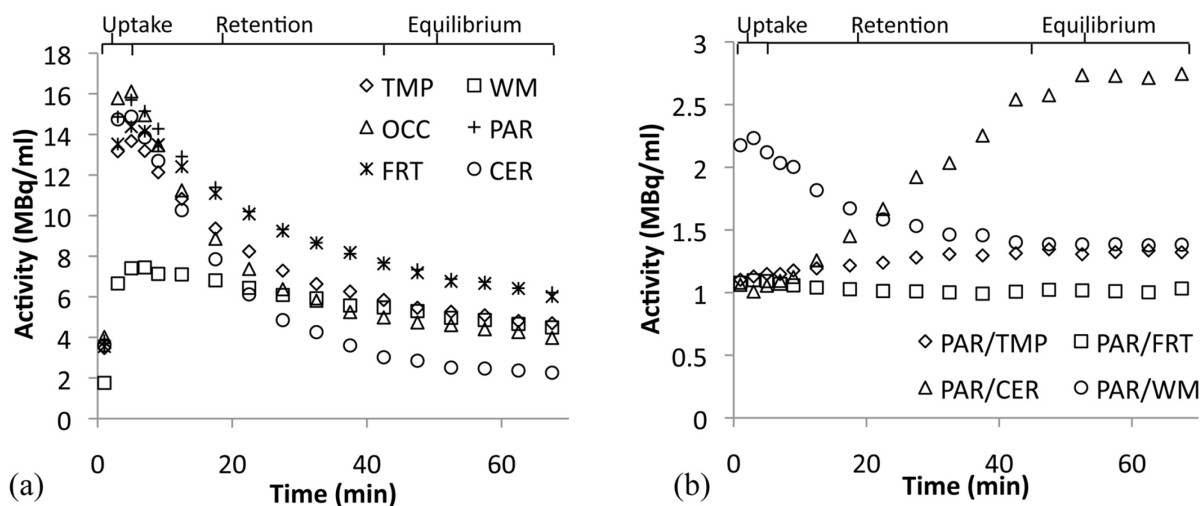


Figure 3.2. [C-11]PIB time activity curves (TACs) for regions of the brain from a [C-11]PIB positive human study (a), and the ratio of the activities of neighboring regions at each time point (b). The phases of the tracer's temporal behavior can be used to form more appropriate temporally dependent composite images for HYPR-LR. (PAR = parietal cortex, FRT = frontal cortex, TMP = temporal cortex, OCC = occipital cortex, WM = white matter, CER = cerebellum).

The temporal parameters in Equation 3.1 must be determined from the data to be analyzed. This can be done on a region of interest (ROI) level. Specifically, ROIs should be drawn over structures in the image, and the ratios of neighboring structures must be examined. More emphasis can be put on structures of relevance. This is illustrated in Figure 3.2b with the parietal cortex and the surrounding structures in a human [C-11]PIB dataset. The parameters t_{uptake} and t^* can be determined by identifying the end of the flat uptake phase and the start of the flat equilibrium phase, respectively. α is more arbitrary. The frames at the beginning and end of the retention phase will largely determine the size of α , and α should be made as large as possible while keeping the contrast in the composite images for these frames as close as possible to the contrast in the frames themselves. Selection of the parameters used in Equation 3.1 could be

done for individual patients, or for a general population for whom a tracer's temporal behavior is relatively consistent.

The size of the kernel, F , used in the formation of the weighting image is the other parameter which must be determined. The size of the kernel will determine the degree to which regions with disparate temporal behaviors overlap and contribute to bias, and also determine the spatial frequencies of individual frames that effectively take on the noise properties of their composite images (Johnson *et al* 2008). If the proposed composite scheme is implemented correctly and the contrast between objects in individual frames and their respective composites is nearly the same, overlap between regions should contribute little to temporal errors. A larger kernel should thus be desirable, as it will suppress noise at a wide range of spatial frequencies. In this work, the largest kernel used was a 3-dimensional (3-D) Gaussian with a FWHM approximately double the resolution of the scanner, 9 mm in this case. If the composite images do not match their respective frames, a relatively small kernel should be used to limit bias. The smallest kernel use in this work was a 3-D Gaussian with a FWHM of 3mm, close to the thickness of the cortex, the primary object of interest for [C-11]PIB. The effects of kernel size are further explored in the next chapter.

The proposed method of forming multiple composite images will itself be limited in a number of respects. For one, it will likely not be possible to create composite images that have the exact same contrast between objects as in their respective frames. However, so long as there is not substantial bias introduced into multiple frames, having a few frames slightly biased by imperfect composite images should not affect kinetic analysis a great deal. Secondly, some PET tracers may not be amenable to the method of forming composites described in Equation 3.1. Finally, using shorter composite images will increase the variance in individual frames and in

quantitative parameter estimates. Nevertheless, the ratio of the activities of neighboring regions should at least be examined to provide insight into what time-series data should be used to form composite images. This will allow for the maximum benefit in terms of variance reduction while minimizing bias for a given PET tracer and imaging task.

3.4 Summary

In this chapter, a more optimal implementation of HYPR-LR has been introduced that can be tailored to specific studies. This implementation attempts to limit potential bias caused by the algorithm while providing the maximum possible reduction in noise by forming multiple time-dependent composites that account for a tracer's kinetic behavior. Such an implementation may be especially beneficial in the quantitative kinetic analysis of dynamic PET tracer data. This is explored in the next chapter.

References

- Cheng, J C, Rahmim, A, Blinder, S, Camborde, M L, Raywood, K and Sossi, V 2007 A scatter-corrected list-mode reconstruction and a practical scatter/random approximation technique for dynamic PET imaging *Phys. Med. Biol.* **52** 8 2089-106
- Johnson, K M, Velikina, J, Wu, Y, Kecskemeti, S, Wieben, O and Mistretta, C A 2008 Improved waveform fidelity using local HYPR reconstruction (HYPR LR) *Magn. Reson. Med.* **59** 3 456-62
- Logan, J, Fowler, J S, Volkow, N D, Wang, G J, Ding, Y S and Alexoff, D L 1996 Distribution volume ratios without blood sampling from graphical analysis of PET data *J. Cereb. Blood Flow Metab.* **16** 5 834-40
- Logan, J, Fowler, J S, Volkow, N D, Wolf, A P, Dewey, S L, Schlyer, D J, MacGregor, R R, Hitzemann, R, Bendriem, B and Gatley, S J 1990 Graphical analysis of reversible radioligand binding from time-activity measurements applied to [N-¹¹C-methyl]-(-)-cocaine PET studies in human subjects *J. Cereb. Blood Flow Metab.* **10** 5 740-7
- Mistretta, C A, Wieben, O, Velikina, J, Block, W, Perry, J, Wu, Y, Johnson, K and Wu, Y 2006 Highly constrained backprojection for time-resolved MRI *Magn. Reson. Med.* **55** 1 30-40

Patlak, C S and Blasberg, R G 1985 Graphical evaluation of blood-to-brain transfer constants from multiple-time uptake data. Generalizations *J. Cereb. Blood Flow Metab.* **5** 4 584-90

Patlak, C S, Blasberg, R G and Fenstermacher, J D 1983 Graphical evaluation of blood-to-brain transfer constants from multiple-time uptake data *J. Cereb. Blood Flow Metab.* **3** 1 1-7

Chapter 4. Improved Kinetic Analysis with Dynamic PET Data with HYPR-LR

4.1 Introduction

The reductions in noise gained from HYPR-LR processing could improve the precision and accuracy of kinetic parameters estimated from dynamic PET tracer data. The proposed optimal implementation of the algorithm could provide these improvements while introducing minimal bias. More precise and accurate kinetic parameter estimates could improve the utility of dynamic PET data in a number of contexts. Parametric image generation (i.e. voxel-by-voxel kinetic analysis) could be a particularly valuable application for HYPR-LR as parametric images provide physiologic information on the finest possible spatial scale but are limited by high noise. Less variance in parametric images could enable the identification of trends that would otherwise be lost to noise and lend greater confidence to existing trends and observations. HYPR-LR could likewise benefit kinetic analysis on a region of interest (ROI) level, but the benefits will diminish as larger ROIs are used. The effect of HYPR-LR processing on parametric images is thus the primary focus of this chapter.

4.2 Chapter Aims

The aim of this chapter is to rigorously evaluate the tradeoff between bias and variance seen with HYPR-LR processing in both individual time frames and parametric images of PET tracer data. This is done for [C-11]Pittsburgh Compound B ([C-11]PIB), a tracer that binds to beta-amyloid that is amenable to a number of kinetic analysis methods (Yaqub *et al* 2008). This allows the effects of HYPR-LR on different analysis methods to be evaluated using the same data. Two analysis methods are studied here: the reference region Logan graphical method and

the basis function implementation of the simplified reference tissue method (SRTM), so called receptor parametric mapping (RPM or RPM2) (Logan *et al* 1990, Logan *et al* 1996, Lammertsma and Hume 1996, Gunn *et al* 1997, Wu and Carson 2002). The Logan graphical method is used as it is simple to implement and assumes no particular model, but is limited by a noise-dependent bias (Slifstein and Laruelle 2000, Logan 2000). RPM2 is generally considered to be more robust than the Logan method with regards to both bias and variance (Yaqub *et al* 2008), but it assumes a model and requires a nonlinear fit, which is more difficult to implement and more sensitive to parameters used in the fitting process. Both the proposed implementation of HYPR-LR using multiple composite images, heretofore called HYPR-LR-MC (multiple composites), and an implementation using all the frames in a dataset to form the composite, heretofore called HYPR-LR-FC (full composite), are studied. Simulated dynamic studies are used to evaluate the absolute performance of the HYPR-LR, and human studies are used to study the algorithm in the context of a true imaging task. While the focus here is on two analysis methods for [C-11]PIB data, this work is also intended to provide a framework for determining the optimal implementation of HYPR-LR for a given imaging task that can be generalized to other tracers and analysis methods.

4.3 Methods

4.3.1 Creation of Numerical Phantoms

As HYPR-LR processing uses data in both space and time, realistic spatial distributions of time activity curves (TACs) and noise must be simulated. With this in mind, numerical phantoms were created using TACs obtained from a human [C-11]PIB acquisition and the Zubal brain phantom (Zubal *et al* 1994). The [C-11]PIB TACs used were taken from a [C-11]PIB positive human scan acquired over 70 minutes with 5x2 minute and 12x5 minute frames. ROIs were

drawn over the frontal cortex, parietal cortex, occipital cortex, temporal cortex, white matter, and cerebellum on a temporally summed image. The resulting temporal patterns were used to create a noise-free dynamic image set by impressing the TAC values into their corresponding regions in the Zubal phantom image.

A PET acquisition on an ECAT HR+ scanner was then approximated using published performance information of the scanner model (Brix *et al* 1997, Herzog *et al* 2004). Data were first resampled to voxel sizes of 2.2x2.2x2.45mm, and then smoothed with a 4.39x4.39x5.10 mm³ full-width-at-half-maximum (FWHM) Gaussian to approximate the resolution of the scanner. The activity distributions in the smoothed images were converted into expected counts by multiplying by factors for decay correction, frame duration, and voxel volume. Data in each slice were then forward projected at 160 angles spaced at 1.125 degrees using MATLAB's (The MathWorks®) 2-dimensional radon transform function (i.e. a 2 dimensional acquisition). An attenuation map for each slice was created by assigning all voxels identified as bone in the Zubal brain phantom an attenuation coefficient of bone, and all voxels identified as other tissues an attenuation coefficient of water at 511 keV. The attenuation map was then resampled to the same matrix size as the PET images and forward projected at the same angles as the emission data. Each simulated emission sinogram was multiplied by its corresponding attenuation sinogram and the published sensitivity of the scanner. Scatter was not modeled, but sinograms were multiplied by the expected scatter fraction for the amount of activity used in the simulation. While this does not accurately model scatter, it will reduce counts to a similar degree as a true scatter correction algorithm so that added count-dependent Poisson noise is appropriately scaled. A noisy data value was then generated at each position in the resulting sinograms by generating a random number from a Poisson distribution with a mean equal the value of that position in the noise-free

sinograms. The resulting noisy sinograms were reconstructed with filtered backprojection (FBP) using a ramp filter with a cutoff at 0.75 the Nyquist frequency after correcting for attenuation, and values in the resulting images were converted back to activity units (Bq/ml). Fifty noisy realizations of the same simulated [C-11]PIB dataset were produced in this way. The noise-free sinograms were also reconstructed with FBP to use as a standard. FBP reconstruction was used as it is an analytical method that does not introduce any bias of its own, unlike iterative reconstructions like expectation-maximization (EM) and *maximum a posteriori* (MAP). This will allow for a more thorough evaluation of the bias and variance properties of HYPR-LR that is not confounded by the tradeoff between bias and variance in the reconstruction itself.

4.3.2 Acquisition of Real Data

Eight human [C-11]PIB datasets were evaluated to illustrate the potential of HYPR-LR to improve the kinetic analysis of real data. These datasets were selected as a representation of [C-11]PIB positive scans. All data were obtained in accordance with a human subjects research protocol approved by the University of Wisconsin institutional review board. Briefly, the PET data were acquired using a Siemens HR+ scanner in 3-D mode (septa retracted). A five minute transmission scan was first acquired for attenuation correction, followed by a 70 minute dynamic emission scan initiated with a 30 second bolus infusion of radiotracer (518-585 MBq). The data were divided into 5x2 minute frames and 12x5 minute frames and reconstructed using a filtered backprojection algorithm using a ramp filter (at the Nyquist frequency) to a voxel size of $2.0 \times 2.0 \times 4.25 \text{ mm}^3$ and corrected for random events, attenuation, dead-time, scanner normalization, and scatter radiation.

4.3.3 HYPR-LR Processing and Smoothing

Both the real data and the simulated data were processed with HYPR-LR-FC and HYPR-LR-MC. A summary of the HYPR-LR terminology frequently used in this chapter is included in Table 4.1. The relevant temporal parameters for HYPR-LR-MC (Chapter 3, Equation 3.1) were determined by examining the ratios of the activities of neighboring regions, as described in Chapter 3. The same parameters were determined to be appropriate for both the simulated data and all the human datasets, Namely, t_{uptake} was set at frame 3 (6 minutes), α was set to 2 frames (5 frames total in the sliding window), and t^* was set at frame 12 (40 minutes). The impact of kernel size was studied using 3-dimensional Gaussian filtering kernels with a FWHM in each spatial dimension of three different sizes: 3, 6, and 9 mm. The 9x9x9 mm³ FWHM kernel was used to process all of the human data to examine both the maximum improvement in variance and the maximum bias to be expected from HYPR-LR processing.

Table 4.1. A summary of HYPR-LR terminology used frequently in this chapter

Term	Definition
HYPR-LR	Highly constrained backProjection-Local Reconstruction
Composite Image	Temporally summed (i.e. time-averaged) image used in HYPR-LR processing to provide a low-noise estimate of a frame
Weighting Image	Spatial comparison of an individual frame with its composite image used to weight the composite image
F , Filtering Kernel	The smoothing kernel used to make the spatial comparison between an individual frame and its composite image
HYPR-LR-MC	HYPR-LR with Multiple Composite images
HYPR-LR-FC	HYPR-LR with a Full Composite image (summed over all frames)

Simulated and real data were also smoothed (after reconstruction) to provide a simple denoising method to compare HYPR-LR processing to. Data were smoothed with 3x3x3 and 6x6x6 mm³ FWHM Gaussian kernels. Although smoothing is not as sophisticated as other denoising techniques, it is still one of the most commonly used methods for reducing noise.

4.3.4 Kinetic Analysis

Parametric images of the non-displaceable binding potential (BP_{ND}) were created from both the simulated and human data. The BP_{ND} is the ratio of bound to unbound (non-displaceable) tracer at equilibrium. This is one of the primary quantitative measures used for tracers that show reversible binding behavior, and is frequently taken as a measure of available receptors. BP_{ND} parametric images were created using the reference region Logan graphical method and receptor parametric mapping (RPM2). These analysis methods are described in detail in Appendix A.

The cerebellum was used as a reference region for both analysis methods (Lammertsma and Hume 1996, Price *et al* 2005)(Logan *et al* 1996). For all [C-11]PIB data, Logan graphical analysis was performed using a reference tissue efflux constant, k_{2REF} , of 0.144min⁻¹(Price *et al* 2005, Lopresti *et al* 2005), and an equilibrium time, t^* , of 40 minutes, determined from the data analyzed. The Logan distribution volume ratios (DVRs) generated at each voxel were converted to non-displaceable binding potentials ($BP_{ND} = DVR - 1$). RPM2 was performed using a k_{2a}^{min} of 0.02min⁻¹ and a k_{2a}^{max} of 0.1 min⁻¹ with 50 basis functions. The minimum and maximum values for k_{2a} were derived from non-linear least squares SRTM fits to several ROI TACs from both real and simulated data. The minimum k_{2a} value used falls slightly above the values obtained from some of these fits, but gives results that are most consistent when compared with the Logan results. The reference region efflux constant, k_2^{REF} , used in RPM2 was determined by finding the median k_2^{REF} of all voxels with a $BP_{ND} > 0$ in the first-pass fitting.

RPM2 requires that each frame be weighted by its duration and the total number of counts in the frame (without decay correction) (Gunn *et al* 1997):

$$\text{Frame Weight} = \frac{(\text{Frame duration})^2}{\text{Total counts in frame}} \quad (4.1)$$

The unprocessed data were weighted in this fashion, but a different weighting scheme is required for the HYPR-LR processed data, as the variance in each frame will no longer be determined by the number of counts in the frame, but by the number of counts in the composite image. The frames in the HYPR-LR processed data were therefore weighted as (again, without decay correction):

$$\text{HYPR - LR Frame Weight} = \frac{(\text{Composite duration})^2}{\text{Total counts in composite}} \quad (4.2)$$

Fits to the HYPR-LR-FC data will thus be uniformly weighted as the same composite is used for each frame.

For the simulated data, the parametric Logan image generated from the noise-free FBP reconstruction was used as a standard to which all noisy simulated parametric images were compared. The reference region Logan method assumes no model, and therefore should be the least biased of any reference tissue method when there is no noise in the data.

4.3.5 Data Evaluation

4.3.5.1 Bias and Variance in the Simulated Data

The impact of HYPR-LR processing on both individual time frames and parametric images was evaluated by measuring the bias and variance of the simulated data. The bias at each voxel in each time frame was taken as the percentage difference between the mean voxel value over the

50 noise realizations and the voxel value in the noise-free FBP reconstruction:

$$\text{bias (\%)} = \frac{\mu_x - x}{x} \cdot 100 \quad (4.3)$$

where μ_x is the mean voxel value over all noise realizations and x is the true voxel value. Bias in the parametric images was measured in the same way, using the voxel values in the reference Logan parametric image created from the noise-free FBP reconstruction as a reference.

The variance was evaluated using the coefficient of variation (COV) at each voxel:

$$\text{COV} = \frac{\sigma_x}{\mu_x} \quad (4.4)$$

where σ_x is the standard deviation of a voxel over all noise realizations. The mean bias and COV of all voxels in the parietal and frontal cortices is reported (11794 voxels). The bias and COV of the time-series data were averaged over all frames.

4.3.5.2 Evaluation of the Human Data

A ROI based kinetic analysis was used to evaluate bias in the parametric images of the human data. For each dataset, ROIs were drawn over the frontal and parietal cortex (regions of particular interest in [C-11]PIB scans) on temporally summed images. ROIs contained 2648 voxels on average (range 1150-4385 voxels). TACs averaged over these ROIs were analyzed with the reference Logan graphical method with the same parameters described above to generate an average BP_{ND} value for the entire corresponding region. Over such a large region, the Logan estimates of the BP_{ND} should be relatively unbiased as there is little noise in the TAC and a model is not assumed. These BP_{ND} values were thus used as a standard and compared with the BP_{ND} values from the same regions in the parametric images. In the ideal case, the BP_{ND} values taken from the parametric images will match the ROI Logan estimates exactly. A bias will

appear as a deviation from unity in the slope of a linear fit to the data, or a deviation from zero in the y-intercept.

BP_{ND} values obtained with the reference Logan method and RPM2 were also compared voxel-by-voxel before and after processing to give an indication of variance in the parametric images. For each human [C-11]PIB dataset, the voxel values obtained with each method were plotted against each other and fit to a straight line. The Pearson correlation coefficient (r) of the resulting fits should provide an indication of the variance in the parametric images. This assumes that the effect of noise in the time-series data on the BP_{ND} estimates is independent for Logan analysis and RPM2. This is likely not true, and this approach therefore only gives a semi-quantitative estimate of the variance in the parametric images. The correlation coefficients obtained from each dataset were compared between the original data, smoothing with a $3 \times 3 \times 3$ mm³ FWHM Gaussian, HYPR-LR-MC, and HYPR-LR-FC using paired t-tests.

4.4 Results

4.4.1 Evaluation Bias and Variance in the Simulated Data

The noise-free simulated data give insight into the bias that HYPR-LR processing can introduce. In the case of the simulated [C-11]PIB data studied here, HYPR-LR-FC introduces errors into border regions of individual time frames that distort TACs (Figure 4.1). As a result, there are also errors in the BP_{ND} parametric images created with both the Logan graphical method and RPM2 (Figure 4.2). HYPR-LR-MC effectively eliminates these errors.

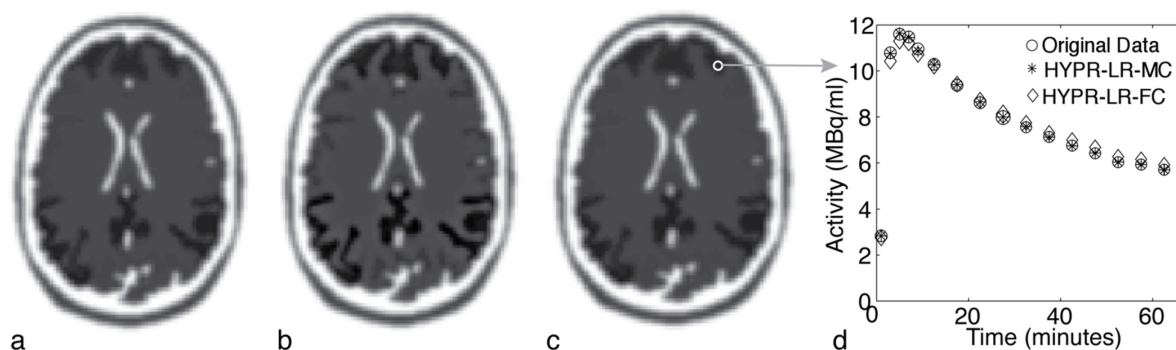


Figure 4.1. Evaluation of HYPR-LR with a noise-free simulated phantom. A frame from the original reconstruction (a) is compared to HYPR-LR-FC (b) and HYPR-LR-MC (c). In this frame, HYPR-LR-FC inappropriately increases the contrast between the cortex and the white matter. The errors in individual frames change the shape of TACs (d). HYPR-LR-MC virtually eliminates errors caused by HYPR.

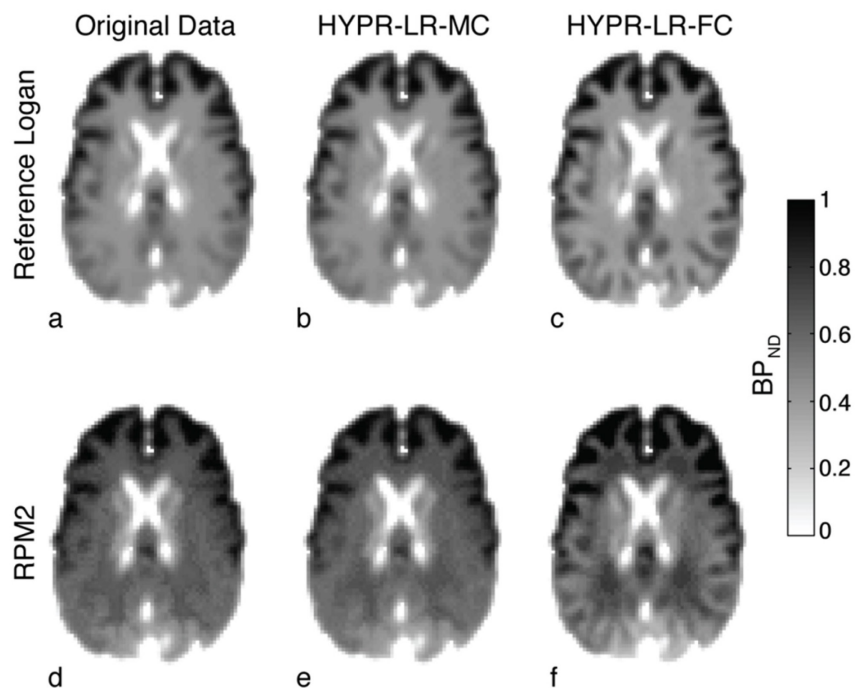


Figure 4.2. Parametric images of the noise-free simulated data generated with either the reference region Logan graphical method (a-c) or RPM2 (d-f). RPM2 tends to overestimate BP_{ND} values in some regions, particularly the white matter. The parametric images generated from the data processed with HYPR-LR-MC (b&e) differ little from the parametric images generated from the unprocessed data (a&d). The parametric images generated from the data processed using HYPR-LR-FC (c&f) show greater contrast between the high uptake regions of cortex and the surrounding white matter.

The noisy simulated data demonstrate the tradeoff between this bias and the variance reduction seen with HYPR-LR processing. In individual time frames, data processed with HYPR-LR-MC and HYPR-LR-FC show significant reductions in the COV (Figure 4.3a). HYPR-LR-MC processing does not reduce the average COV as much as HYPR-LR-FC, but it effectively introduces no bias. Averaged over all frames, the bias introduced by HYPR-LR-FC is small, 0.47% when the $9 \times 9 \times 9 \text{ mm}^3$ filtering kernel is used. Larger filtering kernels provide more variance reduction. No additional bias is seen with HYPR-LR-MC as kernel size increases, and bias increases with kernel size for HYPR-LR-FC. Both implementations of HYPR-LR compare very favorably with spatial smoothing, which introduces significant negative bias into individual time frames due to loss of spatial resolution.

HYPR-LR processing significantly improves both the bias and variance in the parametric images created with the Logan graphical method (Figure 4.3b). As with the individual time frames, HYPR-LR-FC reduces noise to a greater degree than HYPR-LR-MC, but can also introduce a slight bias. Greater reductions in both the noise-dependent Logan bias and the COV are achieved with larger filtering kernels. For example, HYPR-LR-MC with a $9 \times 9 \times 9 \text{ mm}^3$ FWHM Gaussian kernel reduces the mean bias from -37.1% to -0.21% and the average COV from 33.1% to 11.0%. HYPR-LR-FC with the same kernel further reduces the COV to 6.37% and introduces a slight positive bias of 2.45%. This positive bias is consistent with what is observed in Figure 4.2. Parametric Logan images created from the HYPR-LR processed data compare very favorably to the images created from the smoothed data. Smoothing with a $3 \times 3 \times 3 \text{ mm}^3$ FWHM Gaussian reduces the average bias to -22.7% and the average COV to 29.5%, and the $6 \times 6 \times 6 \text{ mm}^3$ FWHM

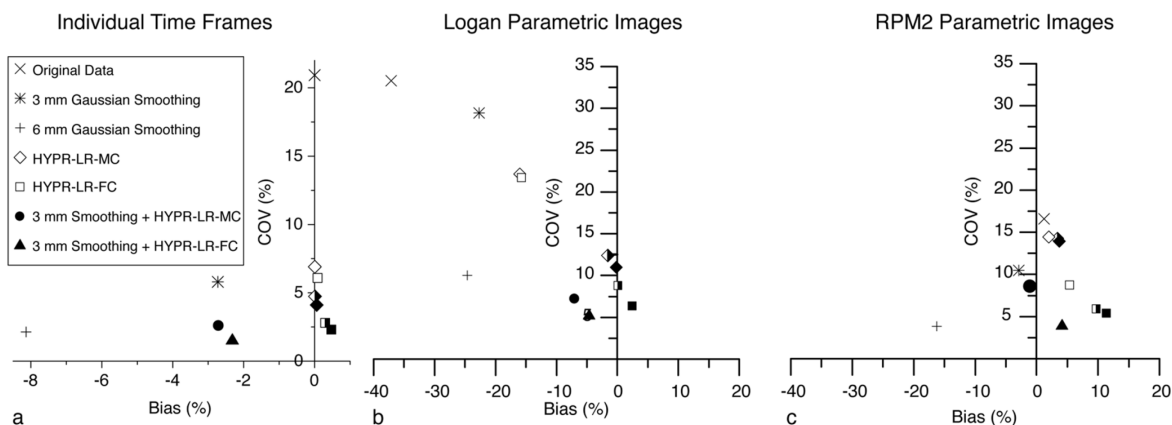


Figure 4.3. The relationship between bias and the COV in the simulated data for individual time frames (a), Logan parametric images (b), and RPM2 parametric images (c). The mean bias and COV of voxels in the frontal and parietal cortices are shown for the original data, the data spatially smoothed with 3 and 6 mm FWHM 3-D Gaussians, and for the data processed with HYPR-LR-MC and HYPR-LR-FC using Gaussian smoothing kernels with either a 3 mm (open shapes), a 6 mm (half-open shapes), or a 9 mm FWHM (solid shapes). The mean bias and COV following both spatial smoothing with a 3 mm FWHM Gaussian and HYPR-LR-MC and HYPR-LR-FC with a 9 mm FWHM Gaussian kernel are also shown.

Gaussian reduces the average bias to -24.6% (though this bias is largely due to smoothing not noise), and the average COV to 10.0%.

HYPR-LR-MC and HYPR-LR-FC processing also reduce the variance in the RPM2 parametric images. The variance reduction provided by HYPR-LR-MC processing is not as great as in the Logan images, but it does provide an improvement while introducing little bias. Variance reduction increases as larger kernels are used with HYPR-LR-MC and little additional bias is introduced (Figure 4.3c). For example, when the largest filtering kernel is used HYPR-LR-MC processing reduces the COV from 16.6% to 14%, and increases the bias from 1.2% to 3.73%. HYPR-LR-FC processing reduces noise more dramatically than HYPR-LR-MC, but at the cost of introduced bias. The tradeoff between bias and noise is closely related to kernel size for HYPR-LR-FC. When a $3 \times 3 \times 3 \text{ mm}^3$ kernel is used, the average COV is reduced to 8.7% and

average bias increases to 5.39%. When a $9 \times 9 \times 9 \text{ mm}^3$ FWHM kernel is used, average COV drops to 5.37% and average bias increases to 11.4%. Spatial smoothing does compare relatively favorably to HYPR-LR in the RPM2 parametric images. Smoothing with the $3 \times 3 \times 3 \text{ mm}^3$ FWHM Gaussian reduces the average COV to 10.5% and creates a negative bias of -2.92% relative to the baseline bias for RPM2 of 1.2%.

HYPR-LR can also be used in addition to spatial smoothing. Although resolution will still be degraded by the initial smoothing, HYPR-LR will provide an additional reduction in noise with no further loss of spatial resolution. For example, smoothing with a $3 \times 3 \times 3 \text{ mm}^3$ FWHM Gaussian followed by HYPR-LR-MC processing with a $9 \times 9 \times 9 \text{ mm}^3$ FWHM Gaussian kernel reduces the average COV in the Logan parametric images to 7.19%, albeit while increasing bias to -6.98%, and reduces the variance in the RPM2 parametric images to 8.55% with a bias of -1.03%.

4.4.2 Evaluation of Human [C-11]PIB Data

Illustrative parametric images from a human PIB dataset qualitatively demonstrate the relative tradeoff between variance and (in the case of the Logan method) bias reduction, and introduced bias from HYPR-LR processing or simple spatial smoothing (Figure 4.4). These images are consistent with the data presented in the simulation results. HYPR-LR-MC reduces the variance in both the Logan and RPM2 parametric images, though the variance reduction is notably greater for the Logan images. HYPR-LR-MC also globally increases the BP_{ND} values in the Logan images, indicating a reduction of the noise-dependent bias. HYPR-LR-FC provides

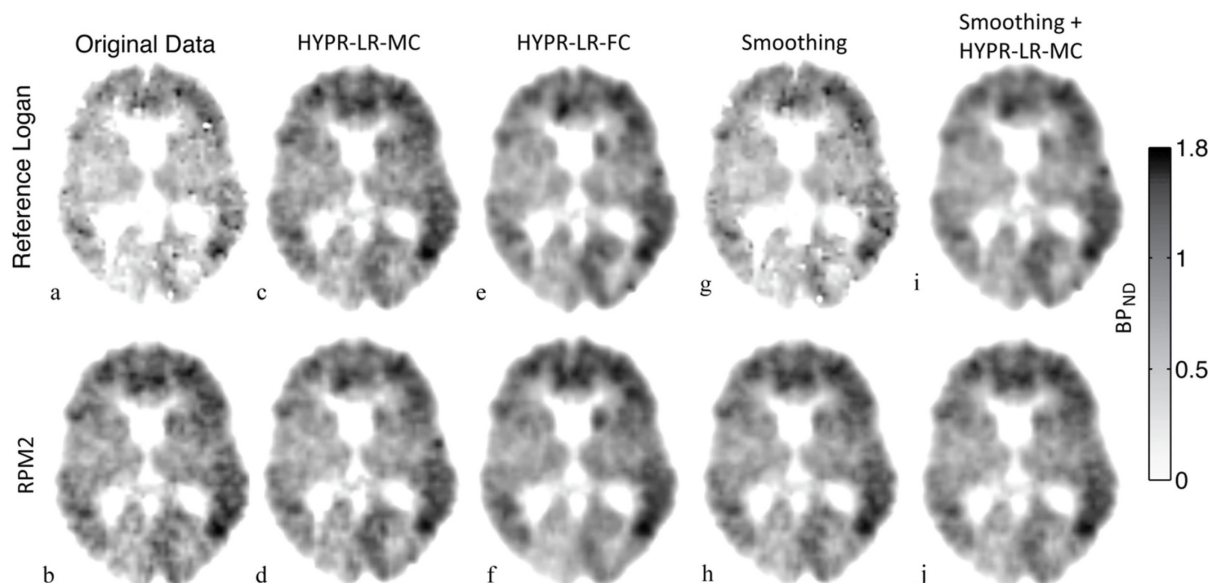


Figure 4.4. An illustrative example from a human [C-11]PIB dataset showing the effects of HYPR-LR processing on parametric images. The unprocessed data are predictably noisy and the Logan image (a) appears biased compared to the RPM2 image (b). HYPR-LR processing with a 9 mm FWHM Gaussian kernel improves the variance of both Logan and RPM2 parametric images (c-f). HYPR-LR-FC reduces variance more than HYPR-LR-MC processing, but the HYPR-LR-MC results are likely less biased. Spatial smoothing with a $3 \times 3 \times 3$ mm³ Gaussian results in improved variance with a corresponding loss of spatial resolution (g & h). HYPR-LR processing can also be done following smoothing to provide a further improvement in variance without any additional loss of spatial resolution, demonstrated here with HYPR-LR-MC (i & j).

the greatest reduction in variance in both the Logan and RPM2 parametric images in exchange for a slight inappropriate enhancement of the contrast between white matter and the cortex. HYPR-LR-FC likewise reduces the noise-dependent Logan bias. Smoothing with a $3 \times 3 \times 3$ mm³ FWHM Gaussian results in some improvement of the variance and bias of the Logan image, and qualitatively improves the variance in the RPM2 image to a similar degree as HYPR-LR-MC processing at the cost of some blurring. HYPR-LR processing can also be done in addition to spatial smoothing to further reduce variance. This is demonstrated in Figure 4.4 with HYPR-LR-MC.

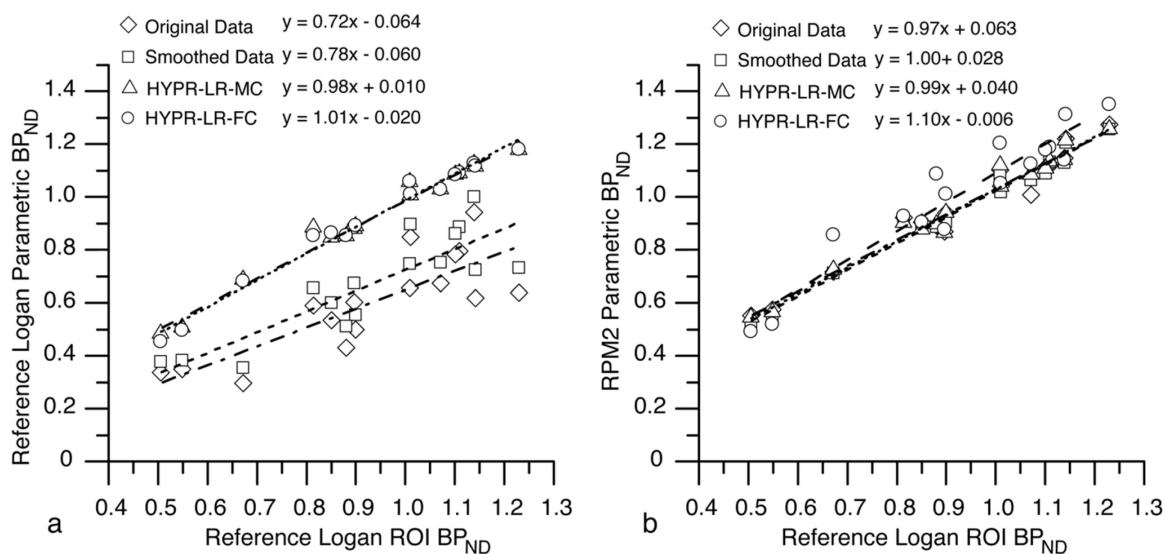


Figure 4.5. Bias in the [C-11]PIB human data. BP_{ND} values obtained from ROIs drawn on the parametric Logan (a) and RPM2 (b) images were compared to the BP_{ND} values obtained from the TACs of the same ROIs with the reference region Logan graphical method. Each point on the graphs represents the BP_{ND} from either the frontal or parietal cortex of one of the eight [C-11]PIB positive scans studied. Linear fits to the BP_{ND} values obtained using different types of processing are also shown with their corresponding equations (— = original data, --- = smoothed, = HYPR-LR-MC, - - - = HYPR-LR-FC). A deviation of the slope from unity or a y-intercept other than zero indicates the presence of a bias.

To evaluate bias in the human data, voxel BP_{ND} values averaged over frontal and parietal cortex ROIs from all eight datasets were compared with standard BP_{ND} values obtained from TACs averaged over the same ROIs using the reference Logan method. HYPR-LR-FC and HYPR-LR-MC reduce both the bias and variance of the Logan parametric image derived BP_{ND} values as the slopes of the linear fits approach unity and all the data points fall closely around their respective fits (Figure 4.5a). Spatial smoothing also reduces some of the noise-dependent Logan bias, but much less than HYPR-LR processing. The results from the RPM2 parametric images largely reflect what is seen in the simulated data. There appears to be little bias in the RPM2 images of the original data and the HYPR-LR-MC processed data. HYPR-LR-FC does introduce a positive bias, seen in the increased BP_{ND} values and the increase of the slope of the

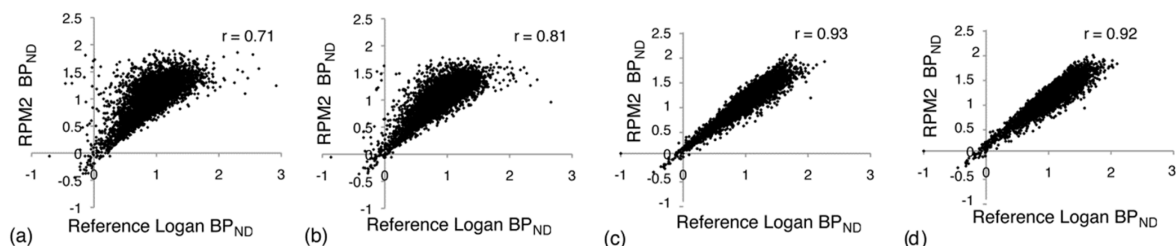


Figure 4.6. Voxel BP_{ND} values obtained with the Logan graphical method and RPM2 plotted against each other from a representative [C-11]PIB study. The parametric images generated from the original data (a) are compared with those generated from the data smoothed with a $3 \times 3 \times 3 \text{ mm}^3$ FWHM Gaussian (b), HYPR-LR-MC (c), and HYPR-LR-FC (d). The correlation between the two analysis methods, measured here with the Pearson correlation coefficient (r), gives an indication of the variance of the parametric images.

fit from 0.97 to 1.1. Smoothing does not bias the slope of the fit, but it does reduce the y-intercept of the fit from 0.063 to 0.028, and all of the smoothed BP_{ND} values fall slightly below the original values.

Finally, variance in the human data was evaluated semi-quantitatively by plotting voxel values from Logan and RPM2 parametric images against each other. An illustrative example of all voxels in the parietal and frontal cortex of the same dataset shown in Figure 4.4 demonstrates that HYPR-LR increases the correlation between BP_{ND} values derived from the different analysis methods, indicating a reduction in variance (Figure 4.6). When the correlation coefficients of all the [C-11]PIB datasets are compared following spatial smoothing and HYPR-LR processing using paired t-tests, all of the denoising methods significantly increase the correlation between Logan and RPM2 BP_{ND} values ($p < 0.01$, Table 4.2). There is not a significant difference between the correlation coefficients for HYPR-LR-MC and HYPR-LR-FC ($p > 0.05$), but HYPR-LR-MC and HYPR-LR-FC both significantly increase the correlation over smoothing with a $3 \times 3 \times 3 \text{ mm}^3$ Gaussian. The lower correlation coefficient of the smoothed data is due mostly to the higher noise in the Logan parametric images.

Table 4.2. The mean and range of Pearson correlation coefficients obtained from a linear fit to the voxel-by-voxel comparisons of the reference region Logan method and RPM2 for each of the 8 human [C-11]PIB datasets. The mean correlation coefficient was significantly improved with each of the denoising methods over the original data (*, $p < 0.01$). There was no difference between the two implementations of HYPR-LR ($p > 0.05$), but they both increased the mean correlation coefficient more than simple smoothing (+, $p < 0.01$).

	Original Data	Smoothed	HYPR-LR-MC	HYPR-LR-FC
Mean Pearson-r (Range)	0.62 (0.42-0.88)	0.71* (0.51-0.82)	0.94*+ (0.91-0.98)	0.93*+ (0.89-0.98)

4.5 Discussion

In this chapter, the potential of HYPR-LR to improve variance in both individual time frames and quantitative parametric images has been evaluated in the context of PET tracer data. The proposed optimized implementation of the algorithm using multiple composite images (HYPR-LR-MC), which will ideally provide the maximum improvement in noise while introducing no bias, has been compared to an implementation using all study frames to form the composite image (HYPR-LR-FC), which will provide the maximum possible improvement in noise but potentially introduce bias. HYPR-LR processing has also been compared to spatial smoothing.

The results show that HYPR-LR-FC processing can potentially introduce bias into border regions in individual time frames and parametric images. This bias will be dependent on differences in contrast that exist between individual frames and the composite image. Bias caused by HYPR-LR-FC can be visualized in the noise-free simulated data of individual time frames (Figure 4.1b), TACs (Figure 4.1d), and parametric images (Figure 4.2). This bias was also quantified in the noisy simulated data (Figure 4.3), and in parametric images of the human data (Figure 4.5). While the bias introduced by HYPR-LR-FC is relatively small when averaged

over all individual time frames, it makes a more significant impact on the parametric images, particularly those created with RPM2 (Figure 4.3 & Figure 4.5).

HYPR-LR-MC processing virtually eliminates the bias caused by HYPR-LR. The simulated data show that individual time frames and parametric images are essentially unbiased following HYPR-LR-MC processing (Figure 4.1-Figure 4.3), and the human parametric images confirm this (Figure 4.4 & Figure 4.5).

Bias can also be limited if a smaller kernel size is used with HYPR-LR-FC. In this work, the smallest kernel used was a Gaussian with a FWHM of $3 \times 3 \times 3 \text{ mm}^3$, only slightly larger than the thickness of the cerebral cortex, the primary object of interest in [C-11]PIB data. For the simulated data studied here, HYPR-LR-FC with this size kernel performed particularly well with regard to bias when the data were analyzed with RPM2, only introducing slightly more bias than HYPR-LR-MC with a large 9 mm FWHM filtering kernel (5.39% versus 3.73%). HYPR-LR-FC with the smaller kernel size did not provide as much of a benefit to the Logan parametric images, as BP_{ND} values are still relatively biased (Figure 4.3b).

Both methods of implementing HYPR-LR reduce variance in individual time frames and parametric images. HYPR-LR-FC processing with a larger filtering kernel gives the greatest reductions in variance (Figure 4.3 & Figure 4.4). This is not surprising, as each frame in a study is given the noise properties of the fully summed composite image. Processing with HYPR-LR-MC reduces variance most significantly in parametric images generated with the Logan graphical method, and in RPM2 parametric images to a lesser extent (Figure 4.3, Figure 4.4, Figure 4.6, & Table 4.2). As expected, a larger kernel size results in better variance reduction with HYPR-LR-MC while introducing little or no additional bias. A larger kernel likewise improves the variance reduction with the HYPR-LR-FC algorithm, but more bias is introduced (Figure 4.3). Using

HYPR-LR-FC with a small filtering kernel may therefore be desirable in some applications. For example, when the simulated data are analyzed with RPM2, HYPR-LR-FC with a smaller kernel still achieves good variance reduction (from 16.6% to 8.7%) while introducing little bias, as discussed above.

In this work, HYPR-LR processing has been compared to simple spatial smoothing. While many other denoising methods have been developed, spatial smoothing remains one of the most common ways to control noise in PET data. In addition, the processing time required for HYPR-LR will not be substantially longer than the time required to spatially smooth each frame. Processing time will largely be determined by the number of convolution operations that must be performed, and in this work the number of convolutions required for HYPR-LR-MC processing is 1.6 times greater than the number required to spatially smooth each frame.

Individual frames processed with HYPR-LR compare very favorably to frames that have been spatially smoothed (Figure 4.3a). HYPR-LR also compares favorably to spatial smoothing when the data are analyzed with the reference Logan graphical method (Figure 4.3b, Figure 4.4, & Figure 4.5). The improvements offered by HYPR-LR are less dramatic compared to simple smoothing when parametric images are created with RPM2. HYPR-LR-MC provides less noise reduction than smoothing with the $3 \times 3 \times 3 \text{ mm}^3$ FWHM Gaussian, though spatially smoothed BP_{ND} values are slightly more biased (Figure 4.3c & Figure 4.4). HYPR-LR-FC using the $3 \times 3 \times 3 \text{ mm}^3$ FWHM Gaussian kernel does provide more variance reduction than spatially smoothing with a $3 \times 3 \times 3 \text{ mm}^3$ FWHM Gaussian for a comparable amount of bias (Figure 4.3c), although the bias caused by HYPR-LR-FC is not due to any loss of spatial resolution. HYPR-LR processing can also be done in addition to spatial smoothing to provide further reductions in variance without any additional loss of spatial resolution (Figure 4.3 & Figure 4.4).

In the future, HYPR-LR must be considered more fully in the context of other denoising methods, for example wavelet denoising and iterative image reconstruction algorithms, including the numerous proposed approaches to 4-dimensional (4-D) PET reconstruction (Turkheimer *et al* 1999, Turkheimer *et al* 2000, Lin *et al* 2001, Cselenyi *et al* 2002, Turkheimer *et al* 2003, Alpert *et al* 2006, Rahmim *et al* 2009). As HYPR-LR uses temporally integrated data to reduce noise, comparing it to denoising methods that likewise utilize the time domain, such 4-D reconstructions, will be particularly important. Iterative reconstructions, wavelet denoising, and HYPR-LR have all demonstrated an ability to substantially reduce noise, but each also has drawbacks. A full comparison between HYPR-LR and these other denoising processes, explicitly examining the pros and cons of each, is beyond the scope of the current work and will likely depend on the specific imaging task. Furthermore, as demonstrated here with spatial smoothing, HYPR-LR could easily complement these other denoising techniques. This is particularly relevant for performing HYPR-LR on OSEM reconstructions, which are now routinely done on both clinical and research scanners and provide some noise control themselves.

This work has shown that following HYPR-LR processing, Logan and RPM2 analysis perform comparably. After denoising with HYPR-LR-MC and HYPR-LR-FC, both the COV and the bias are similar between the Logan and RPM2 images (Figure 4.3-Figure 4.6). If anything, after HYPR-LR processing the greater bias is seen with RPM2 with little additional benefit in variance reduction (Figure 4.3c & Figure 4.5b). In addition, in this application the performance of RPM2 was more variable and sensitive to user selected parameters. In particular, the minimum k_{2a} value used in this work was slightly greater than that predicted by non-linear SRTM fits to ROI TACs, and greater than the value previously reported for [C-11]PIB analysis (Yaqub *et al* 2008). There was also a slight positive bias in the BP_{ND} values obtained with RPM2

in the simulations (Figure 4.3c). This might be because the assumption of a simplified reference tissue model does not adequately describe the kinetics of [C-11]PIB in this case (Price *et al* 2005). While the objective of this work is not to determine the best way to analyze [C-11]PIB data, the increased reliability and greater robustness seen with Logan analysis following HYPR-LR processing may prove valuable, as the Logan method is easy to implement, does not assume any particular model, and does not require imposing limits on the data, for example the range of k_{2a} in RPM2.

Presumably, HYPR-LR processing should also improve other data driven methods, such as the multi-linear regression methods that are not susceptible to a noise-sensitive bias but do exhibit greater variance than the Logan graphical method (Ichise *et al* 2002, Logan 2003). Likewise, it should improve other model based methods like compartmental analysis.

The results presented here suggest that HYPR-LR-MC and HYPR-LR-FC may have value in different contexts. HYPR-LR-MC introduces minimal bias into the data, but the bias introduced by HYPR-LR-FC is not that great, particularly when a smaller filtering kernel is used. And while HYPR-LR-MC reduces variance, HYPR-LR-FC does so to a greater degree. When the focus is on relatively large regions of high uptake in [C-11]PIB data, HYPR-LR-FC performs relatively well. However, caution should still be exercised when using all frames of the study to form the composite image. In the case of [C-11]PIB, it appears as if the bias caused by HYPR-LR-FC results in greater contrast between structures in the brain. While such an image may be appealing to look at, it may be a misleading result. Bias caused by HYPR-LR will also likely be greater in studies that have greater contrast between areas of interest and their surrounding background, for example [C-11]raclopride or any of a number of tracers used to study tumor biology. It is clear that using HYPR-LR with composite images that have been formed in a way that accounts for

the kinetic behavior of the tracer being studied can certainly provide an improvement in the variance of kinetic parameters while introducing very little bias.

While the focus of this chapter has been the application of HYPR-LR processing to [C-11]PIB data, a tracer of interest in the neuroscience community, the approach presented here should be generalizable to other tracers and other applications outside the brain. Indeed, the fairly detailed structure of the brain, and of the cortex in particular, provides a good means of testing HYPR-LR processing. HYPR-LR processing may prove particularly valuable for providing more detailed physiologic information on a smaller anatomical scale for cardiac and oncology applications of dynamic PET imaging. Not all tracers will follow the exact uptake pattern we have described, and the optimal composite scheme, including simply using a fully summed composite, will depend on the application.

4.6 Conclusion

HYPR-LR is a promising denoising technique for a number of medical imaging modalities, including dynamic PET imaging. This chapter has evaluated the tradeoff between bias and variance seen with HYPR-LR processing in the context dynamic PET tracer data, with a focus on kinetic analysis. HYPR-LR processing significantly improves the variance of both individual time frames and quantitative parametric images, and the proposed implementation using multiple composite images does so while introducing little bias. This work also provides a framework for testing the validity of HYPR-LR processing in the context of a given tracer and analysis method. In the future, HYPR-LR may prove particularly valuable in PET applications that suffer from high noise, such as PET scans requiring high spatial or temporal resolution, vulnerable patient populations who require less radiation dose, tracers used to screen large populations, and tracers

utilizing unique but dosimetry limited radionuclides such as [I-124] and [Cu-64]. HYPR-LR is a simple denoising tool, and the proposed method for its quantitatively accurate implementation could easily be implemented for different tracer behaviors, or for individual studies.

References

- Alpert, N M, Reilhac, A, Chio, T C and Selesnick, I 2006 Optimization of dynamic measurement of receptor kinetics by wavelet denoising *Neuroimage* **30** 2 444-51
- Brix, G, Zaers, J, Adam, L E, Bellemann, M E, Ostertag, H, Trojan, H, Haberkorn, U, Doll, J, Oberdorfer, F and Lorenz, W J 1997 Performance evaluation of a whole-body PET scanner using the NEMA protocol. National Electrical Manufacturers Association *J. Nucl. Med.* **38** 10 1614-23
- Cselenyi, Z, Olsson, H, Farde, L and Gulyas, B 2002 Wavelet-aided parametric mapping of cerebral dopamine D2 receptors using the high affinity PET radioligand [11C]FLB 457 *Neuroimage* **17** 1 47-60
- Gunn, R N, Lammertsma, A A, Hume, S P and Cunningham, V J 1997 Parametric imaging of ligand-receptor binding in PET using a simplified reference region model *Neuroimage* **6** 4 279-87
- Herzog, H, Tellman, L, Pietrzyk, U, Casey, M E and Kuwert, T 2004 NEMA NU2-2001 Guided Performance Evaluation of Four Siemens ECAT PET Scanners *IEEE Trans Nucl Sci* **51** 5 2662-9
- Ichise, M, Toyama, H, Innis, R B and Carson, R E 2002 Strategies to improve neuroreceptor parameter estimation by linear regression analysis *J. Cereb. Blood Flow Metab.* **22** 10 1271-81
- Lammertsma, A A and Hume, S P 1996 Simplified reference tissue model for PET receptor studies *Neuroimage* **4** 3 Pt 1 153-8
- Lin, J W, Laine, A F and Bergmann, S R 2001 Improving PET-based physiological quantification through methods of wavelet denoising *IEEE Trans. Biomed. Eng.* **48** 2 202-12
- Logan, J 2003 A review of graphical methods for tracer studies and strategies to reduce bias *Nucl. Med. Biol.* **30** 8 833-44
- Logan, J 2000 Graphical analysis of PET data applied to reversible and irreversible tracers *Nucl. Med. Biol.* **27** 7 661-70
- Logan, J, Fowler, J S, Volkow, N D, Wang, G J, Ding, Y S and Alexoff, D L 1996 Distribution volume ratios without blood sampling from graphical analysis of PET data *J. Cereb. Blood Flow Metab.* **16** 5 834-40

Logan, J, Fowler, J S, Volkow, N D, Wolf, A P, Dewey, S L, Schlyer, D J, MacGregor, R R, Hitzemann, R, Bendriem, B and Gatley, S J 1990 Graphical analysis of reversible radioligand binding from time-activity measurements applied to [N-11C-methyl]-(-)-cocaine PET studies in human subjects *J. Cereb. Blood Flow Metab.* **10** 5 740-7

Lopresti, B J *et al* 2005 Simplified quantification of Pittsburgh Compound B amyloid imaging PET studies: a comparative analysis *J. Nucl. Med.* **46** 12 1959-72

Price, J C, Klunk, W E, Lopresti, B J, Lu, X, Hoge, J A, Ziolkowski, S K, Holt, D P, Meltzer, C C, DeKosky, S T and Mathis, C A 2005 Kinetic modeling of amyloid binding in humans using PET imaging and Pittsburgh Compound-B *J. Cereb. Blood Flow Metab.* **25** 11 1528-47

Rahmim, A, Tang, J and Zaidi, H 2009 Four-dimensional (4D) image reconstruction strategies in dynamic PET: beyond conventional independent frame reconstruction *Med. Phys.* **36** 8 3654-70

Slifstein, M and Laruelle, M 2000 Effects of statistical noise on graphic analysis of PET neuroreceptor studies *J. Nucl. Med.* **41** 12 2083-8

Turkheimer, F E, Aston, J A, Banati, R B, Riddell, C and Cunningham, V J 2003 A linear wavelet filter for parametric imaging with dynamic PET *IEEE Trans. Med. Imaging* **22** 3 289-301

Turkheimer, F E, Banati, R B, Visvikis, D, Aston, J A, Gunn, R N and Cunningham, V J 2000 Modeling dynamic PET-SPECT studies in the wavelet domain *J. Cereb. Blood Flow Metab.* **20** 5 879-93

Turkheimer, F E, Brett, M, Visvikis, D and Cunningham, V J 1999 Multiresolution analysis of emission tomography images in the wavelet domain *J. Cereb. Blood Flow Metab.* **19** 11 1189-208

Wu, Y and Carson, R E 2002 Noise reduction in the simplified reference tissue model for neuroreceptor functional imaging *J. Cereb. Blood Flow Metab.* **22** 12 1440-52

Yaquib, M, Tolboom, N, Boellaard, R, van Berckel, B N, van Tilburg, E W, Luurtsema, G, Scheltens, P and Lammertsma, A A 2008 Simplified parametric methods for [11C]PIB studies *Neuroimage* **42** 1 76-86

Zubal, I G, Harrell, C R, Smith, E O, Rattner, Z, Gindi, G and Hoffer, P B 1994 Computerized three-dimensional segmented human anatomy *Med. Phys.* **21** 2 299-302

Chapter 5. Non-linear Spatio-temporal Filtering of Dynamic PET Data Using a Low-Pass Filter with Expectation-Maximization Deconvolution

5.1 Introduction

The second novel denoising method for dynamic positron emission tomography (PET) presented in this thesis is spatio-temporal expectation-maximization (STEM) filtering. This thesis has so far demonstrated that Highly constrained back-Projection-Local Reconstruction (HYPR-LR) is an effective method for reducing noise in dynamic PET data and improving kinetic analysis. Furthermore, HYPR-LR can be tailored to specific imaging tasks and applications to improve noise while introducing little bias. However, application of HYPR-LR processing to specific tasks does require *ad hoc* selection of parameters used in the algorithm, which can be somewhat arbitrary. A 4-dimensional (4-D) denoising method that requires less adjustment but that is still simple, effective, and suited to a wide range of dynamic PET applications could thus be of value.

5.2 Chapter Aims

The aim of this chapter is to present STEM as a 4-D filtering algorithm that is simple, requires little adjustment, and can be applied to a wide range of dynamic PET studies. A method that filters data in the time domain alone, temporal EM (TEM) filtering is also presented, though as will be shown the benefits obtained with TEM filtering are less than those obtained with STEM. STEM and TEM filtering couple two well established methods: low-pass filtering followed by expectation-maximization (EM), or Richardson-Lucy, deconvolution (Richardson 1972, Lucy 1974). In principle, the initial 4-D filter suppresses noise at a broad range of spatial

and temporal frequencies and the subsequent deconvolution recovers the frequencies most important to the signal after only a few iterations. This approach is similar to early termination of EM reconstruction, which improves noise at the cost of a slight degradation in resolution. However, because STEM filtering is 4-D, a substantial degree of noise is averaged out with little loss of signal. As TEM only filters temporal data, less noise will be reduced but there will be no loss of spatial resolution. In addition, because STEM and TEM use EM deconvolution, they are data driven processes and will produce a unique filter for a given dataset. STEM and TEM filtering are facilitated by two non-traditional approaches to the filtering process. Namely, time-activity curves (TACs) are transformed to an image frame number domain, and the filtering kernel is shift-variant.

The aim of this chapter is to introduce the STEM filtering methodology. The next chapter will evaluate the method's performance on PET data.

5.3 Theory

5.3.1 Initial Filtering

The goal of STEM and TEM filtering is to suppress temporal (and in the case of STEM spatial) noise in the initial filtering step, and then to restore the frequencies most important to the signal using EM deconvolution. The initial step for STEM filtering can be described as:

$$g_{i,j} = (f \otimes' S)_{i,j} \quad (5.1)$$

where $f_{i,j}$ is the original 4-dimensional dataset, denoted by the spatial dimension, i , and the image frame dimension, j , $S_{i,j}$ is the 4-dimensional filter, $g_{i,j}$ is the filtered result, and \otimes' is a modified convolution process. The initial filtering step is the same for TEM filtering, but only the time domain is filtered. The filter for TEM is thus one dimensional, and can be represented as S_j . The

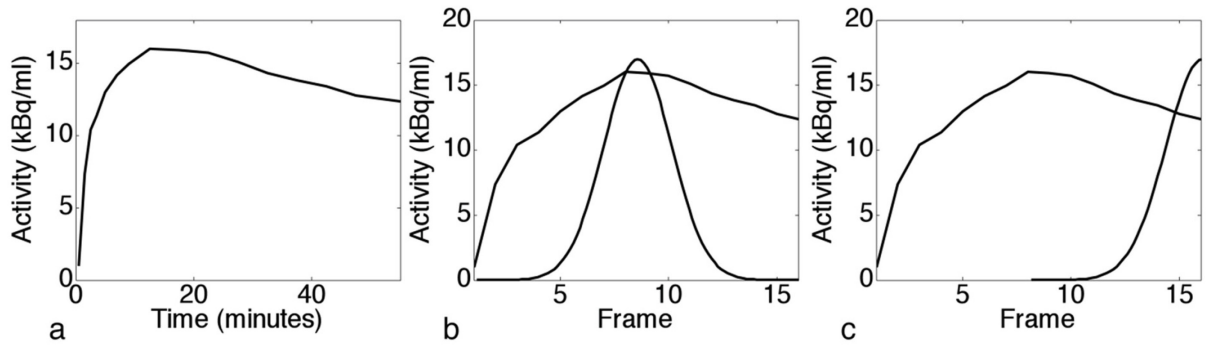


Figure 5.1. An illustration of the image frame domain component of STEM and TEM filtering. An initial voxel TAC (a) is transformed to the image frame domain and convolved with a shift-variant Gaussian (b) that is truncated at the beginning (not shown) and end (c) of the curve.

convolution process employed is distinct from standard convolution in two important ways: the temporal component takes place in the image frame domain, as opposed to the time domain, and the convolution is shift-variant.

5.3.1 Filtering in the Image Frame Domain

Data filtered with STEM and TEM are transformed from the time domain to the image frame domain, filtered, and then transformed back to the time domain (Figure 5.1a & b). Practically, the transformation from the time domain to the frame domain and from the frame domain back to time is trivial. More formally, it can be described by the invertible matrix operations:

$$XT=F \quad (5.2)$$

$$X^{-1}F=T \quad (5.3)$$

where X is a diagonal transformation matrix whose diagonal elements are equal to the frame numbers divided by their respective mid-point times, T is a vector of the mid-point times of each frame, and F is a vector of the frame numbers.

Filtering in the frame domain can help minimize bias caused by STEM filtering while maximizing the noise reduction it provides. Dynamic PET studies are typically sampled asymmetrically, with finer sampling early in a study when tracer kinetics are changing rapidly and coarser sampling as the study progresses. Such a sampling scheme maximizes frame durations to reduce noise while still sampling at an adequate rate to capture changes in the signal, limiting the change in tracer activity from one frame to the next. This will limit the amount the temporal signal is smoothed by the initial filter, particularly at early frames, making the restoration of the signal easier. In addition, by filtering in the frame domain, rather than interpolating to a uniform sampling rate and filtering in the time domain, STEM filtering provides the maximum averaging of noise between frames.

5.3.3 Shift-Variant Convolution

The convolution operation used in STEM and TEM filtering is distinct from standard convolution because it is shift-variant. In particular, the filtering kernel is truncated at the beginning and end of the frame domain. This approach is required as TACs are not periodic and not compactly supported. Standard approaches to convolving discrete data such as circular convolution and zero-padding would be incorrect and thus cannot be used. The filtering kernel is truncated by simply ignoring the elements of the kernel that fall outside the frame domain during the convolution (Figure 5.1c). Any kernel that is truncated must be normalized only by the area falling within the image frame domain.

For STEM filtering, the modified 4-dimensional convolution between the dynamic PET data $f_{i,j}$ with M frames indexed by $j = 1, 2, \dots, M$, and the filtering kernel S , with $2N+1$ elements in the image frame domain indexed by $j = -N, -N+1, \dots, 0, \dots, N-1, N$, and $2P+1$ elements in the spatial domain indexed by $i = -P, -P+1, \dots, 0, \dots, P-1, P$, can be represented as:

for $j=1$ to N

$$(f \otimes S)_{i,j} = \frac{\sum_{i'=-P}^P \sum_{j'=-N}^{j-1} f_{i-i', j-j'} S_{i', j'}}{\sum_{i'=-P}^P \sum_{j'=-N}^{j-1} S_{i', j'}} \quad (\text{a})$$

for $j = N + 1$ to $M - N$

$$(f \otimes S)_{i,j} = \frac{\sum_{i'=-P}^P \sum_{j'=-N}^N f_{i-i', j-j'} S_{i', j'}}{\sum_{i'=-P}^P \sum_{j'=-N}^N S_{i', j'}} \quad (\text{b}) \quad (5.4)$$

for $j = M - N + 1$ to M

$$(f \otimes S)_{i,j} = \frac{\sum_{i'=-P}^P \sum_{j'=j-M}^N f_{i-i', j-j'} S_{i', j'}}{\sum_{i'=-P}^P \sum_{j'=j-M}^N S_{i', j'}} \quad (\text{c})$$

As PET images are typically compactly supported in space, no special normalization in the spatial domain is included in Equation 4.2, though it could easily be done if required. For TEM filtering, the spatial dimension would simply be omitted. The kernel would still be truncated at the beginning and end of the time domain.

5.3.4 EM Deconvolution

After the initial filtering step, EM deconvolution is performed to recover the frequencies most important to the signal. For STEM filtering, this can be described as:

$$y_{i,j}^{n+1} = y_{i,j}^n \left(\frac{g_{i,j}}{(y^n \otimes S)_{i,j}} \otimes S \right)_{i,j} \quad (5.5)$$

where $y_{i,j}^n$ is the STEM filtered result after n iterations, and $g_{i,j}$ is the dynamic data after the initial filtering (Equation 5.1). Again, for TEM filtering, the filter is 1-dimensional.

The reduction in noise from the initial filtering step is sustained by terminating EM deconvolution after only a few iterations. Because the initial filter is 4-dimensional, it can be made relatively small in each dimension to limit the degradation of the signal and still reduce noise to a substantial degree. A few EM deconvolution iterations should thus be all that is needed to largely restore the temporal and spatial frequencies that dominate the signal, while noise is still largely suppressed. This is empirically demonstrated in the next chapter.

5.3.5 Filter Magnitude

The magnitude of the effective filter used for TEM and STEM filtering is revealing. Because the filtering kernel is shift variant, its magnitude in the Fourier transform of the frame domain is not Gaussian. The magnitude of an example filter with a FWHM of 4 frames in the frame domain is shown in Figure 5.2a. The magnitude of this filter in the frame frequency domain was found as:

$$\frac{|FFT_j(f \otimes S)_{p,j}|}{|FFT_j(f_{p,j})|} \quad (5.6)$$

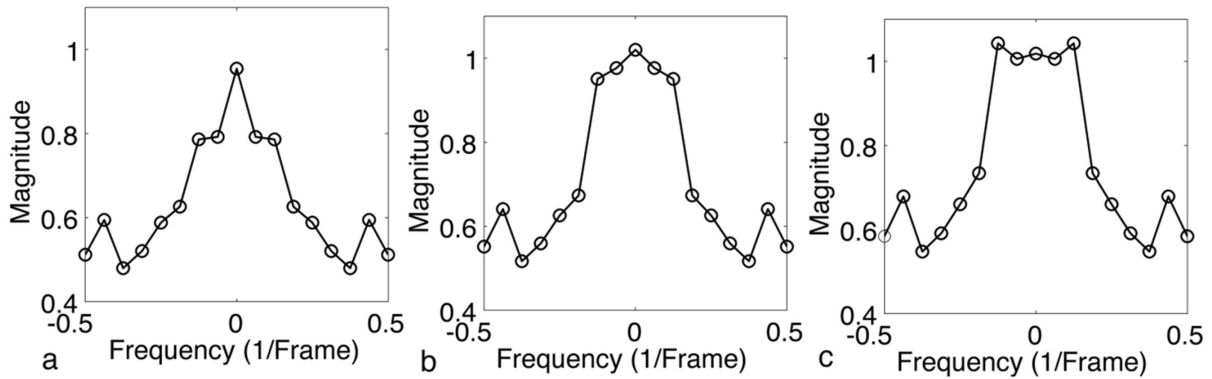


Figure 5.2. The magnitude of the effective filter in frame frequency space after the initial filter (a), after 3 deconvolution iterations (b), and after 5 deconvolution iterations (c) demonstrates the progressive recovery of lower frequencies.

where FFT_j is the discrete Fourier transform of the frame domain, $f_{p,j}$ is a frame-activity curve (FAC) from a striatal voxel, $i=p$, in a simulated [C-11]raclopride dataset, and $(f \otimes S)_{p,j}$ is the FAC of the same voxel following filtering. The magnitude of the effective filter following EM deconvolution with equation 3 demonstrates the rapid recovery of lower frequencies, and the progressive recovery of higher frequencies (Figure 5.2e & f). It is also interesting to note that there is an increase in the filter's magnitude as it approaches the Nyquist frequency, reflecting the fact that the filtering process preserves the sharp edge at the abrupt end of the FAC.

5.3.6 Filter Parameter Selection

The factors most important to the adequate recovery of signal in TEM and STEM filtering are the size of the initial filter and the number of EM iterations performed. The spatial frequencies present in typical dynamic PET studies are relatively high compared to the frequencies present in the frame-activity domain (Figure 5.3). An asymmetric Gaussian filtering kernel is therefore proposed for STEM filtering, whose full width at half maximum (FWHM) is wider in the frame domain than in the spatial domain to limit the degradation of spatial frequencies. The results

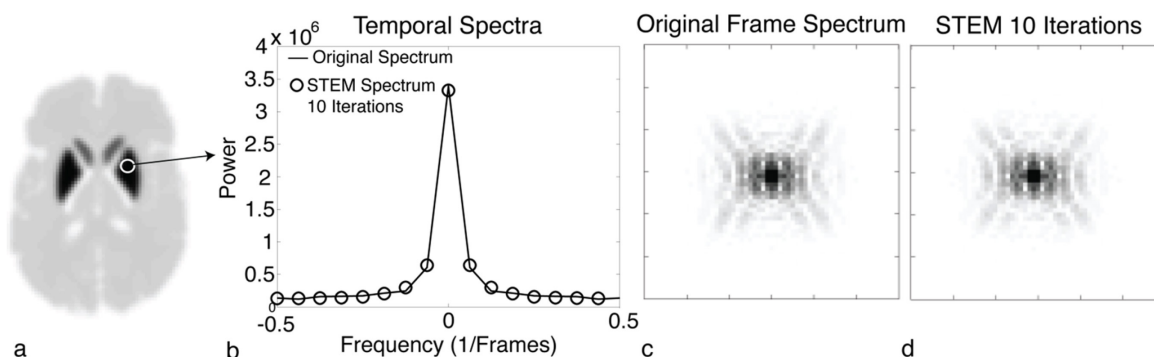


Figure 5.3. The spectral properties of an example [C-11]raclopride TAC (a & b) and frame (a, c, & d). If the first frame is excluded in the STEM filtered result (i.e. reset to its initial value), the temporal frequencies most important to the example TAC are almost entirely restored after 10 STEM iterations (b). The spatial frequencies are also largely restored, though there is a subtle loss of mid-level and high frequencies (c & d).

presented in the next chapter demonstrate that STEM filtering with a Gaussian filtering kernel with a FWHM approximately equal to the resolution of the scanner in each spatial dimension and a FWHM of 4 frames in the image frame dimension performs quite well, with minimal introduced bias and significant noise suppression. TEM filtering performs well using a Gaussian with a FWHM of 4 frames.

Using kernels of this size, the temporal (and spatial) frequencies most important to the data studied in this thesis are largely restored after 10 iterations. If the first frame is left unfiltered, the spectrum of an example [C-11]raclopride TAC filtered with STEM is almost entirely restored after 10 iterations (Figure 5.3 a & b). The spatial frequencies from an example [C-11]raclopride slice are also largely restored, though there is some visible degradation of the higher frequencies (Figure 5.3 c & d).

Kernel size and the number of iterations required are interrelated. Adjusting either one will impact the degree to which the original signal is restored and noise is suppressed. The size of the

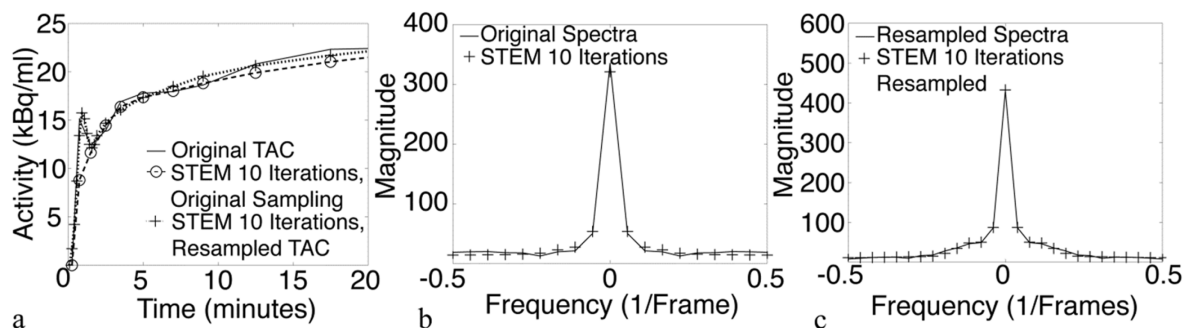


Figure 5.4. The effects of temporal sampling on the ability of STEM filtering to restore the original signal. An example [F-18]FDOPA TAC shows a sharp peak in the first minute of the study (a). If STEM filtering is applied the original sampling scheme, this peak is lost. As a result, the frequency spectrum of the STEM filtered TAC does not perfectly match the spectrum of the original TAC (b). If the first 2 minutes of the study are resampled to 10 second frames, STEM filtering better preserves the initial peak, and the frequency spectra of the resampled TAC and the STEM filtered TAC are nearly equivalent (c).

filtering kernel and the number of iterations suggested above were determined empirically, as illustrated in the following chapter. The noise suppression obtained with smaller kernels is not as good, even though fewer iterations are required, because the initial amount of noise suppression is less. Likewise, larger kernels provide little benefit relative to the extra number of iterations required.

5.3.7 Effects of Temporal Sampling

The restoration of the temporal signal will also be dependent on the temporal sampling scheme. Ideally, a study should be sampled such that the percent change in activity from frame to frame should be similar throughout the study. If TACs have not been sampled at an adequate rate, STEM and TEM filtering will have difficulty fully restoring them. For example, for the [F-18]FDOPA striatal TAC shown in Figure 5.4, the initial sampling scheme (2x30 seconds, 3x1, 3x2, 4x5, and 6x10 minute frames) does not sufficiently sample the initial part of the study to

preserve the sharp peak in the first minute following STEM filtering. If the first two minutes of the study are effectively re-sampled by interpolating to 10 second frames, higher frequencies are less prominent in the resulting frame frequency spectrum, and STEM filtering restores the initial peak far better than with the initial sampling scheme. The interpolation is an oversimplification of the true behavior of the [F-18]FDOPA TAC, but nevertheless illustrates the impact of sampling on the ability of STEM (and TEM) filtering to fully recover temporal signal. Although STEM and TEM filtering will better maintain the fidelity of the temporal signal when the data are sampled at a higher rate, the resulting frames will be noisier.

5.4 Summary

In this chapter, STEM has been presented as a spatio-temporal filtering method to reduce noise in dynamic PET data. TEM filtering has also been introduced as a method that filters temporal data only. Because STEM is a 4-dimensional process, a substantial degree of noise-averaging can be achieved with little loss of signal. Likewise, TEM filtering should reduce noise with no loss of spatial resolution and little effect on underlying temporal signals. The next chapter aims to demonstrate these properties in the context of dynamic PET data.

References

Lucy, L B 1974 An iterative technique for the rectification of observed distributions *AJ* **79** 6 745-754

Richardson, W H 1972 Bayesian-Based Iterative Method of Image Restoration *JOSA* **62** 1 55-59

Chapter 6. Evaluation of STEM and TEM Filtering

6.1 Chapter Aims

The previous chapter introduced spatio-temporal expectation-maximization (STEM) and temporal expectation-maximization (TEM) filtering and put them in a theoretical context. The aim of this chapter is to rigorously evaluate their performance on real positron emission tomography (PET) data, and to demonstrate the ideas proposed in the previous chapter. In particular, this chapter aims to demonstrate that STEM, and to a lesser degree TEM, filtering provide significant reductions in noise with little loss of signal. Similar to the evaluation of Highly constrained back-Projection-Local Reconstruction (HYPR-LR), this chapter illustrates the improvements in variance relative to introduced bias following STEM and TEM filtering in individual time frames and in parametric images generated with various kinetic analysis methods using phantom data, and simulated and human [C-11]raclopride and [F-18]FDOPA data. STEM and TEM filtering are compared to spatial smoothing.

6.2 Methods

6.2.1 Dual-Isotope Phantom

The same dual-isotope phantom used to evaluate HYPR-LR in Chapter 2 was used to evaluate STEM filtering. The details of the data acquisition are described in that chapter. The acquired data were reconstructed into 30x5 minute frames with filtered back-projection (FBP) using 3 different filters: a 2-dimensional (2-D) ramp filter with a frequency cutoff of 0.104 mm^{-1} , and 3-dimensional (3-D) Hann filters with frequency cutoffs of 0.104 and 0.065 mm^{-1} . Corrections for deadtime, normalization, and scatter were applied using the system software, and

attenuation correction was applied using the CT data. All reconstructions used an image matrix of 128x128x47 with voxel sizes of 3.125x3.125x3.27 mm³.

STEM and TEM filtering were applied to the ramp reconstruction, the highest resolution images. STEM filtering was applied using a 4-dimensional (4-D) Gaussian filter with a FWHM in the image frame domain of 4 frames and a FWHM in each of the 3 spatial dimensions of 6.25 mm. TEM filtering was performed using a 1-dimensional (1-D) Gaussian with a FWHM of 4 frames. STEM and TEM filtering were performed up to 10 iterations. As the only dynamic behavior in this study is two decaying exponentials, using frames of different durations would have little impact on the shape of the TACs. Uniform frames were thus used.

Bias in the time-series data was assessed using the percent contrast of the 13 mm sphere to the background at each frame over the course of the study using a volume of interest (VOI) drawn on the CT scan:

$$\text{Contrast (\%)} = \frac{13 \text{ mm Sphere (Bq/ml)} - \text{Background (Bq/ml)}}{\text{Background (Bq/ml)}} \times 100 \quad (6.1)$$

The coefficient of variation (COV) at each frame was assessed in a large VOI drawn on the CT scan in the F-18 background:

$$\text{COV (\%)} = \frac{\sigma_{\text{Background}}}{\mu_{\text{Background}}} \quad (6.2)$$

where $\sigma_{\text{Background}}$ is the standard deviation and $\mu_{\text{Background}}$ is the mean of the large background VOI.

6.2.2 [C-11]-Raclopride and [F-18]-FDOPA simulations

Simulated dynamic image datasets for [C-11]-raclopride and [F-18]-FDOPA were created using time-activity curves (TACs) derived from human studies of patients with Parkinson disease

and the Zubal brain phantom (Zubal *et al* 1994). Details of the access to these human data are described in the section below on the application of STEM filtering to actual human scans. TACs from the caudate nucleus, putamen, thalamus, white matter, and the frontal, parietal, temporal, and occipital cortex were obtained from human datasets and impressed onto the corresponding regions in the Zubal brain phantom. VOIs drawn on the human data were made as large as possible to limit noise. The [C-11]-raclopride TACs were obtained from a 60 minute study with 16 frames: 4x1, 3x2, 8x5, and 1x10 minutes in duration. [F-18]-FDOPA TACs were obtained from a 90 minute study with 18 frames: 2x30 seconds, 3x1, 3x2, 4x5, and 6x10 minutes in duration. As will be shown in the results below, these sampling schemes are not ideal as they result in bias in the early frames following STEM filtering. However, the merits of using TACs derived from human studies with adequate signal-to-noise ratios are chosen over resampling to noisier, more unreliable data, or simulating TACs with model derived rate constants.

Simulations were generated using the same methods described in Chapter 3 for [C-11]-PIB. Briefly, acquisitions of [C-11]-raclopride and [F-18]-FDOPA on an ECAT HR+ scanner were approximated using published performance information about the scanner model (e.g. resolution, sensitivity, etc...) (Brix *et al* 1997, Herzog *et al* 2004). Noise-free data were converted into counts by accounting for sensitivity, voxel volume, frame duration, and radioactive decay. Data were then forward projected using MATLAB's (The MathWorks®) 2-D radon transform to create 2-D sinograms, attenuated using an attenuation map derived from the Zubal phantom, and multiplied by the expected scatter fraction for the amount of activity used in the simulation. 40 noisy realizations of the emission sinograms for [C-11]-raclopride and [F-18]-FDOPA were then created by adding Poisson noise scaled by the number of counts at each position in the noise-free sinograms. Noisy sinograms were then corrected for attenuation, sensitivity, and scatter fraction,

and reconstructed with FBP using either a ramp filter with a frequency cutoff of 0.171 mm^{-1} , or a Hann filter with a frequency cutoff of 0.227 mm^{-1} and converted back into activity concentrations (Bq/ml). FBP reconstructions of the noise-free sinograms using the ramp filter were used as a standard to determine bias, as described below.

STEM and TEM filtering were performed on the ramp reconstructions, as these images will have the best initial spatial resolution. A 4-D Gaussian with a FWHM in the frame domain of 4 frames and a FWHM in each of the 3 spatial dimensions of 4.40 mm was used for STEM filtering, and a 1-D Gaussian with a FWHM of 4 frames was used for TEM filtering. Ten EM deconvolution iterations were performed for both STEM and TEM.

Bias was evaluated in the STEM and TEM filtered images and in the images reconstructed with the Hann filter. The bias of each voxel was taken as the percent difference between the mean of that voxel over the 40 noise realizations, μ_x , and that voxel's value in the noise-free FBP reconstruction, x :

$$\text{bias (\%)} = \frac{\mu_x - x}{x} \times 100 \quad (6.3)$$

Variance was assessed using the COV at each voxel:

$$\text{COV} = \frac{\sigma_x}{\mu_x} \quad (6.4)$$

where σ_x now represents the standard deviation of each voxel, as opposed an entire region in the phantom study (Equation 6.2). The mean bias and variance of all voxels in the striatum, the structure of primary interest for [C-11]-raclopride and [F-18]-FDOPA scans, were the principal measures taken from the simulated data.

6.2.3 Kinetic analysis of simulated data

Parametric images were generated from the simulated datasets using a number of kinetic analysis methods. Parametric images of the non-displaceable binding potential (BPND) were generated from the [C-11]-raclopride simulations, and parametric images of the normalized uptake rate constant, K_i^* , were generated from the [F-18]-FDOPA simulations. As stated in Chapter 4, the BPND is a parameter of primary interest in reversible tracer studies. The K_i^* is a similar aggregate measure for tracers that show irreversible binding behavior. In the case of [F-18]-FDOPA studies, K_i^* is typically interpreted as a marker of dopamine synthesis and storage (Sossi et al 2003).

BP_{ND} parametric images were created with the data driven reference region Logan graphical method (Logan *et al* 1990, Logan *et al* 1996) and the model based simplified reference tissue model (SRTM) basis function method (Lammertsma and Hume 1996, Gunn *et al* 1997), frequently referred to as receptor parametric mapping (RPM). Logan plots were fit from 30 to 60 minutes. Calculation of the abscissa values did not include the term involving the reference region efflux rate constant, k_2^{REF} , as it is known to be unimportant for [C-11]raclopride data (Logan 2000). RPM was performed using a fixed k_2^{REF} (RPM2, (Wu and Carson 2002)), determined by an SRTM fit to a TAC averaged over the entire striatum. The range of the efflux rate constant, k_{2a} , used in RPM2 was 0.035 to 0.2 min^{-1} , with 50 possible values (i.e. 50 basis functions). The minimum and maximum k_{2a} values were derived from SRTM fits to the TACs used to create the numerical phantom. A TAC from a large cerebellar VOI, obtained prior to STEM filtering, was used as the reference tissue TAC for all of the methods used to analyze [C-11]raclopride.

Parametric images of K_i^* were generated from the [F-18]FDOPA simulations with the reference region Patlak method (Patlak *et al* 1983, Patlak and Blasberg 1985). A TAC averaged over both occipital lobes was used as a reference region input (Patlak *et al* 1983, Patlak and Blasberg 1985, Brooks *et al* 1990). The Patlak plot was fit from 30-90 minutes. A more complete description of the kinetic analysis methods used is included in Appendix A.

The bias and variance in the resulting parametric images were analyzed in the same way as they were for the time-series data. Bias was found using Equation 6.3, with the true voxel value, x , equal to the voxel's value in the parametric image of the noise-free FBP reconstruction. The COV of each voxel was found for each analysis method using Equation 6.4. The voxel bias and COV were averaged over all striatal voxels in the parametric images.

Human [C-11]Raclopride and [F-18]FDOPA scans

The performance of STEM filtering on actual PET studies in humans was evaluated using anonymized archived dynamic image data from two separate research protocols. TEM filtering was not evaluated in the human data based upon the limited improvements seen in the simulated parametric images. [C-11]raclopride scans of Parkinson disease patients were acquired on a Siemens HRRT scanner at the University of British Columbia. Data were acquired in list-mode over 60 minutes and reconstructed with 3-D ordinary Poisson ordered subset EM (OP-OSEM) into 16 frames with durations of 4x1, 3x2, 8x5, and 1x10 minutes with matrix sizes of 256x256x205 and voxel sizes of 1.2x1.2x1.23 mm. [F-18]FDOPA scans, also of patients with Parkinson's disease, were acquired on a Siemens ECAT HR+ scanner at the University of Wisconsin-Madison. Data were acquired over 90 minutes and reconstructed with FBP into 18 frames with durations of 2x30 seconds, 3x1, 3x2, 4x5, and 6x10 minutes with matrix sizes of 128x128x63 and voxel dimensions of 2.57x2.57x2.45 mm. In both cases the data were acquired

in accordance with human subjects research protocols approved by the respective local institutional review boards, and in accordance with the declaration of Helsinki.

STEM filtering was implemented with up to 10 iterations using a 4-D asymmetric Gaussian with a FWHM of 4 frames in the frame domain, and a FWHM of 3 mm in each spatial dimension for the [C-11]raclopride HRRT study and 5.2 mm in each spatial dimension for the [F-18]FDOPA HR+ study. All human data were compared to spatial smoothing after reconstruction with a 3-D Gaussian with a FWHM 1.8 mm in each spatial dimension for the [C-11]raclopride data and 3.9 mm in each spatial dimension for the [F-18]FDOPA data.

Parametric images of the human data were created with the same methods used for the simulated data. Bias in the time-series data was assessed by examining the residuals of TACs from relatively large VOIs before and after filtering. Bias in the parametric images was assessed by comparing BP_{ND} or K_i^* values obtained from TACs averaged over large VOIs to BP_{ND} or K_i^* values obtained from parametric images averaged over the same VOIs. VOIs were drawn on PET images temporally summed over the entire course of the study over the right and left caudate nucleus, the right and left putamen, the thalamus, the frontal cortex, and the temporal cortex. Variance in both the time-series images and parametric images was assessed qualitatively (i.e. visually).

6.3 Results

6.3.1 Dual-Isotope Phantom

STEM filtering compares favorably to the spatial filters studied, providing substantial reductions in noise over the initial FBP reconstruction with the ramp filter (0.104 mm⁻¹ frequency cutoff), without introducing a great degree of bias to the TACs or causing a substantial

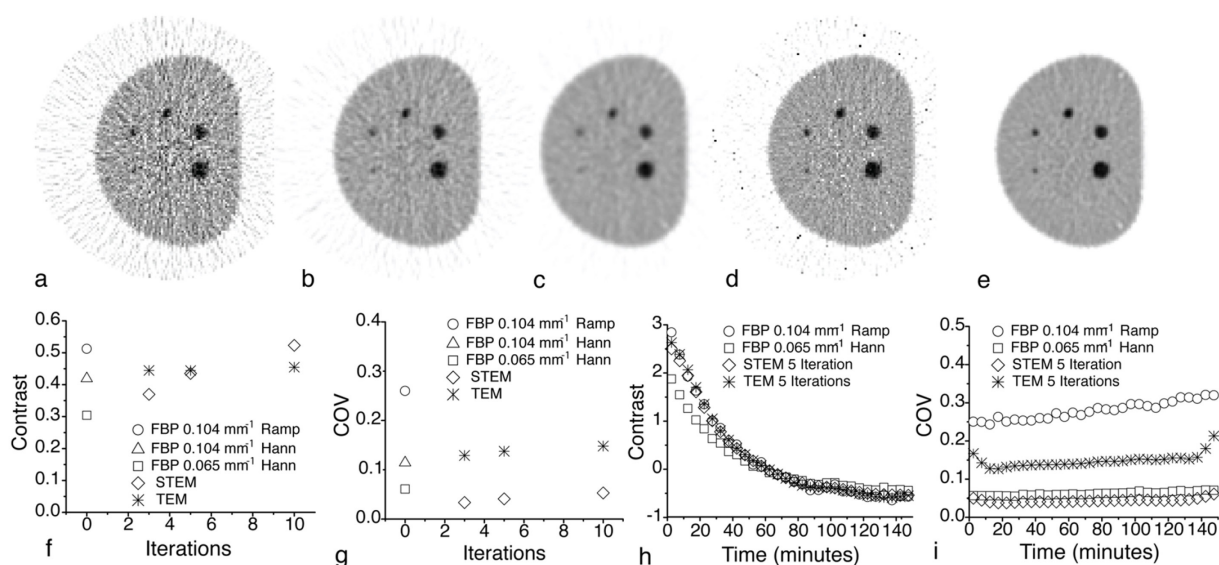


Figure 6.1. The results of the dual-isotope phantom. An illustrative frame ($t = 42.5$ minutes) compares traditional FBP reconstructions (a-c) to TEM (d) and STEM (e) filtering. As more EM iterations are performed there is a progressive recovery of contrast and a corresponding increase in the COV (f & g). The contrast of the 13 mm sphere over the entire time course is largely unaltered by STEM and TEM filtering with 5 iterations (h). The COV of the background is lower following STEM filtering with 5 iterations than in the reconstruction with the 0.065 mm^{-1} Hann window over the entire time course (i). TEM filtering also lowers the COV, but not to the same degree.

loss of spatial resolution. TEM filtering likewise reduces noise and causes no loss in spatial resolution, but it does not improve noise as much as STEM filtering. At an example frame ($t = 42.5$ minutes) STEM filtering gives a greater reduction in noise than the Hann filters but does not degrade the image contrast or resolution (Figure 6.1a-d). TEM filtering also reduces noise without degrading the image, but the reduction in noise is less than that seen with STEM (Figure 6.1e). As more iterations are performed, STEM filtering recovers more contrast, but more noise is introduced into the TEM and STEM filtered images (Figure 6.1f & g). The improvements in image quality that STEM and TEM filtering provide hold true for the entire study (Figure 6.1h & i). After 5 EM iterations, STEM and TEM filtering only appear to bias the earliest frames,

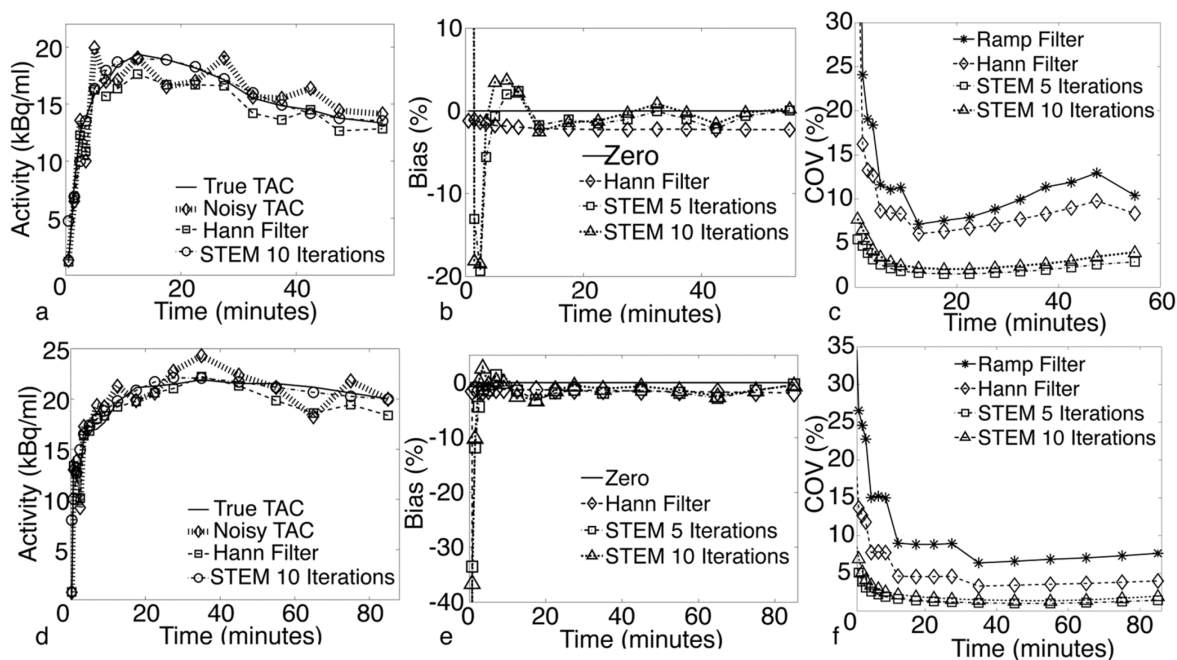


Figure 6.2. Example TACs and the bias-COV tradeoff seen with STEM filtering. An example [C-11]raclopride voxel TAC falls much closer to the underlying truth following STEM filtering (a). STEM filtering biases the earliest frames in the study, but by the later frames the STEM filtered TAC is less biased than the TAC from the Hann reconstruction (b). The COV is lower at all frames following STEM filtering than in either the original reconstruction or in the reconstruction using the Hann filter (c). The [18F]-FDOPA simulations show similar results (d-e).

where the radioactive decay curves have the highest frequency behavior, and this bias is still less than that introduced by the Hann filter with the 0.065 mm^{-1} cutoff at the same frames. STEM and TEM filtering predictably provide less noise suppression in the early and late frames as the filtering kernel is truncated and thus provides less averaging.

6.3.2 [C-11]Raclopride and [F-18]FDOPA simulations

The simulated data show similarly promising results. Following STEM filtering, an example TAC from the [C-11]raclopride simulations falls much closer to the underlying truth than either the original noisy TAC or the TAC from the FBP reconstruction with the Hann filter (Figure 6.2a). With the exception of the earliest frames, STEM filtering introduces minimal bias into the

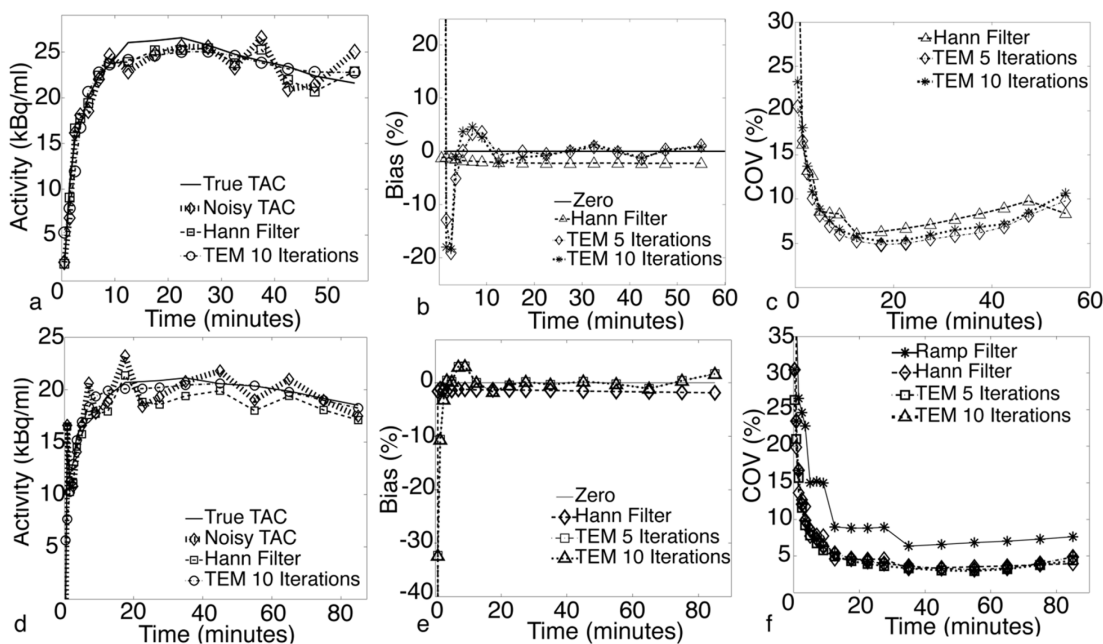


Figure 6.3. Example TACs and the bias-COV tradeoff seen with TEM filtering for both [C-11]raclopride (a-c) and [F-18]FDOPA simulations (d-f). TEM filtering reduces high-frequency noise in the example TACs, but the filtered TACs still generally follows the trend of the noisy TACs (a & d). The bias properties of TEM are similar to those of STEM (b&e). TEM filtering does reduce noise, but not to the same degree as STEM filtering (c & f).

TACs of striatal voxels (Figure 6.2b). The average bias in these voxels is markedly high in the first frame, is 10-20% in magnitude through the second and third frames, and diminishes after that. After approximately the first 10 minutes of the study, the STEM filtered TACs are no more biased, and typically less biased, than the TACs of the data filtered with the Hann window. Because of the short duration of the early frames, the bias of the integral of the TACs is minimal, and is only -0.59% after 5 iterations. More importantly, as shown below, the bias in the early frames has little impact on the quantitative parameters studied in this work (i.e. BP_{ND} and K_i^*). The variance reduction achieved with STEM filtering is substantial, and is greater than that achieved with the Hann filter at all frames (Figure 6.2c). The results from the [F-18]FDOPA simulations are consistent with the [C-11]raclopride results (Figure 6.2d & e).

The simulated data filtered with TEM show similar results. TEM filtering also reduces the high frequency noise in example TACs, to a similar degree as the Hann filter (Figure 6.3a & d). It is important to note, however, that the TEM filtered TACs still follow the general trend of the original noisy TACs, and do not necessarily follow the noise-free TACs. The bias seen with TEM filtering is similar to that seen with STEM filtering (Figure 6.3b & e). The bias at later frames is slightly less with TEM filtering, likely because there is no loss of spatial resolution. TEM filtering does reduce variance in individual frames, but not to the same degree as STEM filtering (Figure 6.3c & f).

6.3.3 Kinetic Analysis of [C-11]Raclopride and [F-18]FDOPA simulations

STEM filtering improves the variance of the simulated [C-11]raclopride and [F-18]FDOPA parametric images for all the analysis methods studied (Table 6.1). STEM filtering also compares favorably with the 0.227 mm^{-1} Hann filter, which predictably introduces a negative bias due to a loss of spatial resolution. After 10 iterations, the parametric [C-11]raclopride images created from the STEM filtered data show little bias and a better average COV than the parametric images created from the Hann filtered data.

The parametric K_i^* images of the simulated [F-18]FDOPA data are largely consistent with the [C-11]raclopride results, but do show more bias, a positive bias in this case, when fewer iterations are used. The Patlak images are themselves slightly positively biased, reflected in the positive average bias in the parametric images created from the FBP reconstructions with the ramp filter, and the bias that is only slightly less than zero in the parametric images created from the Hann filtered data. After 10 iterations, the parametric images created from the STEM filtered

Table 6.1. The average bias and COV of all voxels in the striatum of the parametric images created from the simulated data. After 10 iterations, the parametric images of the STEM filtered data have a lower average COV and less average bias than the parametric images of the data reconstructed using the 0.227 mm^{-1} Hann filter. The average COV is not significantly lower following TEM filtering. In addition, the Logan and Patlak parametric images are more biased following TEM filtering.

	$[^{11}\text{C}]\text{-Raclopride}$				$[^{18}\text{F}]\text{-FDOPA}$	
	RPM2		Reference Logan		Patlak	
	Bias (%)	COV (%)	Bias (%)	COV (%)	Bias (%)	COV (%)
Original Reconstruction (Ramp)	1.37	11.5	-15.8	19.6	3.13	35.5
Hann Filter	-2.62	6.07	-8.15	15.1	-0.15	19.8
STEM 3 Iterations	-1.05	3.04	-0.80	3.73	11.3	4.86
STEM 5 Iterations	-0.96	3.78	-0.68	4.94	5.86	7.09
STEM 10 Iterations	-0.23	4.95	-0.50	6.88	2.20	10.6
TEM 3 Iterations	2.0341	10.9	4.8	18.2	16.96	22.41
TEM 5 Iterations	1.2795	11.2	5.03	21.7	9.66	27.6
TEM 10 Iterations	1.415	11.4	4.4	24.5	4.55	29.49

data do show less bias and an average COV that is half of that seen in the parametric images created from the Hann filtered data.

TEM filtering does not significantly improve the noise in the simulated parametric images (Table 6.1). The Patlak images do show some improvement following TEM filtering, but the improvement is modest. TEM does not significantly bias the RPM2 parametric images, but it does appear to bias the Logan and Patlak parametric images. Based on these results, TEM filtering was not explored further in the human studies.

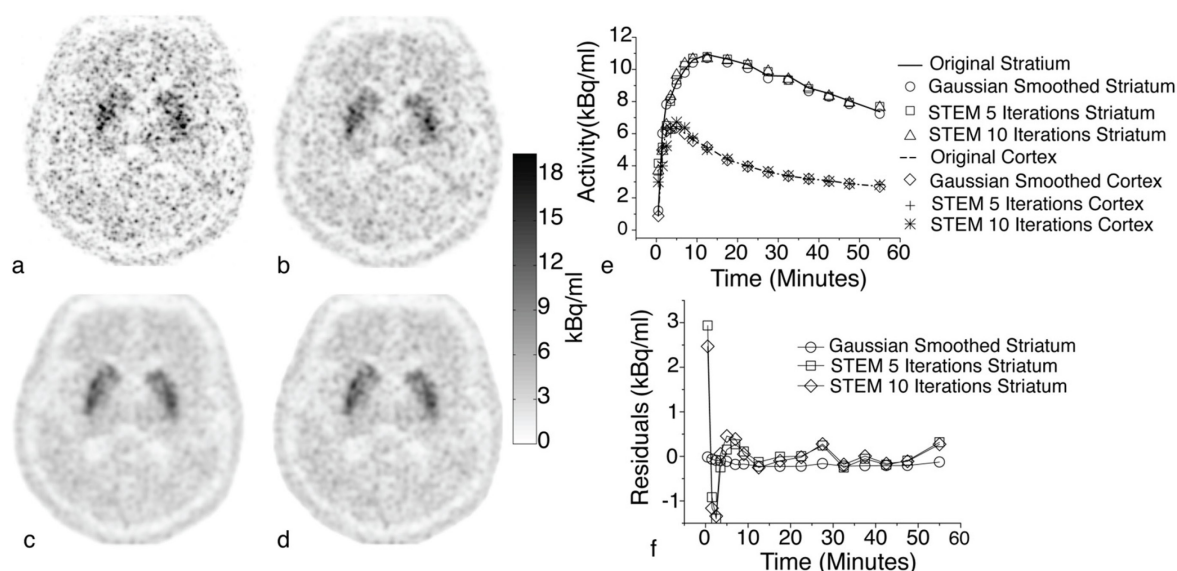


Figure 6.4. A single time frame from the human [C-11]raclopride study evaluated ($t = 32.5$ minutes). The original reconstruction (a) is compared with spatial smoothing using a $1.8 \times 1.8 \times 1.8$ mm³ FWHM Gaussian (b), and STEM filtering after 5 (c) and 10 (d) iterations. Example TACs from large ROIs of the striatum and frontal cortex demonstrate that with the exception of the earliest time points STEM filtering biases the data very little (e & f).

6.3.4 [C-11]Raclopride and [F-18]FDOPA Human Data

The STEM filtered human results are consistent with the simulations. For both the human [C-11]raclopride and [F-18]FDOPA scans studied, after 5 iterations, the STEM filtered images appear to have better spatial resolution than the spatially smoothed image but significantly lower noise (Figure 6.4 & Figure 6.5). The sharpness of the images increases after 10 iterations at the cost of some increased noise. As with the simulated data, there is some bias in early frames following STEM, but as the study progresses the residuals of the STEM filtered data are comparable or better than those of the spatially smoothed data filtering (Figure 6.4f & Figure 6.5f).

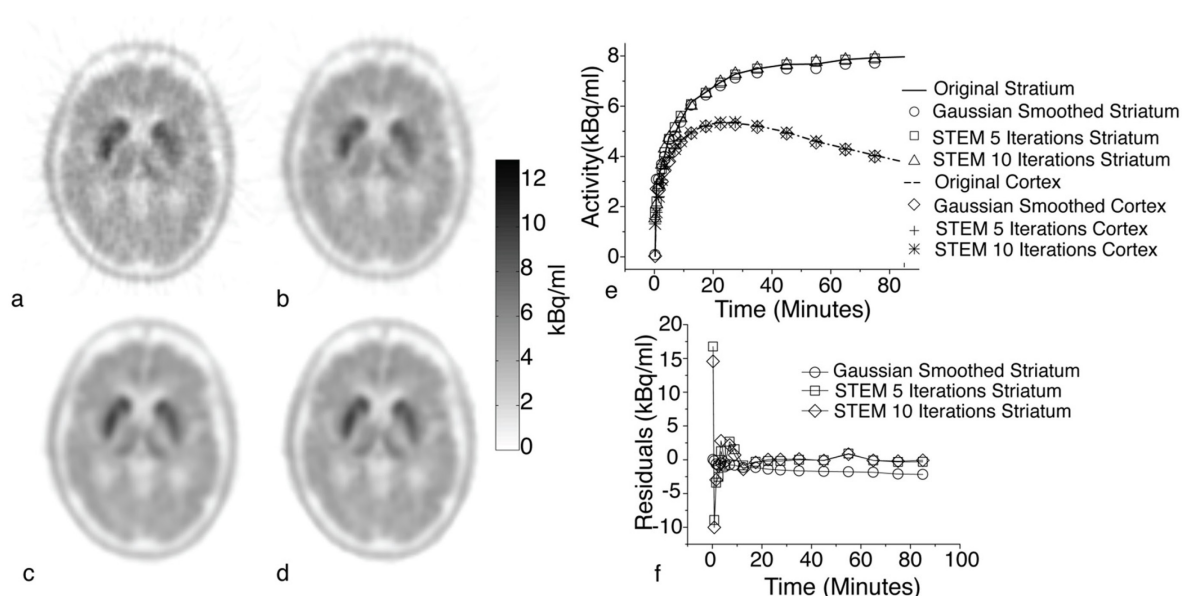


Figure 6.5. A single time frame from the human [F-18]FDOPA study evaluated ($t = 45$ minutes). The original reconstruction (a) is compared with spatial smoothing using a $3.86 \times 3.86 \times 3.86 \text{ mm}^3$ FWHM Gaussian (b), and STEM filtering after 5 (c) and 10 (d) iterations. As with the [C-11]raclopride data, example TACs from large ROIs of the striatum and frontal cortex demonstrate that at most time points STEM filtering biases the data very little (e & f).

The improvement in variance in the parametric images is likewise consistent with the simulated data. For the [C-11]raclopride data, after 5 iterations STEM filtering qualitatively improves the variance in the RPM2 parametric images to a greater degree than spatial smoothing for equivalent or even better spatial resolution (Figure 6.6a-c). Comparing the BP_{ND} values obtained from large VOIs drawn on the parametric RPM2 images to the BP_{ND} values obtained from TACs averaged over the same VOIs demonstrates that smoothing negatively biases the BP_{ND} values, as expected with the loss of spatial resolution, and STEM filtering introduces a slight positive bias to the slope of a linear fit to the data (Figure 6.6d). The bias in the STEM filtered data is primarily due to slightly underestimated BP_{ND} values in lower uptake regions. This bias is diminished as more iterations are performed.

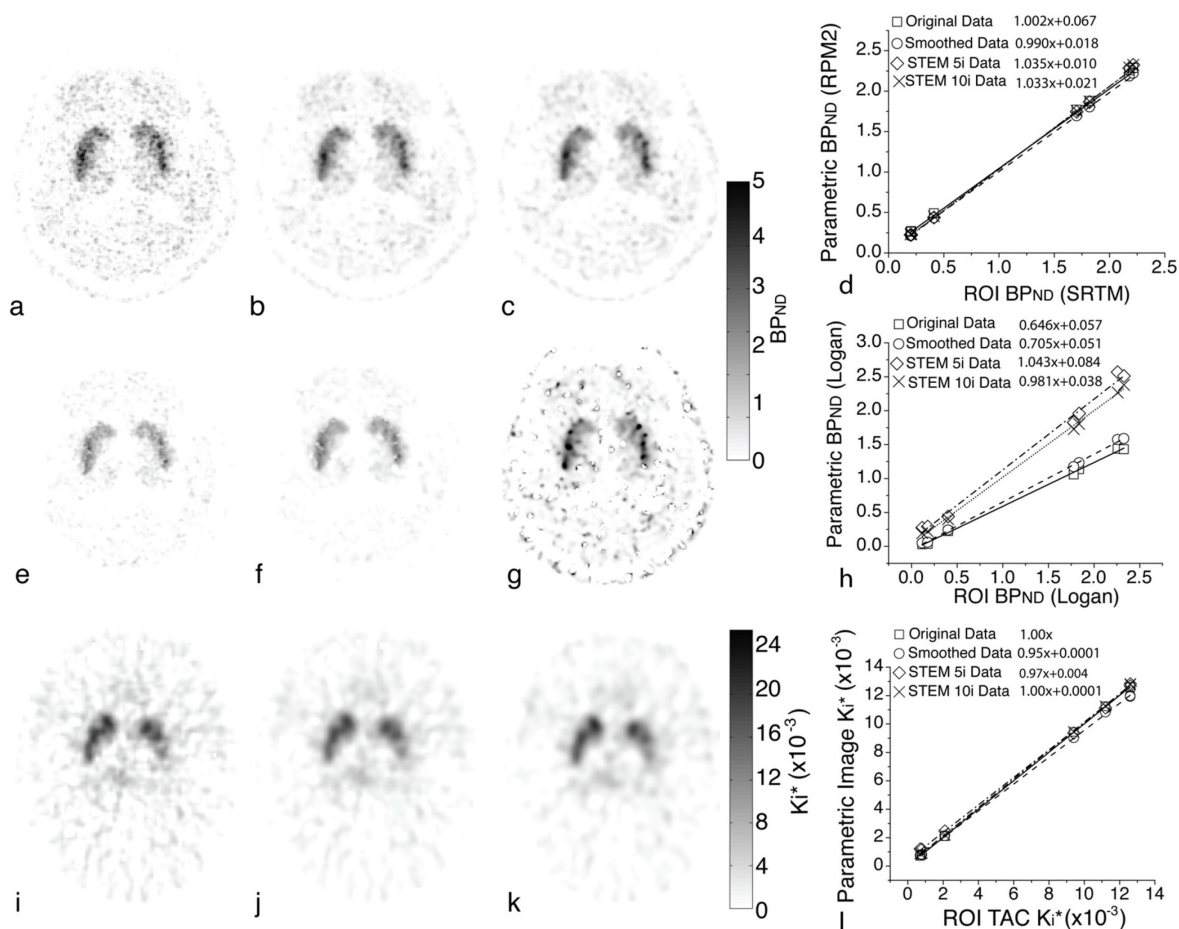


Figure 6.6. RPM2 (a-c) and Logan (e-g) parametric images of the human [C-11]raclopride study, and Patlak parametric images of the human [F-18]FDOPA study (i-k). Parametric created from the original unfiltered reconstruction (a, e, & i) are compared with parametric images created from the spatially smoothed frames (b, f, & j) and the STEM filtered data after 5 iterations (c, g, & k). The BP_{ND} and K_i^{*} values obtained from ROIs in the parametric images are compared with the BP_{ND} and K_i^{*} values obtained from TACs averaged over the same ROIs (d, h, & l). Linear fits to the comparison are shown for the parametric images created from the original data (—), the spatially smoothed data (---), and the data filtered with STEM after 5 (···) and 10 (— · —) iterations.

STEM filtering reduces the noise-dependent bias, and some of the variance, in the Logan parametric images (Figure 6.6e-h). However, a small but noticeable number of voxels have BP_{ND} values that are either very high or negative (Figure 6.6g). This is likely due to the very high noise

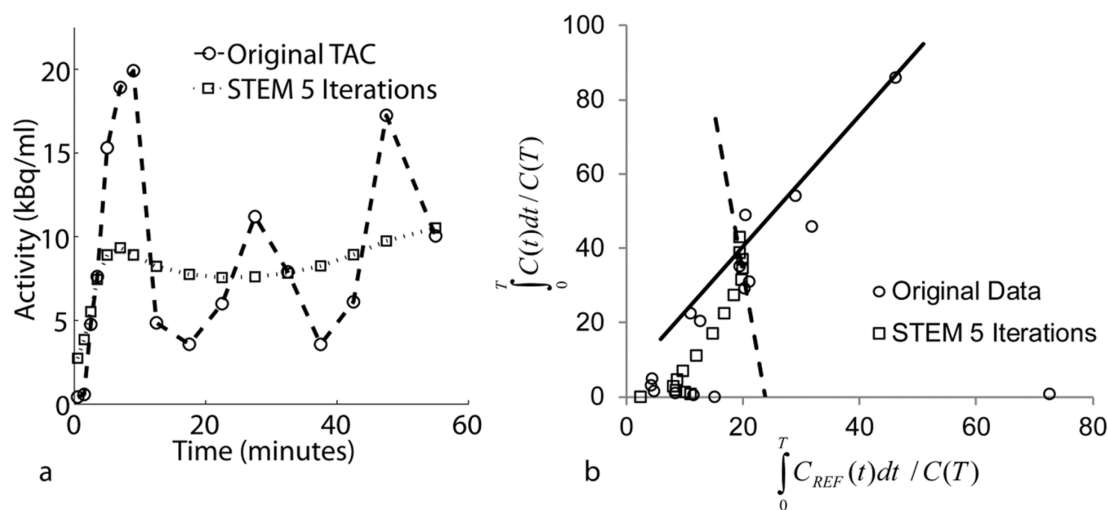


Figure 6.7. The inappropriately high or negative Logan BP_{ND} values following STEM filtering are due to TACs that start to flatten or trend positive at the end of the study because of the very high noise in the HRRT data. STEM filtering exacerbates this behavior (a). When Logan graphical analysis is performed, a linear fit to the noisy original data still yields a line with a reasonable slope. However, the slope of the curve that has been smoothed with STEM filtering is now negative (b).

in the HRRT data, which causes some [C-11]raclopride curves to trend positive at the end of the study. STEM filtering exacerbates this trend and skews the slopes of the Logan plots (Figure 6.7). These values introduce a bias into the average parametric image BP_{ND} values, which is less than the noise-dependent bias seen in images not filtered with STEM (Figure 6.6h).

The reference Patlak parametric images of the [F-18]FDOPA study confirm that STEM filtering can also improve the analysis of tracers that have irreversible binding behavior. After 5 iterations STEM filtering improves the variance in the K_i^* image created with Patlak graphical analysis to a greater degree than spatially smoothing the frames (Figure 6.6i-k). Comparing parametric image K_i^* values averaged over large VOIs to K_i^* values obtained from TACs averaged over the same VOIs shows that the after 5 iterations STEM filtering slightly biases the parametric images, but this bias is eliminated after 10 iterations (Figure 6.6l).

6.4 Discussion

The previous chapter introduced STEM and TEM filtering and the concepts behind their use, and this chapter has attempted to demonstrate that they can provide substantial reductions in noise in both individual time frames and parametric images while introducing little bias.

The dual-isotope phantom data demonstrate that the tradeoff between noise variance and bias is very favorable with STEM filtering. STEM filtering improves noise to a greater degree than traditional filters with less loss of spatial resolution and little loss of temporal accuracy (Figure 6.1). TEM filtering also improves noise, albeit to a lesser degree than STEM, causes absolutely no loss of spatial resolution, and its effects in the time domain appear similar to those of STEM filtering.

The simulated data largely confirm these observations for dynamic PET tracer data. For most frames in the simulated studies, substantial reductions in variance are achieved with minimal bias (Figure 6.2& Figure 6.3). STEM and TEM filtering do bias early frames. This bias is likely due to inadequate temporal sampling, and could be reduced if a finer sampling scheme were used at the cost of increased noise in the shorter frames, as discussed in the previous chapter. Alternatively, the original reconstructions of the first one or more frames could simply be restored after STEM filtering. Importantly, this bias does not appear to have an impact on the quantitative parameters studied here. After STEM filtering with 10 iterations, the variance of the parametric images is low and bias is minimal (Table 6.1). The results from the simulations are largely confirmed by the human data (Figure 6.4-Figure 6.6).

TEM filtering does not significantly improve the variance of the simulated parametric images studied (Table 6.1). This may be due to the fact that kinetic analysis methods provide some

degree of temporal smoothing themselves, as they force the measured data to fit to a predetermined function. Deviations in kinetic parameters are primarily caused by low-frequency noise that subtly alters the shape of TACs. TEM filtering does not reduce enough of this noise to significantly alter the fits. STEM filtering does reduce the variance of kinetic parameters because it enforces a degree of regularization on neighboring TACs. STEM filtering will thus likely be far more useful than TEM filtering for improving quantitative parameters obtained from dynamic PET data.

Interestingly, the parametric images created from the [C-11]raclopride human study with the Logan graphical method show a small but noticeable number of voxels with either very high or very negative values. The simulated data filtered with TEM show similar results. This is likely due to the very high noise in the HRRT data, and the fact that STEM and TEM filtering can exacerbate the effects of low frequency noise by causing TACs to trend either flat or increase at the end of a study (Figure 6.7a). These filtered TACs thus no longer follow reversible binding kinetics. An example Logan plot shows that the noisy original data have both abscissa and ordinate values that can decrease from one point to the next, but a linear fit to the data still gives a reasonable slope. Following STEM filtering, the variability in the abscissa and ordinate values is minimized, but this can create Logan plots with very positive or even negative slopes (Figure 6.7b). The simulated results show that this effect should not be as pronounced in studies acquired on more conventional PET scanners where the noise is not as extreme, so long as STEM and not TEM filtering is used (Table 6.1). It would also likely be less significant for tracers whose activity falls more rapidly at the end of the study. It may therefore be more appropriate to use STEM filtering with another analysis method (e.g. RPM2) for very noisy data, or to use it with Logan graphical analysis for tracers with more pronounced reversible binding behavior.

This chapter has focused primarily on the potential of STEM filtering to improve a number of simplified analysis methods. It also may improve analysis methods that are more sensitive to noise, for example the estimation of individual kinetic parameters in compartmental modeling. The results from the simplified analysis methods, particularly RPM2 which fits the data to a specific model, indicate that STEM filtering may well reduce the variance of individual kinetic rate constants.

STEM filtering is distinct from many 4-D denoising methods in that it makes no explicit assumptions about the dynamic data. In particular, it assumes no kinetic model that all voxels in the image object must follow, and it imposes no explicit limits on the degree to which voxels neighboring each other in space and time are allowed to vary (e.g. a Gibbs prior used in MAP reconstructions or predetermined temporal basis functions), common approaches in 4-D reconstruction (Walledge *et al* 2004, Kadrmas and Gullberg 2001, Meikle *et al* 1998, Nichols *et al* 2002, Li *et al* 2007, Verhaeghe *et al* 2007, Matthews *et al* 1997, Reader *et al* 2006). Rather, because of its use of EM deconvolution, STEM filtering is a data driven approach, and the characteristics of the effective filter will be dependent on the data. The size of the initial 4-D filter does impose an implicit limit on the degree to which neighboring voxels will vary, but this can be offset in part by the number of iterations that are used.

As a post-processing technique, STEM filtering can also improve noise in a number of reconstruction techniques. For example, in this work it has been shown to improve both OSEM and FBP reconstructions. Other iterative reconstructions should thus also be improved, for example MAP and time-of-flight reconstructions.

STEM filtering is very easy to implement and it is relatively fast. In this work it was implemented using MATLAB (version 2011b, the MathWorks, Inc.) on a 64-bit Linux

workstation with two dual core AMD 270 2 GHz processors and 8 GB of RAM. This implementation takes 698 seconds to filter a 128x128x63x18 dynamic dataset up to 10 iterations. These characteristics may make STEM filtering readily applicable to a wide array of dynamic PET applications.

This work has introduced STEM and TEM filtering and generally examined their bias and variance properties in both dynamic time series data and in parametric images. In the future, a more rigorous evaluation of these properties should be undertaken, for example examining the noise-power spectrum and the modulation transfer function in both the space and time domains. It also may prove valuable to evaluate the properties of STEM filtering with a broader variety of time curve behaviors and levels of noise. STEM filtering must also be considered more fully in the context of other 4-D denoising methods, particularly 4-D reconstructions that perform some averaging over the time domain and that do not rely on kinetic models (Kadrmas and Gullberg 2001, Walledge *et al* 2004, Nichols *et al* 2002, Li *et al* 2007, Verhaeghe *et al* 2007, Reader *et al* 2006).

6.5 Conclusions

This chapter has demonstrated that STEM filtering, and to a lesser degree TEM filtering, can provide substantial reductions in variance in both individual time frames and in parametric images created using a number of kinetic analysis techniques, while introducing little bias. STEM filtering makes no assumptions and imposes no explicit limits on the data being filtered, and should therefore provide a simple means of reducing noise for a variety of dynamic PET imaging applications. STEM filtering could be particularly valuable for dynamic PET

applications that suffer from high noise, including parametric image generation, high resolution PET scanning, and tracers that are limited by dosimetry concerns.

References

Brix, G, Zaers, J, Adam, L E, Bellemann, M E, Ostertag, H, Trojan, H, Haberkorn, U, Doll, J, Oberdorfer, F and Lorenz, W J 1997 Performance evaluation of a whole-body PET scanner using the NEMA protocol. National Electrical Manufacturers Association *J. Nucl. Med.* **38** 10 1614-23

Brooks, D J, Salmon, E P, Mathias, C J, Quinn, N, Leenders, K L, Bannister, R, Marsden, C D and Frackowiak, R S 1990 The relationship between locomotor disability, autonomic dysfunction, and the integrity of the striatal dopaminergic system in patients with multiple system atrophy, pure autonomic failure, and Parkinson's disease, studied with PET *Brain* **113** (Pt 5) Pt 5 1539-52

Gunn, R N, Lammertsma, A A, Hume, S P and Cunningham, V J 1997 Parametric imaging of ligand-receptor binding in PET using a simplified reference region model *Neuroimage* **6** 4 279-87

Herzog, H, Tellman, L, Pietrzyk, U, Casey, M E and Kuwert, T 2004 NEMA NU2-2001 Guided Performance Evaluation of Four Siemens ECAT PET Scanners *IEEE Trans Nucl Sci* **51** 5 2662-9

Kadrmas, D J and Gullberg, G T 2001 4D maximum a posteriori reconstruction in dynamic SPECT using a compartmental model-based prior *Phys. Med. Biol.* **46** 5 1553-74

Lammertsma, A A and Hume, S P 1996 Simplified reference tissue model for PET receptor studies *Neuroimage* **4** 3 Pt 1 153-8

Li, Q, Asma, E, Ahn, S and Leahy, R M 2007 A fast fully 4-D incremental gradient reconstruction algorithm for list mode PET data *IEEE Trans. Med. Imaging* **26** 1 58-67

Logan, J 2000 Graphical analysis of PET data applied to reversible and irreversible tracers *Nucl. Med. Biol.* **27** 7 661-70

Logan, J, Fowler, J S, Volkow, N D, Wang, G J, Ding, Y S and Alexoff, D L 1996 Distribution volume ratios without blood sampling from graphical analysis of PET data *J. Cereb. Blood Flow Metab.* **16** 5 834-40

Logan, J, Fowler, J S, Volkow, N D, Wolf, A P, Dewey, S L, Schlyer, D J, MacGregor, R R, Hitzemann, R, Bendriem, B and Gatley, S J 1990 Graphical analysis of reversible radioligand binding from time-activity measurements applied to [N-11C-methyl]-(-)-cocaine PET studies in human subjects *J. Cereb. Blood Flow Metab.* **10** 5 740-7

- Matthews, J, Bailey, D, Price, P and Cunningham, V 1997 The direct calculation of parametric images from dynamic PET data using maximum-likelihood iterative reconstruction *Phys. Med. Biol.* **42** 6 1155-73
- Meikle, S R, Matthews, J C, Cunningham, V J, Bailey, D L, Livieratos, L, Jones, T and Price, P 1998 Parametric image reconstruction using spectral analysis of PET projection data *Phys. Med. Biol.* **43** 3 651-66
- Nichols, T E, Qi, J, Asma, E and Leahy, R M 2002 Spatiotemporal reconstruction of list-mode PET data *IEEE Trans. Med. Imaging* **21** 4 396-404
- Patlak, C S and Blasberg, R G 1985 Graphical evaluation of blood-to-brain transfer constants from multiple-time uptake data. Generalizations *J. Cereb. Blood Flow Metab.* **5** 4 584-90
- Patlak, C S, Blasberg, R G and Fenstermacher, J D 1983 Graphical evaluation of blood-to-brain transfer constants from multiple-time uptake data *J. Cereb. Blood Flow Metab.* **3** 1 1-7
- Reader, A J, Sureau, F C, Comtat, C, Trebossen, R and Buvat, I 2006 Joint estimation of dynamic PET images and temporal basis functions using fully 4D ML-EM *Phys. Med. Biol.* **51** 21 5455-74
- Sossi, V, Holden, J E, de la Fuente-Fernandez, R, Ruth, T J and Stoessl, A J 2003 Effect of dopamine loss and the metabolite 3-O-methyl-[18F]fluoro-dopa on the relation between the 18F-fluorodopa tissue input uptake rate constant K_{occ} and the [18F]fluorodopa plasma input uptake rate constant K_i *J. Cereb. Blood Flow Metab.* **23** 3 301-9
- Verhaeghe, J, Dasseler, Y, Vandenberghe, S, Staelens, S and Lemahieu, I 2007 An investigation of temporal regularization techniques for dynamic PET reconstructions using temporal splines *Med. Phys.* **34** 5 1766-78
- Walledge, R J, Manavaki, R, Honer, M and Reader, A J 2004 Inter-frame filtering for list-mode EM reconstruction in high-resolution 4-D PET *IEEE Trans Nucl Sci* **51** 3 705,706-711
- Wu, Y and Carson, R E 2002 Noise reduction in the simplified reference tissue model for neuroreceptor functional imaging *J. Cereb. Blood Flow Metab.* **22** 12 1440-52
- Zubal, I G, Harrell, C R, Smith, E O, Rattner, Z, Gindi, G and Hoffer, P B 1994 Computerized three-dimensional segmented human anatomy *Med. Phys.* **21** 2 299-302

Chapter 7. Application of HYPR-LR and STEM Filtering to [I-124] PET Imaging

7.1 Introduction

Radioactive iodine isotopes are of great value in nuclear medicine and targeted radionuclide therapy. Radioiodinated agents have a number of advantages: molecules with iodine covalently attached to an aromatic ring are stable *in vivo*, iodine isotopes have a range of half-lives and an appropriate isotope can be selected whose physical half-life matches the physiological half-life of the molecule of interest, iodinated agents can easily be radiolabeled via an exchange reaction (Mangner *et al* 1982, Weichert *et al* 1986), and the field has over 50 years of experience using [I-131] for radiotherapy. Iodine-124 ($t_{1/2} = 4.12$ days) is a positron emitting isotope that could be of great use in a number of positron emission tomography (PET) imaging applications, including imaging antibodies and small molecules with physiological half-lives on the order of hours to days. It's potential as an imaging agent has been recognized for some time, and it continues to be of interest (Greene *et al* 1963, Lippincott *et al* 1964, Bakir *et al* 1992, O'Donoghue *et al* 2011). [I-124] can also be used isosterically to provide high resolution, quantitative PET images of molecules used for targeted radionuclide therapy (TRT) with other iodine isotopes, for example [I-125] and [I-131]. PET images of TRT agents could in turn provide quantitatively accurate, precise, and high resolution normal organ and tumor dosimetry estimates. This has been recognized as a potentially valuable application of [I-124] PET, and dosimetry estimates with [I-124] PET have continued to be of great interest with the introduction of TRT agents like [I-131]-MIBG (Larson *et al* 1992, Sgouros *et al* 2011, Lopci *et al* 2011).

An [I-124] labeled molecule of particular interest at the University of Wisconsin is the phospholipid ether analog [I-124]NM404. NM404 has demonstrated selective uptake and prolonged retention in a large number of preclinical cancer models and human cancers (Rampy *et al* 1995b, Rampy *et al* 1995a, Pinchuk *et al* 2006). In addition to [I-124], NM404 can be labeled with a number of other iodine isotopes, such as [I-125] and [I-131], for targeted radionuclide therapy (TRT), and fluorescent moieties for cellular and *in vivo* optical imaging. High resolution, high quality [I-124]NM404 PET images could be helpful for identifying and evaluating human tumors, and for planning TRT and calculating dosimetry.

However, [I-124] PET imaging is limited in a number of ways. Because of its long half-life, decay scheme including several high energy gamma rays and beta particles, and the potential for high uptake of free iodine by the thyroid, the dose of [I-124] that can be tolerably given to patients may be limited. Additionally, [I-124] only undergoes positron decay 23% of the time. Limited tolerable radiation doses and a relatively low percentage of positron decays will result in high image noise or long scan times. There is also a 604 keV cascade gamma ray that is emitted in 60.5% of the decays, concurrently with roughly half of the positron decays. This gamma results in the detection of incorrect “true” coincidences, which adds a background of incorrect counts to the image, further degrading image quality. A variety of correction algorithms have been proposed to remove this background artifact, but they result in further increased image noise (Lubberink *et al* 2002, Laforest and Liu 2009).

Because of the noise limitations of [I-124] PET imaging, some method of controlling noise will likely be necessary to make [I-124] images in general, and [I-124]NM404 images in particular, diagnostically useful and accurate in clinical applications. Both the Highly constrained back-PRojection-Local Reconstruction (HYPR-LR) and spatio-temporal

expectation-maximization (STEM) filtering methods presented in this thesis could be helpful in this regard.

7.2 Chapter Aims

The aim of this chapter is to evaluate the potential of HYPR-LR and STEM filtering to improve [I-124]NM404 PET imaging. Because HYPR-LR and STEM filtering require 4-dimensional data, applications in which images are acquired at multiple time points are studied. In particular, this chapter aims to:

1. Study the potential of HYPR-LR processing to increase the length of time over which [I-124]-NM404 can be imaged (e.g. several days of scanning) by decreasing noise, particularly at late time points.
2. Study the potential of STEM filtering to improve the quality of human [I-124]-NM404 images in studies involving relatively few (3-4) time points.
3. Study the potential of both HYPR-LR and STEM filtering to reduce the radiopharmaceutical dose and/or imaging time required for [I-124]-NM404, and other tracers labeled with radionuclides that are limited by dosimetry (e.g. [Cu-64]).

7.3 Methods

7.3.1 HYPR-LR for Longitudinal [I-124]NM404 Scanning

To explore the potential of HYPR-LR to increase the length of time over which [I-124]NM404 images with good signal-to-noise ratios (SNR) can be obtained, a pilot study was conducted with two mice with pancreatic cancer xenografts (MiaPaCa) serially imaged with [I-124]NM404 over 14 days. Both mice were injected with approximately 5.55 MBq (150 μ Ci) of [I-124]NM404 and imaged via a hybrid Inveon microPET/CT (Siemens Healthcare, Inc.) 4, 20,

and 30 hours post-injection (p.i.), and approximately every 24 hours after that up to 14 days p.i. All PET scans were acquired to 40 million detected events. PET data were reconstructed with 2-dimensional ordered subset expectation-maximization (2-D OSEM) with 4 iterations and 16 subsets to a matrix size of 128x128x159 with voxel sizes of 0.8x0.8x0.8 mm³. Reconstructed images were registered using affine transformations in Amira (version 4.1.2, Visage Imaging®), and processed with HYPR-LR in MATLAB (version R2008a, The Mathworks™).

In this study, HYPR-LR was implemented using all frames in the studies to form the composite images (HYPR-LR-FC). HYPR-LR-FC was used to study the maximum improvements in noise possible with HYPR-LR in an imaging application with an expected high level of noise. A filtering kernel of 2.4x2.4x2.4 mm³ was used for HYPR-LR processing. Individual time frames were also spatially smoothed with a 2.1x2.1x2.1 mm³ boxcar filtering kernel for comparison.

The SNR and accuracy of the HYPR-LR and spatially smoothed images were assessed in volumes of interest (VOIs). Relatively small spherical VOIs were placed in the tumor (16 voxels) and the liver (24 voxels). The liver was selected as it is a healthy organ that is large and shows homogeneous uptake of [I-124]-NM404. The SNR of the VOIs was assessed by assuming all voxels in them to have uniform uptake and taking the ratio of the standard deviation to the mean:

$$\text{SNR} = \frac{\sigma}{\mu} \quad (7.1)$$

where σ is the standard deviation and μ is the mean. Accuracy was assessed by comparing TACs averaged over the ROIs from the processed images to the TACs from the unprocessed images.

7.3.2 HYPR-LR for Radiation Dose Reduction

Another pilot imaging study was conducted to explore the degree to which radiation dose can be reduced with HYPR-LR. In this case, PET imaging with [Cu-64] was evaluated in addition to [I-124]. Copper-64 is another relatively long lived ($t_{1/2}=12.7$ hours) isotope with a relatively poor percentage of positron decays (18%), whose use might also be limited by radiation dosimetry and image noise (ICRP 1987, Smith 2004). Four healthy mice were scanned for 1 hour on the Inveon microPET/CT (Siemens Healthcare, Inc.). Acquisition of PET data was begun immediately following injection of either 10.4 or 2.74 MBq of [Cu-64]CuCl₂, or 10.7 or 3.90 MBq (289 or 105 μ Ci) of [I-124]NM404. All PET data were histogrammed into 15 frames: 1x1, 1x3, 1x7, 1x15, 1x20, 1x30, 1x45, 1x120, 2x240, 1x480, and 4x600 seconds in duration. PET images were reconstructed using 2-D OSEM with 4 iterations and 16 subsets to a matrix size of 128x128x159 with voxel sizes of 0.8x0.8x0.8 mm³.

HYPR-LR was applied using the multiple composite implementation (HYPR-LR-MC) with a t_{uptake} of frame 3, an α of 2 (5 frames in the sliding composite), and a t_{max} of frame 11. These parameters were empirically determined from the data. HYPR-LR-MC was used because of the relatively fast kinetics, and hence variable time frame images, in the first hour following the injection of these tracers. A 2.4x2.4x2.4 mm³ Gaussian filtering kernel was used for HYPR-LR-MC processing.

Image SNR and accuracy were evaluated in essentially the same way as described above. SNR was measured in the liver for both [Cu-64]CuCl₂ and [I-124]NM404 using Equation 7.1, and TACs averaged over ROIs in the liver, kidneys, and heart were studied. Again, the liver was

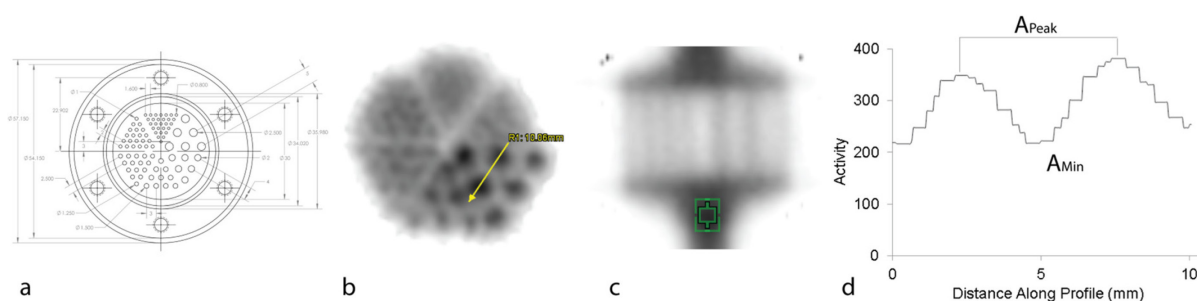


Figure 7.1. The Derenzo resolution phantom used to evaluate STEM filtering of [I-124] data (a). The MTFs of the different reconstructions before and after STEM filtering were measured by comparing the peak and minimum values from a profile through each group of rods (b) to the maximum activity, measured in a small uniform background ROI (c). An example profile is through the 5 mm rods is shown (d).

chosen to measure SNR as it is a relatively large organ with homogeneous uptake of both [I-124]-NM404 and [Cu-64]CuCl₂.

7.3.3 STEM Filtering for Improved Image Quality, Reduced Scan Durations, and Reduced Radiation Dose

The potential of STEM filtering to improve image quality, reduce scan durations, and/or reduce radiation dose was evaluated in a phantom study and in human [I-124]NM404 scans. Current human investigations with [I-124]NM404 consist of 3 scans acquired over the course of 3 days. These data were filtered with STEM as preliminary investigations showed that STEM has greater potential than HYPR-LR to improve datasets with such a small number of frames. STEM filtering such datasets is thus the focus in this section.

7.3.3.1 STEM Filtering [I-124] Phantom Study

STEM filtering was first evaluated with a Derenzo resolution phantom specially designed for a microPET scanner. An acrylic Derenzo phantom with fillable rods 5, 4, 3, 2, and 1.6 mm in diameter, separated from each other by the same distances was utilized for this study. (Figure

7.1a). The phantom was filled with 11.9 MBq of [I-124] and scanned on the Inveon microPET scanner (Siemens Healthcare, Inc.) 1, 24, 48, and 144 hours after it was filled. All PET scans were acquired to 1 billion counts. A single microCT scan of the phantom was acquired, registered to each of the PET scans, and used for attenuation and scatter correction of each PET image. Acquired PET data were histogrammed into sinograms using either all or a sixteenth of the detected coincidences, and reconstructed with either FBP with a ramp filter (at the Nyquist frequency), or 3-dimensional OSEM with *maximum a posteriori* (3-D OSEM/MAP) with 2 OSEM iterations with 16 subsets, and 18 MAP iterations with a β smoothing parameter of 0.1. All images were reconstructed to a matrix size of 128x128x159 with voxel sizes of either 0.4x0.4x0.8 mm³ (FBP) or 0.43x0.43x0.8 mm³ (3D OSEM/MAP).

STEM filtering was applied to all of the reconstructions up to 10 iterations using a Gaussian filtering kernel with a FWHM of 0.8 mm in each spatial dimension, and a FWHM of 1.5 frames in the image frame domain. The FBP reconstructions were also smoothed with a 0.8x0.8x0.8 mm³ Gaussian to serve as an additional comparison for STEM filtering.

The resolution of the images reconstructed with FBP, 3-D OSEM/MAP, FBP followed by STEM filtering, and FBP followed by spatial smoothing was assessed by measuring the modulation transfer function (MTF). The MTF was measured using the images reconstructed with all of the acquired data to give the lowest possible noise. The power of the MTF at the primary spatial frequencies represented by each set of rods was measured as:

$$\frac{A_{\text{Peak}} - A_{\text{Min}}}{A_{\text{Max}} - A_{\text{Background}}} \quad (7.2)$$

where A_{Peak} is the peak activity for a given set of rods, averaged over the maxima for a profile through the rods, A_{Min} is the minimum activity, also averaged over the profile, A_{Max} is the true

maximum activity averaged over a small ROI with little to no volume averaging effects, and $A_{\text{Background}}$ is the background activity (assumed to be zero) (Figure 7.1b & c). The primary spatial frequency represented by each set of rods was taken as the number of rods per mm.

Noise in the images was assessed with the noise power spectrum (NPS). The NPS was measured in a square region of uniform activity in the images reconstructed with a sixteenth of the data using FBP, FBP with STEM filtering, 3-D OSEM/MAP, and 3-D OSEM/MAP with STEM filtering. The noise was found from the background region by subtracting its mean. The NPS was calculated as:

$$S_{j,k} = \frac{1}{M^2} \left| \sum_{x=0}^{M-1} \sum_{y=0}^{M-1} n_{x,y} \exp(-2\pi i \frac{xj}{M}) \cdot \exp(-2\pi i \frac{yk}{N}) \right|^2 \quad (7.3)$$

where $S_{j,k}$ is the 2-dimensional NPS of the noise, $n_{x,y}$, with M elements in both the x and y-dimensions. The 2-dimensional NPS was integrated over 180 projections through the origin to give a 1-dimensional representation of the NPS.

7.3.3.2 STEM Filtering of [I-124]NM404 Human Brain Tumor Studies

The performance of STEM filtering was also evaluated in three human brain tumor [I-124]NM404 studies. All patients studied had either newly diagnosed (n=1) or recurrent (n=2) gliomas. Patients were injected with approximately 185 MBq of [I-124]NM404 and imaged at 6, 24, and 48 hours post-injection on a Discovery VCT PET/CT scanner (GE Healthcare). Each PET scan of the brain was acquired for 90 minutes. Images were reconstructed using either 30 minutes or all 90 minutes of acquired data with 2-D OSEM with 2 iterations and 28 subsets and a $2.57 \times 2.57 \text{ mm}^2$ FWHM Gaussian filter applied after reconstructions. Images were reconstructed to voxel sizes of $2.35 \times 2.35 \times 3.27 \text{ mm}^3$.

STEM filtering was applied up to 10 iterations using a Gaussian filter with a FWHM of 4.7 mm in each spatial dimension and 1.5 frames in the frame dimension. STEM filtering was applied to the reconstructions using only 30 minutes of acquired data. STEM filtering was compared to spatial smoothing with an additional 4.7x4.7x4.7 mm³ FWHM Gaussian applied after reconstruction.

Noise and bias of the human scans were assessed by measuring the bias in the contrast between tumor and background after filtering, by measuring the coefficient of variation (COV) of the background, and by evaluating tumor TACs. Contrast was measured between a tumor ROI and a background ROI drawn in the contralateral hemisphere of the brain:

$$\text{Contrast (\%)} = \frac{\mu_{\text{Tumor}} - \mu_{\text{Background}}}{\mu_{\text{Background}}} \cdot 100 \quad (7.4)$$

where μ_{Tumor} is the mean of the tumor ROI and $\mu_{\text{Background}}$ is the mean of the background ROI.

The COV was measured in the background ROI:

$$\text{COV (\%)} = \frac{\mu_{\text{Background}}}{\sigma_{\text{Background}}} \cdot 100 \quad (7.5)$$

where σ_{Tumor} is the standard deviation of the background ROI. The same ROIs were used for the unfiltered and filtered images.

7.4 Results

7.4.1. HYPR-LR for Longitudinal [I-124]NM404 Scanning

In the 2 mice scanned with [I-124]NM404 over the course of 14 days, HYPR-LR processing significantly improves the noise of the PET images while maintaining the fidelity of the TACs studied (Figure 7.2). In the liver ROI, at the first frame (t = 4 hours) HYPR-LR improves the

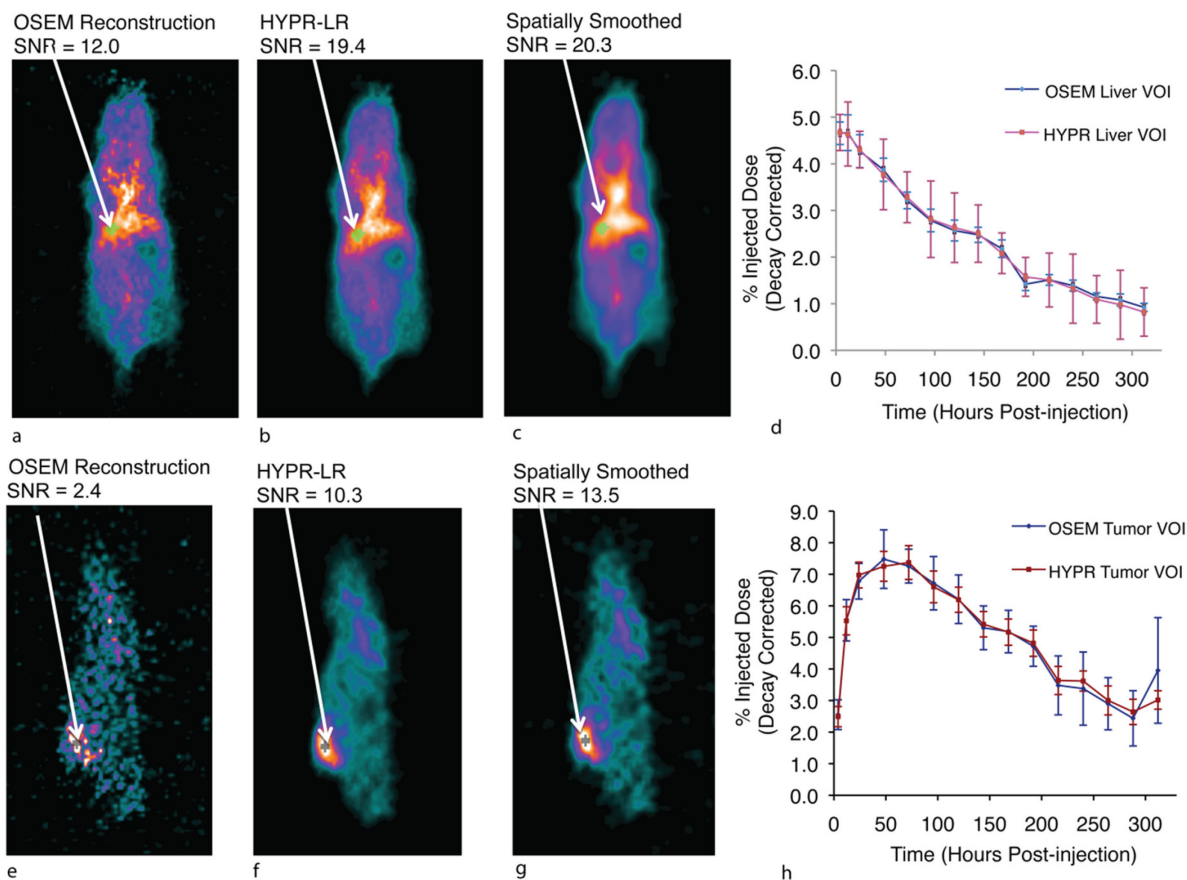


Figure 7.2. Example time frame images and TACs from the extended imaging time-point [I-124]NM404 study. Images from the first frame demonstrate that HYPR-LR increases the SNR of a small liver ROI to nearly the same degree as spatial smoothing, but the image is not as blurred (a-c). The TAC of the ROI is essentially unchanged, and the standard deviation at each time point is reduced by HYPR-LR processing (d). Example images from the last time frame and a tumor TAC show similar improvements (e-h).

SNR by 1.6 fold (from 12 to 19), similar to the SNR of the spatially smoothed image (20.3). In the tumor ROI at the final frame ($t = 240$ hours), HYPR-LR improves the SNR by over 4 fold (from 2.4 to 10.3), also similar to the SNR of the spatially smoothed image (20.3).

7.4.2 HYPR-LR for Radiation Dose Reduction

Following HYPR-LR processing, the PET images of the animals injected with less radioactivity have similar noise properties to the images of the animals injected with a full

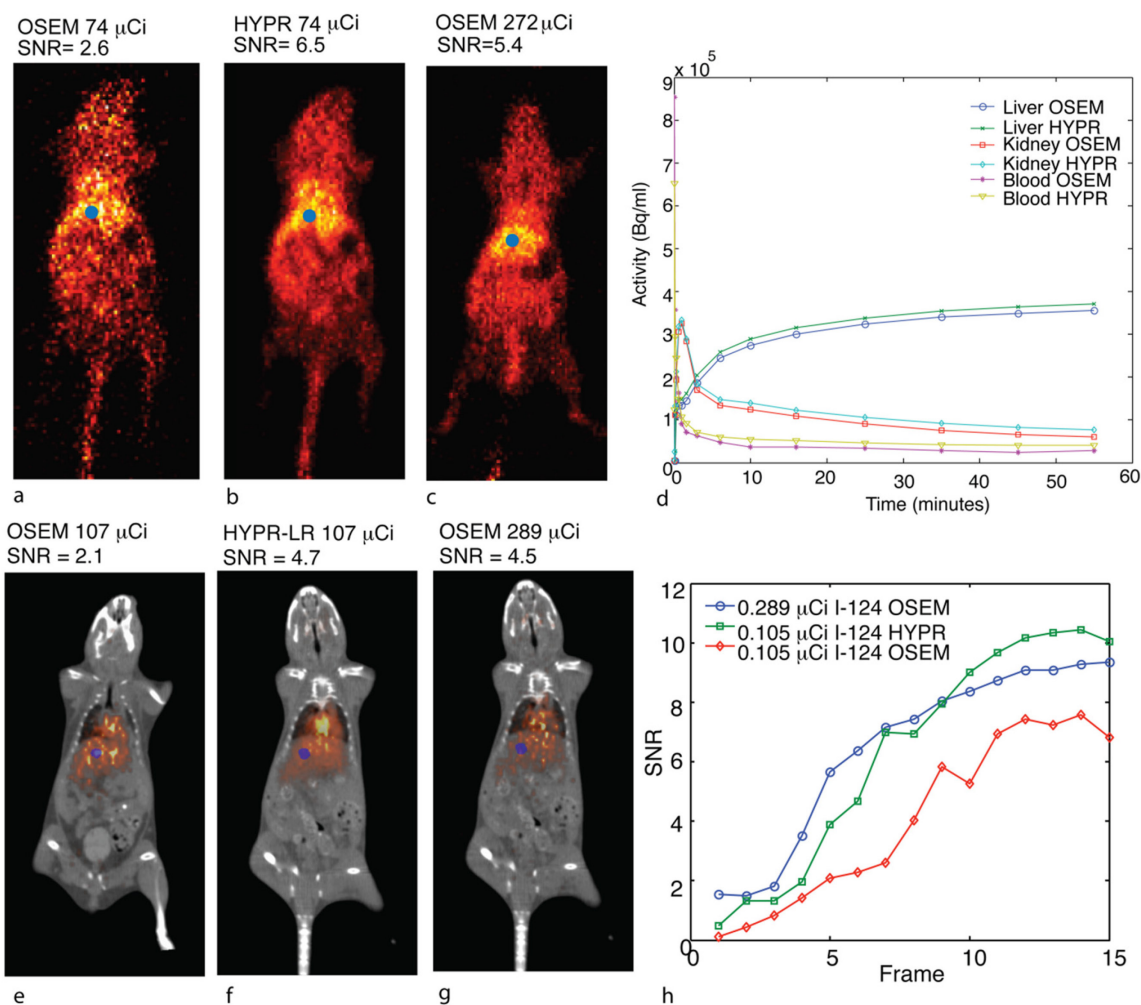


Figure 7.3. Results from the radiopharmaceutical dose reduction study. Example images from the $[Cu-64]CuCl_2$ studies show that following HYPR-LR processing the image from the animal injected with a third of the radioactivity has better SNR than the animal injected with the full dose (a-c). The accuracy of the TACs studied is largely preserved with HYPR-LR processing with the exception of the sharp peaks in the blood and kidney (d, note that the HYPR-LR TACs have been offset to improve their visualization, hence early time points that are not offset are erroneous). Images from the $[I-124]NM404$ show similar results to the $[Cu-64]CuCl_2$ studies (e-g). The improvements in SNR seen with HYPR-LR processing are consistent over the course of the $[I-124]NM404$ study (h).

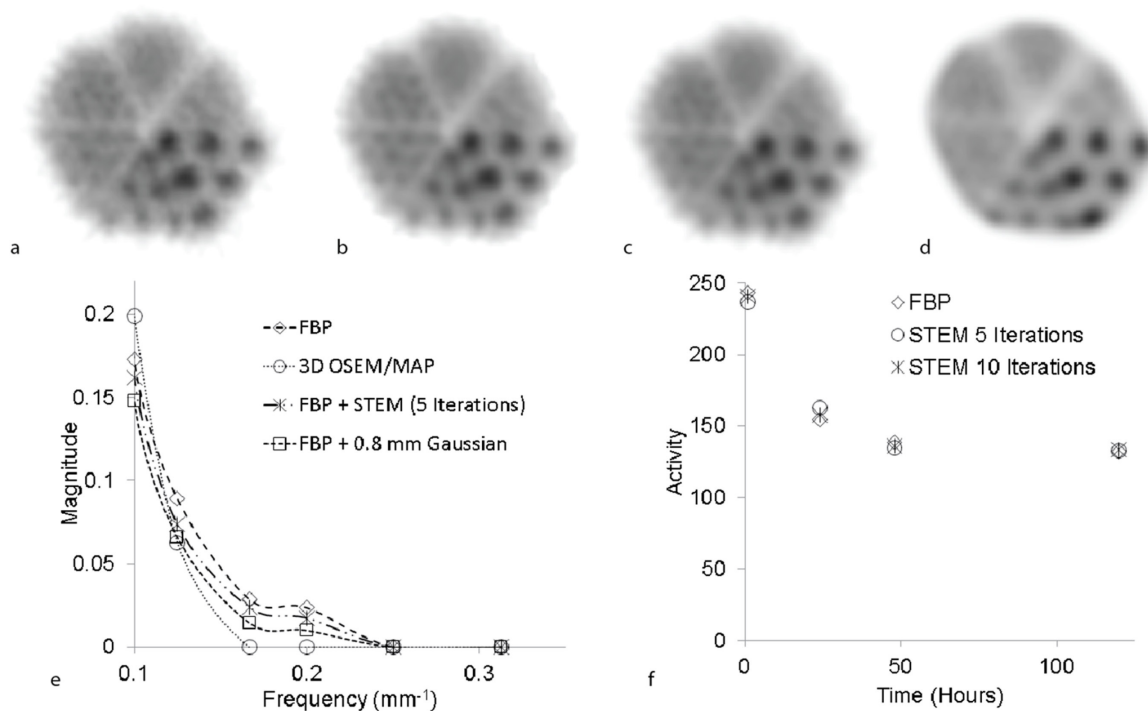


Figure 7.4. Evaluation of spatial resolution and the temporal accuracy following STEM filtering. The FBP reconstruction (a) is compared to the FBP reconstruction filtered with STEM after 5 iterations (b), the FBP reconstruction followed by spatial smoothing with a $0.8 \times 0.8 \times 0.8$ mm³ Gaussian (c), and the 3-D OSEM/MAP reconstruction with $\beta = 0.1$ (d). The MTF of these 4 images at the first frame shows that the resolution of the FBP reconstruction is only slightly degraded by STEM filtering, and more degraded by spatial smoothing (e). The 3-D OSEM/MAP reconstruction performs comparably to FBP at the lower resolutions, but the higher frequencies are lost. STEM filtering slightly biases the TAC after 5 iterations, and this bias is reduced with 10 iterations (f).

radiopharmaceutical dose. This can be seen in the SNR of small liver ROIs from example frames for both tracers (Figure 7.3), and over the course of the [I-124]NM404 study (Figure 7.3b). The TACs of ROIs in the heart, kidneys, and liver of the [Cu-64]CuCl₂ study show that HYPR-LR processing introduces little bias, though some bias can be seen in the peaks of the heart and kidney TACs (Figure 7.3h).

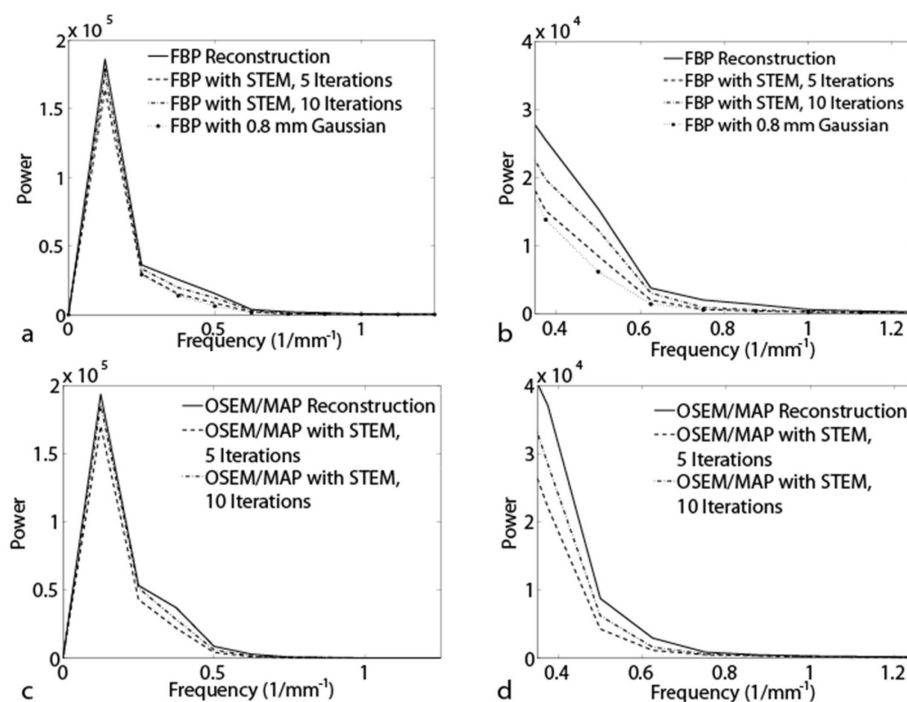


Figure 7.5. The NPS of the FBP (a & b) and OSEM/MAP (c & d) reconstructions before and after STEM filtering with 5 and 10 iterations. The overall NPS (a & c), and the NPS at higher frequencies (b & d) are both shown. STEM filtering reduces the noise in both FBP and OSEM/MAP reconstructions at a broad range of frequencies. More noise reduction is achieved with 5 STEM iterations than with 10. Spatially smoothing the FBP reconstruction gives a similar NPS as STEM filtering with 5 iterations (a & b).

7.4.3 STEM Filtering [I-124] Phantom Results

STEM filtering only slightly degrades the resolution of the Derenzo phantom, as measured by the MTF, while noticeably reducing noise, as measured by the NPS (Figure 7.4 & Figure 7.5). This allows for better visualization of the rods in the Derenzo phantom (Figure 7.4a & b). STEM filtering also does not significantly bias the temporal behavior (i.e. [I-124] decay) of the phantom (Figure 7.4f). STEM filtering degrades the resolution of the phantom less than spatial smoothing while giving a similar degree of noise reduction (Figure 7.4 e & Figure 7.5b).

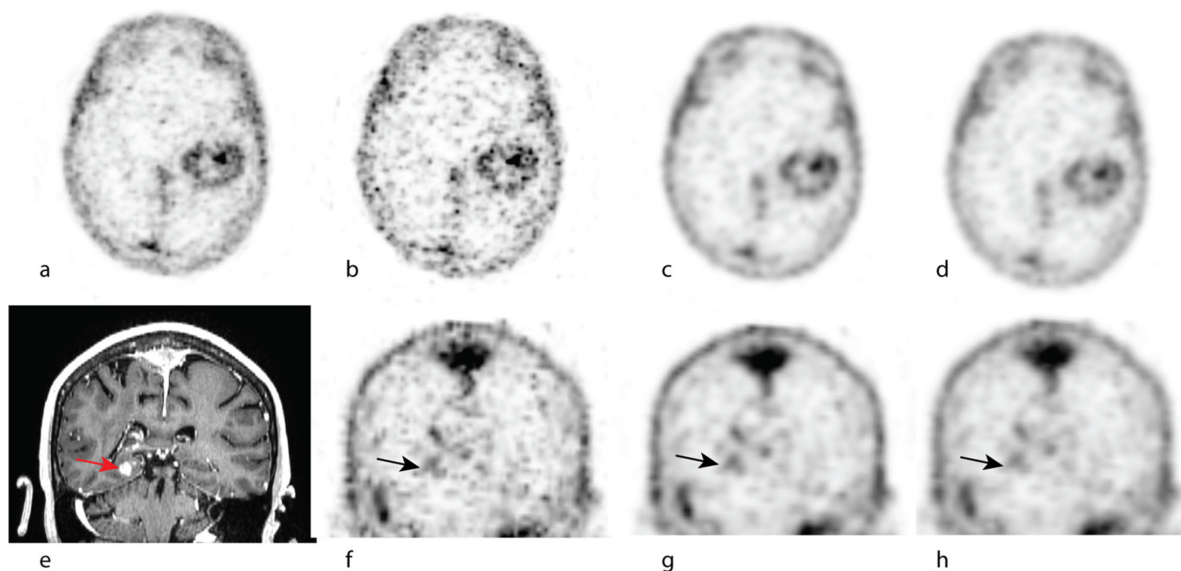


Figure 7.6. Example human images of [I-124]NM404 from 2 brain tumor patients. For the first patient (a-d), the OSEM reconstruction using 90 minutes of data (a) is compared to the same reconstruction using 30 minutes of data (b), the 30 minute reconstruction followed by 5 iterations of STEM (c), and the 30 minute reconstruction following smoothing with a $4.7 \times 4.7 \times 4.7 \text{ mm}^3$ Gaussian (d). For the second patient (e-f), a T1 weighted MRI acquired after the administration of gadolinium (e) shows an enhancing region of tumor (arrow). The OSEM reconstruction of 30 minutes of acquired PET data is also shown (f) and compared to STEM filtering with 5 iterations (g) and smoothing with a $4.7 \times 4.7 \times 4.7 \text{ mm}^3$ Gaussian.

FBP and 3-D OSEM/MAP reconstructions were also compared before and after STEM filtering (Figure 7.4 & Figure 7.5). The FBP reconstruction has better resolution than the 3-D OSEM/MAP reconstruction at higher spatial frequencies, but the 3-D OSEM/MAP reconstruction has less high frequency noise. Following STEM filtering, the FBP reconstruction still has better resolution than the OSEM/MAP reconstruction, and the noise power spectra of the images are similar. STEM filtering can also reduce noise in the MAP reconstructions (Figure 7.5c & d).

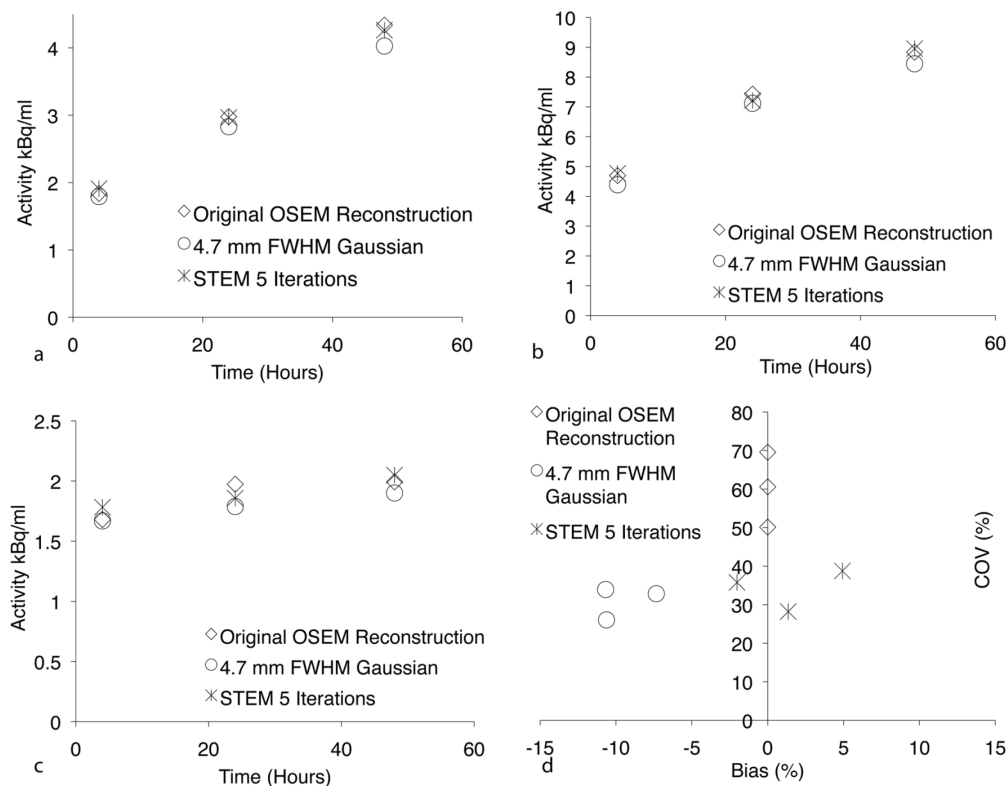


Figure 7.7. Tumor TACs from the 3 patients studied (a-c) and bias and COV from the last frame ($t = 48$ hours) of each study (d). The TACs from the original reconstruction are compared with the TACs from the spatially smoothed images and the images filtered with 5 iterations of STEM. Bias in the tumor activity at the last frame is compared to the COV of a contralateral background region (d).

7.4.4 STEM Filtering of [I-124]NM404 Human Brain Tumor Studies

STEM filtering reduces noise in the human brain tumor studies while introducing little bias into the data. In example images from two of the patients studied, STEM filtering the shorter (30 minute) acquisitions reduces the high frequency noise without blurring the tumor activity (Figure 7.6). The second set of example images in particular (Figure 7.6e-h) demonstrates how this may improve tumor visualization. The contrast is not degraded in a small region of recurrent tumor in the right medial temporal lobe (arrow), but high frequency noise is reduced.

The tumor TACs are slightly biased by STEM filtering, but at nearly all the frames studied this bias is less than what is seen with spatial smoothing (Figure 7.7a-c). The bias of the tumor activity and COV of the background at the final frame confirm this, showing that STEM filtering introduces less bias for comparable reductions in noise relative to spatial smoothing (Figure 7.7d).

7.5 Discussion

7.5.1 HYPR-LR Processing of [I-124]NM404 Studies

The pilot studies in this work show that noise improvements from HYPR-LR processing could be used to extend the time over which [I-124]NM404 (or any other molecule labeled with [I-124]) is imaged, and could be used to reduce radiopharmaceutical dose of tracers labeled with [I-124] and other radionuclides that are limited by radiation dosimetry.

HYPR-LR processing improves the SNR of the PET images from the mice scanned over 14 days with [I-124]NM404 up to 4 fold, dramatically improving the quality of images acquired several days after the injection of the radiotracer (Figure 7.2). Time points occurring a few half-lives after the injection of radiotracer could contain important information, and improved SNR at these time points might allow this information to be observed and measured with greater accuracy and confidence. In addition, a noise improvement of 4-fold essentially makes up for the poor positron fraction of [I-124] decays.

The improvements in noise seen with HYPR-LR processing in the radiopharmaceutical dose reduction study are likewise significant. The results demonstrate that images processed with HYPR-LR have similar SNRs to unprocessed images acquired with 3 or more times the injected radiopharmaceutical dose (Figure 7.3). These improvements could be tremendously valuable for

radionuclides whose use will likely be limited by radiation dosimetry, making their clinical use more feasible and safe for human subjects.

7.5.2 STEM Filtering of [I-124]NM404 Studies

STEM filtering has potential to improve the quality of datasets consisting of multiple images acquired over the course of hours or days. These improvements would be particularly valuable for tracers labeled with [I-124]. Such tracers, for example antibodies or in this case the small molecule NM404, can provide insight into biological processes that occur over hours or days, but are limited by the radiation dosimetry of [I-124]. As such, image quality with [I-124] tracers can be poor, or scanning times at each time point must be long. STEM filtering could thus provide better image quality with less radiation dose or shorter acquisitions at each time point.

STEM filtering has been evaluated here using a Derenzo resolution phantom and 3 [I-124]NM404 studies in humans with gliomas. The Derenzo resolution phantom demonstrates that STEM filtering can reduce noise at individual frames, measured by the NPS (Figure 7.5), without significantly degrading spatial resolution, measured by the MTF (Figure 7.4e), or the temporal signal (Figure 7.4f). The rods in the phantom can thus be better visualized, particularly at higher spatial frequencies (Figure 7.4a-d). STEM filtering gives slightly better spatial resolution than simple spatial smoothing (Figure 7.4e) and a similar NPS (Figure 7.5b). The STEM filtered FBP reconstruction also compares favorably to the OSEM/MAP reconstruction. Following STEM filtering, the FBP reconstruction has better spatial resolution at high spatial frequencies than the OSEM/MAP reconstruction (Figure 7.4e) for a similar level of noise (Figure 7.5). The noise in the OSEM/MAP reconstruction is also reduced with STEM filtering (Figure 7.5c & d), though the spatial resolution of the resulting images is still worse than it is in the FBP reconstruction.

The human studies also show an improvement in noise with little loss of spatial or temporal resolution following STEM filtering. Example PET images from two patients show that STEM filtering might allow for better visualization of tumors in [I-124]NM404 studies, as noise is well suppressed and there is little loss of signal in the lesions (Figure 7.6). This may be particularly valuable for small lesions that could be easily obscured by noise or overly blurred by simple spatial smoothing (Figure 7.6e-h). The minimal bias and improvements in noise seen with STEM filtering are confirmed by the tumor TACs (Figure 7.7a-c) and the tradeoff between bias and COV in the last frame from each study (t=48 hours) (Figure 7.7d).

The human images do show that while STEM filtering suppresses high frequency spatial noise quite well, low frequency spatial noise is largely preserved because it is recovered along with the low frequency signal. Such low frequency spatial noise may interfere with the detection of small lesions. Small lesions may therefore be difficult to distinguish from noise at low spatial frequencies regardless of whether STEM filtering is performed. This could be explored more fully with a detection study using a machine or human observer. An observer may incorrectly identify noise as a small lesion, or dismiss actual small lesions as noise. Such a study will help better define the true potential of STEM filtering for improving the actual diagnostic quality of [I-124]NM404 images.

STEM filtering should also be compared to other denoising methods in the context of [I-124] imaging. In this work it has been compared to spatial smoothing and to an OSEM/MAP reconstruction using a relatively conservative β smoothing parameter of 0.1. STEM filtering performed relatively well compared to these established methods of reducing noise. However, STEM filtering was not compared to wavelet denoising or other more sophisticated methods.

STEM filtering has the advantage of being less complicated to implement than wavelet denoising, and because it uses EM deconvolution no explicit limits are put on the data.

7.5.3 Limitations of HYPR-LR Processing and STEM Filtering for Improving [I-124] Studies

Both HYPR-LR and STEM filtering require a dynamic component to the data. Many other noise reduction methods, for example smoothing, MAP reconstruction, and wavelet denoising, do not, and can be used with individual images. HYPR-LR processing and STEM filtering will thus be limited to applications in which multiple acquisitions are involved. However, many [I-124] PET imaging applications may involve acquiring data at multiple time points, for example to calculate radiation dosimetry for TRT with an [I-131] labeled agent.

It is also important to note that HYPR-LR processing and STEM filtering are post-processing methods, and as such will be limited by the accuracy of the initial reconstructions. This is an important consideration in applications with very low counts, including extreme instances of the examples studied here (e.g. imaging a radionuclide after several physical half-lives have passed). PET images will be limited by inaccuracies in correction methods (e.g. random counts and scatter) when very low activities are scanned (Watson *et al* 1997, Cheng *et al* 2007). HYPR-LR processing and STEM filtering cannot reduce the errors in the images themselves. However, the denoising algorithms explored in this work could be used to devise better correction methods (Cheng *et al* 2011).

7.6 Conclusions

This chapter has presented HYPR-LR processing and STEM filtering as denoising methods that could be used to improve the PET imaging of [I-124] in a number of ways. These methods

could reduce noise in sets of images that have been acquired over several days, in images acquired with less injected radiopharmaceutical dose, and in images acquired for less time to improve patient comfort, compliance, and clinical practicality. Improvements in noise could enable more accurate kinetic analysis, demonstrated previously with shorter-lived isotopes (Floberg *et al* 2012), and enable better clinical diagnosis, though this remains to be demonstrated. To my knowledge, this is the first demonstration of using a 4-dimensional process to reduce noise in dynamic PET data acquired over the course of days in separate scanning sessions. Such an approach could be very useful for imaging other molecules with slow kinetics, particularly antibodies, and could make the clinical use of such molecules safer and more feasible.

References

- Copper, radiation dose to patients from radiopharmaceuticals 1987 *Ann. ICRP* **18** 135-6
- Bakir, M A, Eccles, S, Babich, J W, Aftab, N, Styles, J, Dean, C J, Lambrecht, R M and Ott, R J 1992 c-erbB2 protein overexpression in breast cancer as a target for PET using iodine-124-labeled monoclonal antibodies *J. Nucl. Med.* **33** 12 2154-60
- Cheng, J C, Laforest, R and O'Sullivan, J A 2011 A scatter and randoms weighted (SRW) iterative PET reconstruction *Med. Phys.* **38** 6 3186-92
- Cheng, J C, Rahmim, A, Blinder, S, Camborde, M L, Raywood, K and Sossi, V 2007 A scatter-corrected list-mode reconstruction and a practical scatter/random approximation technique for dynamic PET imaging *Phys. Med. Biol.* **52** 8 2089-106
- Floberg, J M, Mistretta, C A, Weichert, J P, Hall, L T, Holden, J E and Christian, B T 2012 Improved kinetic analysis of dynamic PET data with optimized HYPR-LR *Med. Phys.* **39** 3319-31
- Greene, M W, Stang, L G, Jr and Hillman, M 1963 Labeling of Human Gamma Globulin with I-124. Bnl 777 (T-293) *Tech. Rep. Brookhaven Natl. Lab.* **86** 1-4
- Laforest, R and Liu, X 2009 Cascade removal and microPET imaging with ⁷⁶Br *Phys. Med. Biol.* **54** 6 1503-31

- Larson, S M, Pentlow, K S, Volkow, N D, Wolf, A P, Finn, R D, Lambrecht, R M, Graham, M C, Di Resta, G, Bendriem, B and Daghigian, F 1992 PET scanning of iodine-124-3F9 as an approach to tumor dosimetry during treatment planning for radioimmunotherapy in a child with neuroblastoma *J. Nucl. Med.* **33** 11 2020-3
- Lippincott, S W, Corcoran, C, Jansen, C R, Jesseph, J E, Rai, K, Aronow, S, Greene, M W and Sweet, W H 1964 Labeling of Human Globulin with I-124 for Positron Scanning of Neoplasms *J. Nucl. Med.* **5** 193-9
- Lopci, E, Chiti, A, Castellani, M R, Pepe, G, Antunovic, L, Fanti, S and Bombardieri, E 2011 Matched pairs dosimetry: 124I/131I metaiodobenzylguanidine and 124I/131I and 86Y/90Y antibodies *Eur. J. Nucl. Med. Mol. Imaging* **38 Suppl 1** S28-40
- Lubberink, M, Schneider, H, Bergstrom, M and Lundqvist, H 2002 Quantitative imaging and correction for cascade gamma radiation of 76Br with 2D and 3D PET *Phys. Med. Biol.* **47** 19 3519-34
- Mangner, T J, Wu, J L and Wieland, D M 1982 Solid-phase exchange radioiodination of aryl iodides. Facilitation by ammonium sulfate. *J Org Chem.* **47** 8 1484-8
- O'Donoghue, J A *et al* 2011 124I-huA33 antibody uptake is driven by A33 antigen concentration in tissues from colorectal cancer patients imaged by immuno-PET *J. Nucl. Med.* **52** 12 1878-85
- Pinchuk, A N, Rampy, M A, Longino, M A, Skinner, R W, Gross, M D, Weichert, J P and Counsell, R E 2006 Synthesis and structure-activity relationship effects on the tumor avidity of radioiodinated phospholipid ether analogues *J. Med. Chem.* **49** 7 2155-65
- Rampy, M A, Chou, T S, Pinchuk, A N, Skinner, R W, Gross, M D, Fisher, S, Wahl, R and Counsell, R E 1995a Synthesis and biological evaluation of radioiodinated phospholipid ether analogs *Nucl. Med. Biol.* **22** 4 505-12
- Rampy, M A, Pinchuk, A N, Weichert, J P, Skinner, R W, Fisher, S J, Wahl, R L, Gross, M D and Counsell, R E 1995b Synthesis and biological evaluation of radioiodinated phospholipid ether stereoisomers *J. Med. Chem.* **38** 16 3156-62
- Sgouros, G, Hobbs, R F, Atkins, F B, Van Nostrand, D, Ladenson, P W and Wahl, R L 2011 Three-dimensional radiobiological dosimetry (3D-RD) with 124I PET for 131I therapy of thyroid cancer *Eur. J. Nucl. Med. Mol. Imaging* **38 Suppl 1** S41-7
- Smith, S V 2004 Molecular imaging with copper-64 *J. Inorg. Biochem.* **98** 11 1874-901
- Watson, C C, Newport, D, Casey, M E, deKemp, R A, Beanlands, R S and Schmand, M 1997 Evaluation of Simulation-Based ScatterCorrection for 3-D PET Cardiac Imaging *IEEE Trans Nucl Sci* **44** 90-7

Weichert, J P, Van Dort, M, Groziak, M P and Counsell, R E 1986 Radioiodination via Isotope Exchange in Pivalic Acid *Appl. Radiat. Isot.* **37** 8 907-13

Chapter 8. Impact of Expectation-Maximization Reconstruction Iterations on the Diagnosis of Temporal Lobe Epilepsy with PET

8.1 Introduction

The utility of the denoising methods developed in this thesis must ultimately be demonstrated in the context of real imaging tasks. For example, their ability to improve the detection of trends, to reveal new patterns or findings, and to improve clinical diagnosis must still be proven. While such validation studies have not been undertaken as part of this thesis, assessing the impact of the bias-variance tradeoff seen with a simpler means of controlling noise on a clinical imaging task is illuminating. This chapter aims to accomplish this by investigating the impact of the number of iterations performed in expectation-maximization (EM) reconstruction on the clinical diagnosis of temporal lobe epilepsy (TLE) with 2-deoxy-2-([F-18])fluoro-D-glucose ([F-18]FDG) positron emission tomography (PET).

EM reconstruction with ordered subsets (OSEM) is now widely used for diagnostic PET, and there is a well-known tradeoff between increased image sharpness and increased noise variance as the number of EM iterations is increased during reconstruction (Shepp and Vardy 1982, Hudson and Larkin 1994, Barrett *et al* 1994, Wilson *et al* 1994). The impact of the number of iterations performed on diagnostic accuracy has been studied in the context of several imaging tasks (Gilland *et al* 1992, Wells *et al* 1999, Wells *et al* 2000, LaCroix *et al* 2000, Gifford *et al* 2000), and unsurprisingly the optimal implementation of EM reconstruction is dependent on the task. However, to my knowledge such a study has not been undertaken for the diagnosis of TLE with [F-18]FDG PET.

PET with [F-18]FDG has become an integral part in the diagnosis and pre-surgical evaluation of temporal lobe epilepsy (TLE), and its diagnostic efficacy and ability to predict surgical outcomes have been demonstrated in numerous studies (Theodore *et al* 1992, Manno *et al* 1994, Casse *et al* 2002, Theodore *et al* 2001). TLE is diagnosed on [F-18]FDG PET by identifying hypometabolic regions with decreased [F-18]FDG uptake in a diseased temporal lobe relative to a healthy contralateral one. The diagnosis may be difficult to make if the degree of hypometabolism is subtle, and [F-18]FDG uptake in small regions may be obscured if resolution is poor or noise variance is high. A number of approaches have been developed to improve diagnosis by reducing partial volume effects, for example by using anatomical information from MRI scans, to make small hypometabolic regions more detectable (Baete *et al* 2004, Goffin *et al* 2010, Kato *et al* 2008). However, such correction methods are not readily available at most clinical centers and their use is only beginning to be validated.

Simply increasing the number of iterations performed during expectation-maximization (EM) reconstruction is a much more clinically accessible approach to reducing partial volume effects. In the context of [F-18]FDG PET for TLE, a greater number of iterations may increase image sharpness and thus improve the detectability of small regions of hypometabolism, but this may be offset by the associated increase in image noise. Currently, the specific reconstruction algorithm used for TLE PET studies is typically determined by physician or institutional preference. An optimal reconstruction algorithm may therefore be clinically useful.

8.2 Chapter Aims

The aim of this chapter is to investigate the impact of EM iteration number on the diagnosis of TLE with two OSEM reconstructions. The diagnostic performance of the two reconstructions

is evaluated with a blinded reader study using a receiver operating characteristic (ROC) analysis of the predictive power of [F-18]FDG PET for identifying surgical candidates. The sensitivities of the two different reconstructions for identifying patients who improved with surgery are also compared.

8.3 Methods

8.3.1 Subject Selection

This study was carried out as a retrospective analysis of clinical [F-18]FDG PET studies previously acquired at the University of Wisconsin-Madison for the diagnosis of medically intractable TLE. The medical and imaging records of all patients (n=184) who received [F-18]FDG PET scans for the diagnosis of TLE between 2000-2010 were investigated for inclusion and exclusion criteria as follows. Inclusion criteria included diagnosis or suspicion of TLE; consideration for surgical treatment of epilepsy; age ≥ 18 years; clinical documentation of age, gender, seizure onset, and seizure frequency, antiepileptic drug (AED) trials, EEG report, PET report, MRI report, and in patients ultimately receiving surgery: postoperative follow-up, including seizure frequency and character. Exclusion criteria included a history of cerebral vascular accident (CVA), brain tumor, head trauma, tuberous sclerosis, prior cranial surgery, and hemispheric congenital malformations (e.g., porencephaly, lissencephaly, perisylvian polymicrogyria, hemimegalencephaly).

Medical records were then reviewed to determine the documented findings of [F-18]FDG PET, MRI, EEG exams, and postoperative outcomes. [F-18]FDG PET was deemed positive if unilateral temporal lobe hypometabolism was noted in the medical record. MRI was deemed positive if mesiotemporal sclerosis, hippocampal atrophy, unilateral temporal atrophy, or

temporal gliosis were noted. EEG was deemed localizing if reports indicated that seizures originated from one temporal lobe. Surgical outcome data were evaluated in patients who had at least one assessment of their postoperative seizure course in the electronic medical record. Surgical outcomes were graded according to the International League Against Epilepsy (ILAE) scale (Wieser *et al* 2001). For the purposes of this study, surgical outcomes were further categorized as positive for ILAE scores of 1-4 (1 = absence of seizures, 4 = 4 seizures per year up to a 50% seizure reduction from baseline), and negative for scores of 5 or 6 (less than a 50% reduction in seizures from baseline). Of the patients receiving surgery, only one had a negative outcome (ILAE score of 5). Following the compilation of these data, subjects were anonymized. The general characteristics of this population of subjects and an analysis of their outcomes has previously been published (Struck *et al* 2011).

A subset of 32 subjects was then selected for use in the blinded reader study. This subset of subjects was selected to maximize the number of patients whose scans were initially read as negative with positive surgical outcomes (i.e. false negatives), as the interpretation of these scans is plausibly the most likely to change. The other scans included were selected such that the population of patients used in the reader study maintained the general diagnostic characteristics of the overall population of patients who received [F-18]FDG PET for TLE, while maximizing the number of scans from patients with surgical results. In particular, the percentage of scans initially read as positive and negative was kept approximately the same between the subset of subjects used in the reader study and all [F-18]FDG PET studies acquired to diagnose TLE, as was the proportion of scans with findings concordant and discordant with MRI and/or EEG.

8.3.2 PET Image Acquisition and Reconstruction Protocols

Patients fasted for 6 hours prior to injection of [F-18]FDG. Diabetic patients were instructed to withhold diabetic medications for 6 hours and blood glucose measurements were required to be < 200 mg/dL at the time of tracer injection. Patients were injected intravenously with 0.14 mCi/kg (minimum of 10 mCi) [F-18]FDG, and were then instructed to relax quietly for 45 minutes in a dimly lit room. Patients were imaged at 60 minutes after injection with one of two scanners: an Advance PET scanner and a Discovery VCT PET/CT scanner (GE Healthcare).

Two OSEM reconstructions were performed on each [F-18]FDG PET exam. The first used the reconstruction parameters typical for clinical PET brain scans at the University of Wisconsin for the type of scanner used. These reconstructions were considered the smooth, relatively low-resolution, and low-noise standards. The second reconstruction increased the number of iterations used during reconstruction, while keeping all other parameters constant. The specific number of iterations to be used for the second set of reconstructions was determined by a nuclear medicine physician using a test set of subjects by qualitatively determining the number of iterations at which possible increased confidence in the diagnosis would be offset by increased noise. These reconstructions served as the sharper, higher noise comparisons. Pertinent reconstruction parameters are summarized in Table 8.2, and example reconstructions from each scanner for [F-18]FDG PET scans initially read as both positive and negative are shown in Figure 8.1. Note that 3D OSEM reconstructions of shorter acquisitions with more subsets (35 versus 28) were used for the Discovery VCT, which is standard practice for this scanner at the University of Wisconsin. Corrections for normalization, deadtime, and scatter radiation were applied using system software. Attenuation correction was applied to the scans acquired on the

Table 8.1. Reconstruction parameters for each scanner used in the study. The number of iterations was the only parameter varied between the two OSEM reconstructions for each patient exam.

Scanner	GE Advance	GE Discovery VCT
Reconstruction	2D OSEM	3D OSEM
Matrix Size	128x128x35	128x128x47
Voxel Size	2.3x2.3x4.25 mm ³	2.3x2.3x3.27 mm ³
Number of Subsets	28	35
Number of Iterations: Smooth	2	2
Number of Iterations: Sharp	5	5
Post-Smoothing Filter (Gaussian FWHM)	3.27 mm	2.57 mm

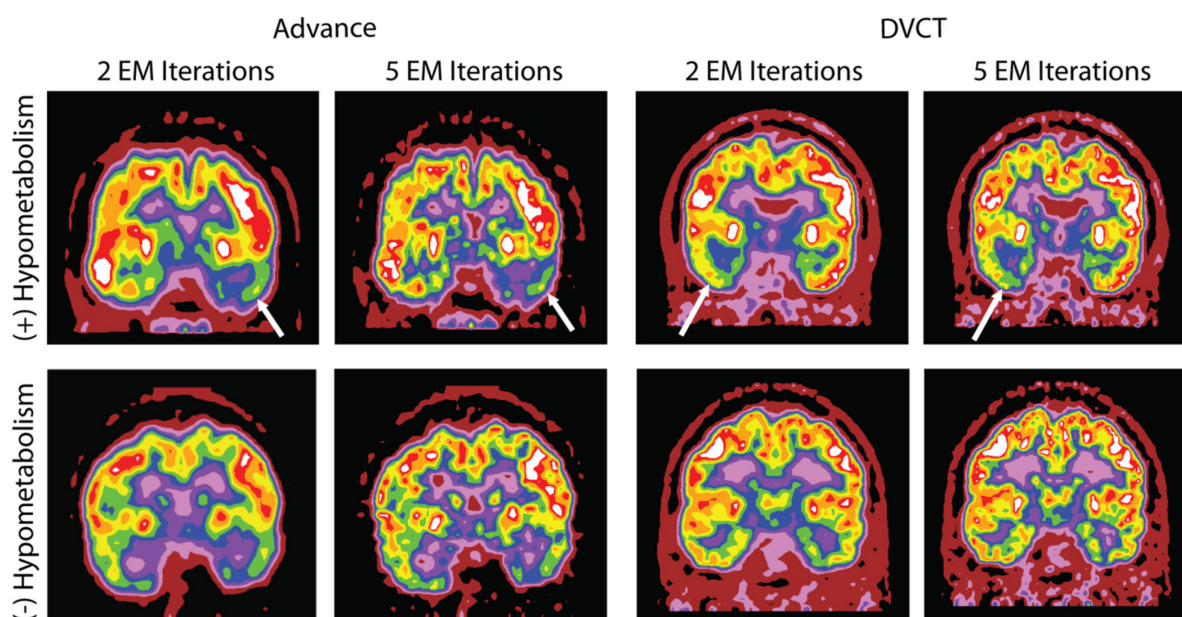


Figure 8.1. Example images of the reconstructions studied. Example slices are shown of the 2 different VCT reconstructions that were compared for both the GE Advance and GE Discovery VCT scanners used in the study. Examples from each scanner for patients with [F-18]FDG PET scans initially read as positive and with positive surgical outcomes, and for patients with [F-18]FDG PET scans initially read as negative who did not receive surgery are both shown. Hypometabolic regions are indicated with arrows.

GE Advance using a transmission scan acquired with two Ge-68 rod sources, and to the scans acquired on the GE Discovery VCT using a co-registered CT scan.

8.3.3 Reader Study Design and Analysis

Each individual reconstruction was assigned a random number and all associated patient, exam, and reconstruction information were removed. All reconstructions were then presented to the blinded readers interspersed randomly. Two readers, reader 1 and reader 2, assigned a diagnostic score of 1-5 to each reconstructed image (1 = unequivocal hypometabolic focus, 2 = strong confidence of hypometabolic focus, 3 = moderate confidence of hypometabolic focus, 4 = equivocal for hypometabolic focus, 5 = no hypometabolic focus). Readers were also blinded to MRI, EEG, and other clinical findings.

ROC curves for surgical candidacy were then generated for each reconstruction, and analyzed for each reader separately and with their results combined. The area under the curve (AUC) was calculated for each ROC curve, and curves for smooth reconstructions (2 EM iterations) were compared with curves for sharp reconstructions (5 EM iterations) using the nonparametric comparison approach of DeLong et al. (DeLong *et al* 1988).

As only one patient out of all the patients meeting the overall inclusion and exclusion criteria had a negative surgical outcome as defined for this study (ILAE score of 5 or 6), the specificity of [F-18]FDG-PET for predicting surgical outcomes cannot be assessed. Therefore, only the sensitivities of the two OSEM reconstructions for identifying patients who improved with surgery at each level of reader confidence were compared. Ninety-five percent confidence intervals (CIs) were found for the sensitivities at each level of diagnostic confidence using the Clopper-Pearson interval, and McNemar's test was used to test for significance.

Access to imaging and medical records of used for the purpose of this study and permission to reprocess and reinterpret imaging studies was approved by the local institutional review board.

8.4 Results

8.4.1 Subject Selection

A total of 120 patients met the initial inclusion and exclusion criteria and 32 were included in the reader study. As outlined above, the subset of 32 scans used for the reader study were selected to maximize the number of scans whose initial interpretations were false negative while keeping the percentage of scans initially read as [F-18]FDG PET positive and negative for hypometabolism, and with concordant and discordant MRI and/or EEG findings, approximately the same as in the 120 patients meeting the inclusion and exclusion criteria. Of the 32 patients included in the reader study, 26 were scanned on the GE advance and 6 were scanned on the GE Discovery VCT. The diagnostic characteristics of the scans selected for the reconstruction study and for the overall population of patients undergoing [F-18]FDG PET for TLE are summarized in Figure 8.2. Of the patients receiving surgery who were included in the reader study (n=18), 9 had an ILAE outcome of 1 (seizure free), 4 had an ILAE outcome of 2 (auras, but no seizures), 4 had ILAE outcomes of 3 (1-3 seizures per year), and 1 had an outcome of 5 (<50% reduction from baseline). The representation of these outcomes in the reader study population is likewise similar to their representation in the overall population of patients receiving surgery. Two patients were identified as surgical candidates but had not received surgery at the time of data collection. One patient was awaiting surgery at the time the study was conducted, and one did

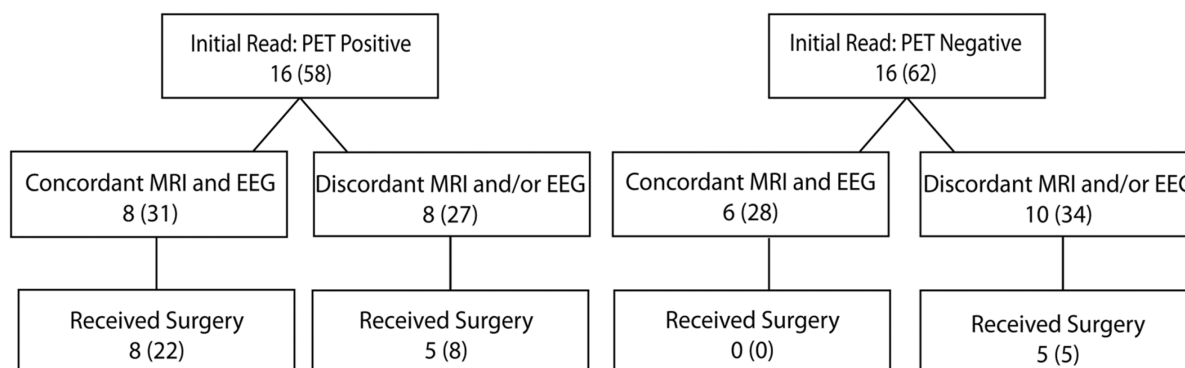


Figure 8.2. Patient population diagnostic characteristics. The diagnostic characteristics of the patient scans included in the study are shown. The characteristics of all of the [F-18]FDG PET scans acquired for TLE diagnosis that met the initial inclusion and exclusion criteria are also included in parentheses. The proportion of scans initially read as positive and negative, and concordant and discordant with MRI and/or EEG were kept approximately the same between the scans included in the reader study and the overall number of scans meeting the inclusion and exclusion criteria. All but one of the patients who received surgery showed clinical improvement, and the patient who did not improve had an [F-18]FDG PET scan initially read as negative.

not proceed with surgical treatment. Both of these patients were scanned on the Discovery VCT.

8.4.2 Reader Study Results

The two readers were very consistent in their interpretations of the [F-18]FDG scans, regardless of the number of iterations used. When the results of the two readers are combined, 48/64 (75%) of the studies were given an identical rating between the two reconstructions, and 13/64 (20.3%) were given ratings that differed by one degree of reader confidence.

The ROC curves for surgical candidacy are shown in Figure 8.3. The ROC curves of the individual readers and their combined results are both included. The area under each curve and

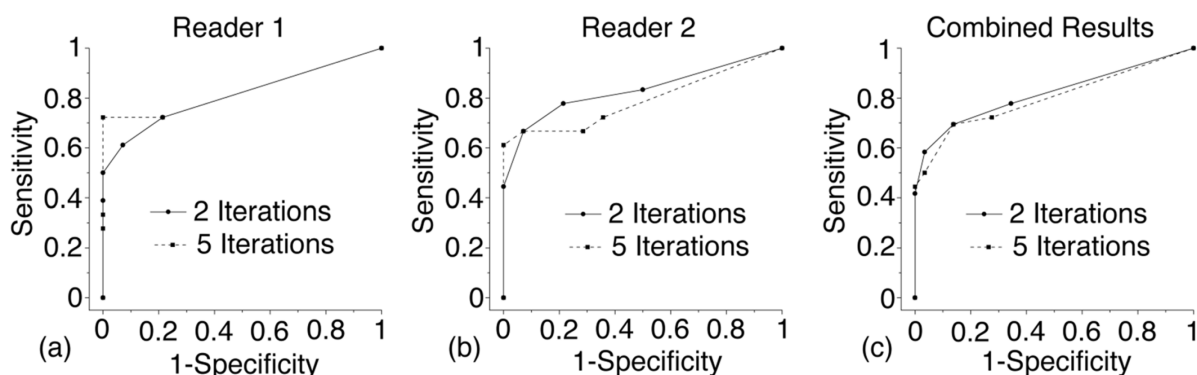


Figure 8.3. Surgical candidacy ROC curves. ROC curves for surgical candidacy are shown for both readers individually (a & b), and with their results combined (c). Smooth reconstructions (2 EM iterations) are compared with sharp reconstructions (5 EM iterations) in each case. There was no statistically significant difference between the AUC of the two reconstructions for either reader separately or with their results combined.

Table 8.2. The areas under the ROC curves from each reconstruction for the individual readers and with their results combined. The P-values for the differences between the AUCs of each reconstruction are shown. None reached significance. The AUCs and the P-values comparing them after excluding the scans acquired of the GE Discovery VCT are also shown. The exclusion of these scans did not alter the results.

Surgical Candidacy	All Scans			Discovery VCT Excluded		
	Reader 1	Reader 2	Combined	Reader 1	Reader 2	Combined
OSEM Iterations						
2	0.839	0.812	0.821	0.888	0.815	0.850
5	0.806	0.831	0.807	0.833	0.830	0.828
P-value	0.563	0.280	0.674	0.470	0.442	0.595

the results of the nonparametric statistical comparison between them are summarized in Table 8.2. There was no statistically significant difference between the AUCs for the reconstructions with 2 iterations and 5 iterations for either of the outcomes. This was true for the results of both readers individually and with their results combined. As the acquisitions and reconstructions from the GE Discovery VCT were 3-dimensional and those from those from the GE Advance were 2-dimensional, the areas under ROC curves excluding the scans acquired on the GE DVCT

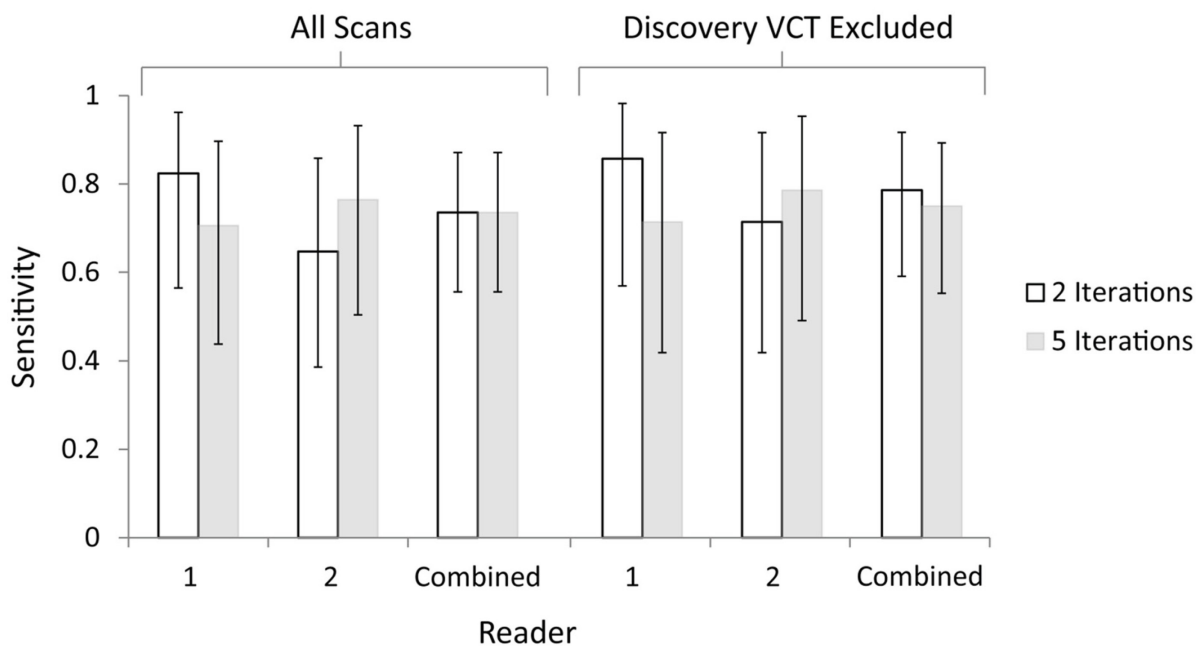


Figure 8.4. The sensitivity of [F-18]FDG PET for predicting a positive surgical outcome for the two OSEM reconstructions studied. There was no statistically significant difference in the sensitivities of the reconstructions for either of the readers, or with their results combined. Excluding the scans acquired on the GE Discovery VCT did not alter the results.

(n= 6) were also examined (Table 8.2). Excluding the GE Discovery VCT scans also excludes the two patients identified as surgical candidates but who had not received surgery at the time of data collection. Excluding these scans did not alter the results.

The sensitivities of the 2 iteration and 5 iteration OSEM reconstructions for predicting surgical outcome at a moderate level of diagnostic confidence (images rated 3 or higher counted as positive reads) are shown in Figure 8.4. There was no significant difference between the two reconstructions for each reader separately or with their results combined. This was true at all other levels of diagnostic confidence as well (data not shown). As with the ROC curves for surgical candidacy, excluding the scans acquired on the Discovery VCT did not alter the results.

8.5 Discussion

The aim of this study was to retrospectively investigate the impact of the number of iterations performed during OSEM reconstruction on the sensitivity and specificity of [F-18]FDG PET for predicting surgical candidacy and surgical outcomes in TLE. This was done with a blinded reader study comparing two OSEM reconstructions, differing in the number of iterations performed. The ability of [F-18]FDG PET to predict surgical candidacy was evaluated with a ROC analysis of the two reconstructions, and the sensitivities of the two reconstructions for predicting surgical outcomes were compared. In the cases studied here, the number of iterations performed during OSEM reconstruction had no statistically significant impact on the sensitivity and specificity of [F-18]FDG PET for predicting surgical candidacy, or its sensitivity for predicting surgical outcome. The nuclear medicine physicians' interpretations of the PET studies were essentially unchanged by the different reconstructions, illustrated by the consistency with which they interpreted the images between the two reconstructions studied. Therefore using physician preference to determine reconstruction parameters seems justified and acceptable in this case. These results should be tempered by the limited statistical power of the results.

The hypometabolic regions identified by nuclear medicine physicians tended to be more global decreases in FDG uptake in the temporal lobe (Figure 8.1). Smaller lesions may not have been identified in either reconstruction, as they may have remained too blurred in the original reconstructions, and obscured by noise in the reconstructions with more iterations. It is possible that reconstructing with a number of iterations between 2 and 5 would be more optimal and would result in a better trade-off between image sharpness and noise variance.

Partial volume correction methods that aim to increase image sharpness while suppressing noise to improve the identification of small hypometabolic regions were not considered (Baete *et al* 2004, Goffin *et al* 2010, Kato *et al* 2008). Such methods are not yet widely available as clinical tools, whereas changing the number of iterations used in OSEM reconstructions can readily be performed and therefore may have a more immediate impact. Given that the results do not indicate any benefit to using the sharper but noisier images obtained with more iterations, more advanced partial volume correction methods might be needed to identify smaller regions of hypometabolism. However, if physicians rely on identifying a pattern of globally reduced [F-18]FDG uptake, such methods may make little difference in subjective interpretation. If this is the case, one of the more objective methods of detecting small regions of hypometabolism might be required (Kumar *et al* 2010, Didelot *et al* 2010).

This work has focused on the number of iterations performed during OSEM reconstruction in order to study the tradeoff between bias and variance (resolution and noise in this case), but there are a number of other factors that will influence resolution and noise. The most notable extraneous factors in this study are the two PET cameras that were used, the GE Advance and the Discovery VCT, and the different acquisitions and reconstruction used for each scanner, 2D acquisition with 2D OSEM reconstruction for the Advance and a shorter 3D acquisition with 3D OSEM reconstruction using more subsets (35 versus 28) for the Discovery VCT (Table 8.1). The overall impact of these differences on the images from the two scanners is difficult to determine. The 3D acquisition and reconstruction of the Discovery VCT images should result in better noise properties in the images, but this may be offset by the shorter acquisition time. Likewise, the greater number of subsets used during reconstruction should give sharper images for the same number of iterations, though image sharpness is also likely influenced by the 3D acquisition.

Rather than attempting to address each of these issues, this work has instead focused only on the impact of iteration number by demonstrating that excluding the Discovery VCT scans does not significantly alter the results.

All reconstructions used for PET imaging have parameters that will affect the tradeoff between bias and variance. While these parameters are frequently determined by physician and institutional preference, it is possible that they could have an impact on diagnostic outcomes. This investigation indicates that this may not be the case with OSEM reconstructions of [F-18]FDG PET images acquired for the diagnosis of TLE, as little difference was found between the two reconstructions studied. This work is limited by its statistical power, by extraneous variables such as the two PET cameras used, and in that only two possible numbers of iterations were examined. However, the consistency with which the readers interpreted the images indicates that a substantial number of scans would have to be read to identify any difference between reconstructions. Different reconstruction parameters, such as an intermediate number of iterations between 2 and 5, may have made a greater impact on the interpretation of scans, but the consistency of the interpretations makes this unlikely as well. If changing the number of iterations performed in reconstruction had potential to change interpretations, less consistency would be expected in the data presented here, even if the area under the ROC curves and the sensitivities are nearly equivalent. As such it appears perfectly reasonable to use images that nuclear medicine physicians are most familiar and comfortable with. Nevertheless, such studies could be helpful in validating and optimizing the reconstruction and image processing methods used in different clinical imaging tasks. This may be particularly valuable in the future for validating the use of the denoising methods presented in this thesis: Highly constrained back-

Projection-Local Reconstruction (HYPR-LR) processing and spatio-temporal expectation-maximization (STEM) filtering.

8.6 Conclusions

This retrospective blinded analysis investigated the impact of the number of iterations performed during OSEM reconstruction on the interpretation of [F-18]FDG PET scans acquired for the diagnosis of TLE. No difference was found between the reconstructions studied. This implies that the reconstructions used for the subjective clinical interpretation of [F-18]FDG PET scans acquired for TLE can be determined by physician preference. More sophisticated means of partial volume correction may have a more significant impact on the diagnostic interpretation of such scans. The methodology presented in this chapter could be used in the future to demonstrate the clinical utility of HYPR-LR processing and STEM filtering.

References

- Baete, K, Nuyts, J, Van Paesschen, W, Suetens, P and Dupont, P 2004 Anatomical-based FDG-PET reconstruction for the detection of hypo-metabolic regions in epilepsy *IEEE Trans. Med. Imaging* **23** 4 510-9
- Barrett, H H, Wilson, D W and Tsui, B M 1994 Noise properties of the EM algorithm: I. Theory *Phys. Med. Biol.* **39** 5 833-46
- Casse, R, Rowe, C C, Newton, M, Berlangieri, S U and Scott, A M 2002 Positron emission tomography and epilepsy *Mol. Imaging Biol.* **4** 5 338-51
- DeLong, E R, DeLong, D M and Clarke-Pearson, D L 1988 Comparing the areas under two or more correlated receiver operating characteristic curves: a nonparametric approach *Biometrics* **44** 3 837-45
- Didelot, A, Mauguiere, F, Redoute, J, Bouvard, S, Lothe, A, Reilhac, A, Hammers, A, Costes, N and Ryvlin, P 2010 Voxel-based analysis of asymmetry index maps increases the specificity of [F-18]MPPF PET abnormalities for localizing the epileptogenic zone in temporal lobe epilepsies *J. Nucl. Med.* **51** 11 1732-9

- Gifford, H C, King, M A, Wells, R G, Hawkins, W G, Narayanan, M V and Pretorius, P H 2000 LROC analysis of detector-response compensation in SPECT *IEEE Trans. Med. Imaging* **19** 5 463-73
- Gilland, D R, Tsui, B M, Metz, C E, Jaszczak, R J and Perry, J R 1992 An evaluation of maximum likelihood-expectation maximization reconstruction for SPECT by ROC analysis *J. Nucl. Med.* **33** 3 451-7
- Goffin, K, Van Paesschen, W, Dupont, P, Baete, K, Palmi, A, Nuyts, J and Van Laere, K 2010 Anatomy-based reconstruction of FDG-PET images with implicit partial volume correction improves detection of hypometabolic regions in patients with epilepsy due to focal cortical dysplasia diagnosed on MRI *Eur. J. Nucl. Med. Mol. Imaging* **37** 6 1148-55
- Hudson, H M and Larkin, R S 1994 Accelerated image reconstruction using ordered subsets of projection data *IEEE Trans. Med. Imaging* **13** 4 601-9
- Kato, H, Shimosegawa, E, Oku, N, Kitagawa, K, Kishima, H, Saitoh, Y, Kato, A, Yoshimine, T and Hatazawa, J 2008 MRI-based correction for partial-volume effect improves detectability of intractable epileptogenic foci on 123I-iomazenil brain SPECT images *J. Nucl. Med.* **49** 3 383-9
- Kumar, A, Juhasz, C, Asano, E, Sood, S, Muzik, O and Chugani, H T 2010 Objective detection of epileptic foci by [F-18]FDG PET in children undergoing epilepsy surgery *J. Nucl. Med.* **51** 12 1901-7
- LaCroix, K J, Tsui, B M, Frey, E C and Jaszczak, R J 2000 Receiver operating characteristic evaluation of iterative reconstruction with attenuation correction in 99mTc-sestamibi myocardial SPECT images *J. Nucl. Med.* **41** 3 502-13
- Manno, E M, Sperling, M R, Ding, X, Jaggi, J, Alavi, A, O'Connor, M J and Reivich, M 1994 Predictors of outcome after anterior temporal lobectomy: positron emission tomography *Neurology* **44** 12 2331-6
- Shepp, L A and Vardy, Y 1982 Maximum Likelihood Reconstruction for Emission Tomography *IEEE Trans. Med. Imaging* **1** 113
- Struck, A F, Hall, L T, Floberg, J M, Perlman, S B and Dulli, D A 2011 Surgical decision making in temporal lobe epilepsy: a comparison of [(18)F]FDG-PET, MRI, and EEG *Epilepsy Behav.* **22** 2 293-7
- Theodore, W H, Gaillard, W D, De Carli, C, Bhatia, S and Hatta, J 2001 Hippocampal volume and glucose metabolism in temporal lobe epileptic foci *Epilepsia* **42** 1 130-2

- Theodore, W H, Sato, S, Kufta, C, Balish, M B, Bromfield, E B and Leiderman, D B 1992 Temporal lobectomy for uncontrolled seizures: the role of positron emission tomography *Ann. Neurol.* **32** 6 789-94
- Wells, R G, King, M A, Simkin, P H, Judy, P F, Brill, A B, Gifford, H C, Licho, R, Pretorius, P H, Schneider, P B and Seldin, D W 2000 Comparing filtered backprojection and ordered-subsets expectation maximization for small-lesion detection and localization in 67Ga SPECT *J. Nucl. Med.* **41** 8 1391-9
- Wells, R G, Simpkin, P H, Judy, P F and King, M A 1999 Maximizing the detection and localization of Ga-67 tumors in thoracic SPECT MLEM(OSEM) reconstructions *IEEE Trans Nucl Sci* **46** 4 1191-8
- Wieser, H G, Blume, W T, Fish, D, Goldensohn, E, Hufnagel, A, King, D, Sperling, M R, Luders, H, Pedley, T A and Commission on Neurosurgery of the International League Against Epilepsy (ILAE) 2001 ILAE Commission Report. Proposal for a new classification of outcome with respect to epileptic seizures following epilepsy surgery *Epilepsia* **42** 2 282-6
- Wilson, D W, Tsui, B M and Barrett, H H 1994 Noise properties of the EM algorithm: II. Monte Carlo simulations *Phys. Med. Biol.* **39** 5 847-71

Chapter 9. Conclusions and Future Directions

This thesis aimed to develop and evaluate Highly constrained back-Projection-Local Reconstruction (HYPR-LR) and spatio-temporal expectation-maximization (STEM) filtering as methods for denoising dynamic positron emission tomography (PET) data. These methods are of potential value because they can be tailored to specific applications and datasets, either explicitly with HYPR-LR or implicitly with STEM, to reduce noise while introducing little bias. They are also easy to implement, and can potentially complement other denoising methods. These characteristics make HYPR-LR processing and STEM filtering applicable to a wide range of dynamic PET studies, giving them potential to impact the use of PET imaging and broaden the modality's scope and potential both clinically and in research.

9.1 HYPR-LR Processing

This thesis proposed an optimized implementation of HYPR-LR for PET imaging and rigorously evaluated the algorithm's performance in the context of the kinetic analysis of dynamic PET tracer data. The optimized implementation of HYPR-LR uses multiple time-dependent composite images (HYPR-LR-MC) that account for the temporal behavior of the tracer being studied to try and provide the greatest degree of noise reduction that is possible without introducing any bias. HYPR-LR-MC has been compared to HYPR-LR using a full composite formed with all study frames (HYPR-LR-FC), which will provide the greatest possible reduction in noise at the potential cost of introduced bias. The performance of HYPR-LR-MC and HYPR-LR-FC were evaluated using [C-11]PIB data.

Both of these implementations of HYPR-LR improve the kinetic analysis of dynamic PET data, particularly quantitative parametric images. HYPR-LR-FC provides the greatest

improvements in the variance of quantitative parameters, but does bias the data. However, the bias is not that great in the measures used in this work. HYPR-LR-MC also improves variance, albeit not to the same degree as HYPR-LR-FC, and does so while introducing little bias.

9.2 STEM Filtering

This thesis developed STEM filtering as another method for reducing noise in dynamic PET data. Like HYPR-LR, STEM filtering is data driven in that the filtering process will be unique for every dataset. However, the uniqueness of a given application of STEM filtering will be determined implicitly through the use of EM deconvolution, as opposed to the explicitly defined composite image ranges in HYPR-LR-MC. This makes the application of STEM filtering less *ad hoc* than HYPR-LR, potentially making its application to a broad range of dynamic PET studies easier.

STEM filtering has been shown to significantly improve both individual time frames in dynamic PET studies and quantitative parameter estimates. It does so while introducing little bias into the data studied in this work. Like HYPR-LR, this gives STEM filtering potential to make significant impacts on both clinical and research PET imaging applications.

9.3 Application of HYPR-LR Processing and STEM Filtering to [I-124] PET Imaging

This thesis evaluated HYPR-LR processing and STEM filtering as methods to improve PET imaging with [I-124] labeled agents. [I-124] could be a very useful radionuclide for PET imaging because of its unique chemical properties and relatively long (4.2 day) half-life. However, its use may be limited by noise because of radiation dosimetry concerns combined with a low

percentage of decays via positron emission (23%). HYPR-LR processing and STEM filtering could thus be of great benefit to [I-124] PET images.

The applications of HYPR-LR and STEM filtering to [I-124] images presented in this work are distinct from their applications to conventional tracer studies because most of the [I-124] datasets studied were acquired as serial images, as opposed to a single dynamic acquisition. HYPR-LR and STEM filtering can both significantly improve noise in such applications. Their use may therefore prove valuable for other serially acquired PET data, for example images of radiolabeled antibodies and other molecules with physiological half-lives of hours to days. This thesis has begun to explore some of the challenges that must be dealt with to apply denoising methods to such studies, for example the effects of motion, registration, and changing object size, but these issues must be dealt with more rigorously in the future.

9.4 Limitations of the Evaluation of HYPR-LR and STEM

This work has demonstrated that HYPR-LR and STEM filtering can significantly improve the analysis of dynamic PET data. However, it has not demonstrated that these algorithms can improve real-world imaging tasks. For example, this work has not shown that the HYPR-LR and STEM can improve the detection of pathology using imaging. This thesis has also not rigorously compared the algorithms to other more sophisticated denoising methods. While the simplicity and effectiveness of HYPR-LR and STEM filtering make their use appealing, such comparisons must be undertaken in the context of true imaging tasks to ultimately demonstrate the potential of these methods to impact the clinical and research use of PET.

9.5 Impact of EM Reconstruction Iterations on Temporal Lobe Epilepsy Diagnosis

While this thesis did not evaluate the ability of HYPR-LR processing and STEM filtering to improve real-world imaging tasks and outcomes, it has evaluated the impact of a simpler means of denoising on clinical diagnosis. In particular, Chapter 8 has evaluated the impact of the number of iterations performed during ordered subset EM reconstruction (OSEM) on the ability of physicians to diagnose temporal lobe epilepsy (TLE) using [F-18]FDG PET. Image sharpness and noise variance increase with increasing numbers of EM iterations, and both of these factors might have an impact on clinical diagnosis.

However, in the data studied here, altering the number of iterations performed during reconstruction had essentially no impact on physicians' abilities to accurately diagnose TLE. This result suggests that the current practice of selecting reconstruction parameters largely based upon institutional and physician preference may be reasonable. It also suggests that image processing methods, and denoising methods in particular, may need to dramatically improve image quality to make a significant impact on clinical diagnosis. This may be because the human eye-brain system provides a substantial level of "noise reduction" in the form of pattern recognition in tasks involving human observers. Denoising methods may also prove valuable in non-observer dependent tasks, for example thresholding methods and statistical parametric mapping.

9.6 Future Work

This thesis has largely focused on the development of HYPR-LR processing and STEM filtering as image processing tools for 4-dimensional PET, and lays the groundwork for their use.

However, to be proven as truly valuable methods, future work must rigorously evaluate their impact on real-world outcomes from imaging experiments and clinical tasks. The evaluation of the impact of the number of EM iterations on the diagnosis of TLE with [F-18]-FDG PET is an example of how such an evaluation could be done in the context of clinical imaging tasks. Future studies should also focus on how HYPR-LR, STEM filtering, and established methods could improve clinical and research tasks that are based on the kinetic analysis of dynamic PET data. Kinetic analysis of PET data gives tremendously valuable information, arguably the most quantitative of any imaging modality, but its use is currently limited in part by noise (Rahmim *et al* 2009). Studies that firmly demonstrate improved outcomes using these denoising methods could truly broaden the scope and potential of dynamic PET imaging.

References

- Rahmim, A, Tang, J and Zaidi, H 2009 Four-dimensional (4D) image reconstruction strategies in dynamic PET: beyond conventional independent frame reconstruction *Med. Phys.* **36** 8 3654-70

Appendix A. Kinetic Analysis Methods for PET Tracer Data

Three simplified kinetic analysis methods are used throughout this work: the reference region Logan graphical method (Logan *et al* 1990, Logan *et al* 1996), receptor parametric mapping (RPM or RPM2) (Lammertsma and Hume 1996, Gunn *et al* 1997, Wu and Carson 2002), and the reference region Patlak graphical method (Patlak *et al* 1983, Patlak and Blasberg 1985). This appendix gives an overview of these methods.

A.1 Kinetic Analysis of Tracers with Reversible Binding Behavior

The kinetic behavior of the tracers with reversible binding behavior presented in this work, [C-11]PIB and [C-11]raclopride, are typically described by the two-tissue compartment model or the simplified one-tissue compartment model. In the two-tissue compartment model, the tracer can be considered either unbound (C_1) or bound (C_2) in tissues, and the transfer of tracer from the plasma to these compartments can be described by the rate constants K_1 , k_2 , k_3 , and k_4 (Figure A.1a). In the simplified one-tissue compartment case, it becomes difficult to distinguish between bound and unbound tracer and they can be collapsed into a single compartment, simplifying the fitting task. The rate constants thus become K_1 and k_{2a} , where k_{2a} is the apparent overall rate constant for the transfer of tracer from tissue to plasma (Figure A.1b) (Lammertsma and Hume 1996). In terms of the two-tissue compartment model rate constants, k_{2a} is:

$$k_{2a} = \frac{k_2}{(1 + k_3 / k_4)} \quad (\text{A.1})$$

Additionally, the reversible tracers in this work are modeled using a reference region as an input. The reference region is assumed to have no specific binding (Figure A.1c).

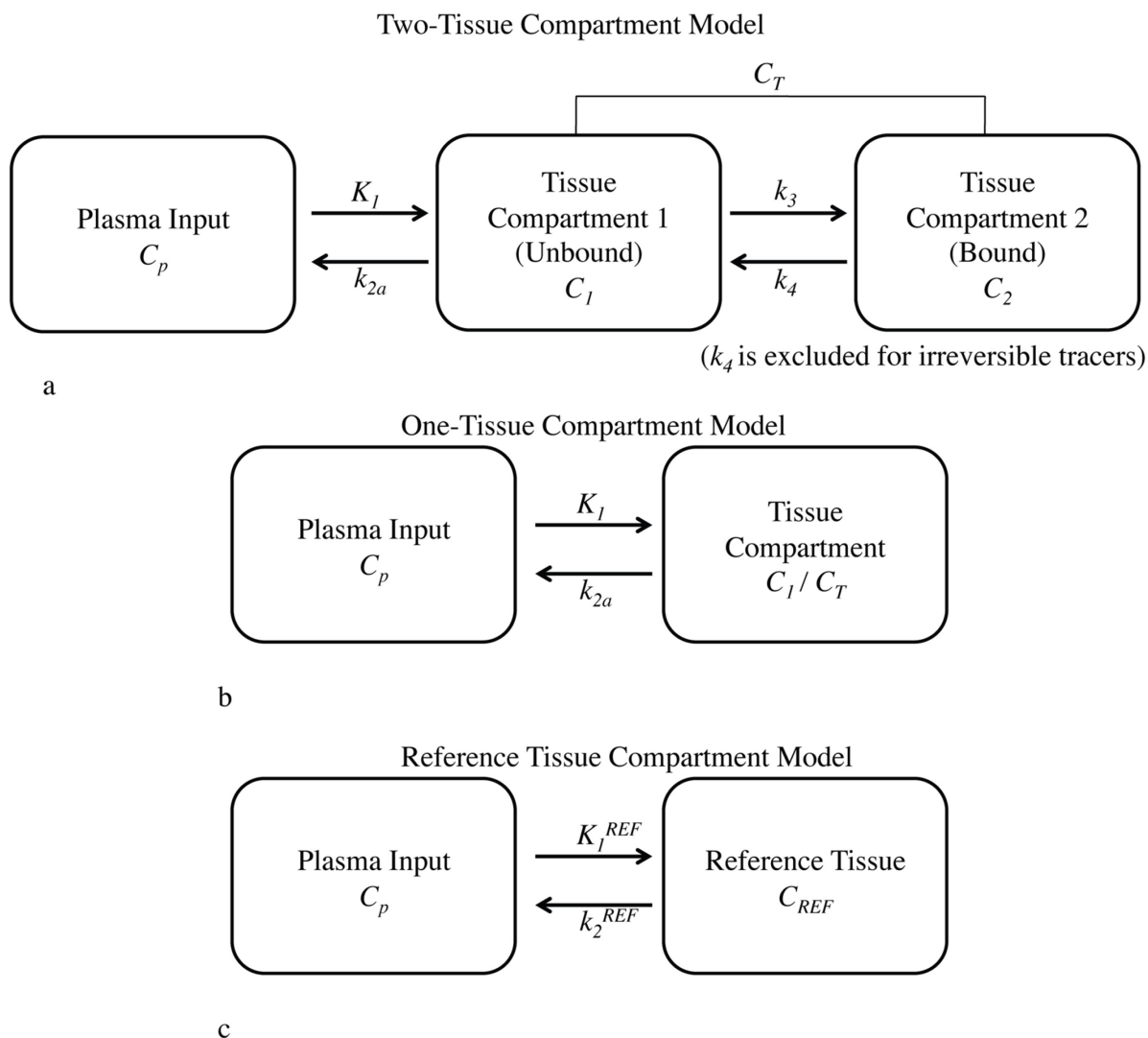


Figure A.1. The kinetic models used in this thesis, including the two-tissue compartment model (a), the simplified one-tissue compartment model (b), and the model for the reference tissue that is used as an input in all the simplified analysis methods presented in this work (c).

This work primarily concerns itself with aggregate quantitative parameters, namely the distribution volume ratio (DVR) and the non-displaceable binding potential (BP_{ND}). The distribution volume (DV) is the ratio, at true equilibrium, of the amount of tracer in tissue relative to that in plasma. The DVR is the ratio of the DV in a tissue with specific binding to the

DV in a region with no specific binding. The BP_{ND} is the ratio of specifically bound to unbound (non-displaceable) tracer at equilibrium. In terms of the kinetic rate constants of the two-tissue compartment model, these parameters can be defined as:

$$DVR = \frac{K_1/k_2(1+k_3/k_4)}{K_1^{REF}/k_2^{REF}} \quad (A.2)$$

$$BP_{ND} = \frac{k_3}{k_4} \quad (A.3)$$

The ratios K_1/k_2 and K_1^{REF}/k_2^{REF} are typically assumed to be the same, so DVR becomes $(1+k_3/k_4)$, and BP_{ND} is then simply $DVR-1$.

For the simplified one-tissue compartment model, the DVR can be expressed as:

$$DVR = \frac{K_1/k_{2a}}{K_1^{REF}/k_2^{REF}} \quad (A.4)$$

Combining Equations A.4 and A.1 yields the same DVR as in the two-tissue compartment case:

$$DVR = (1 + BP_{ND}).$$

A.1.1 Logan Graphical Analysis

Logan graphical analysis with a reference tissue input is one of the methods used in this work to analyze the tracers with reversible binding behavior. Logan graphical analysis relates the measured data from tissue time-activity curves (TACs) and a reference region TAC with the following linear equation:

$$\frac{\int_0^T C_T(t) dt}{C_T(T)} = DVR \left[\frac{\int_0^T C_{REF}(t) dt + C_{REF}(T)/k_2^{REF}}{C_T(T)} \right] + \text{int} \quad (A.5)$$

where $C_T(t)$ is the TAC of interest (e.g. a voxel TAC for parametric images) $C_{REF}(t)$ is the TAC of the reference tissue, k_2^{REF} is the efflux rate constant for the reference tissue, DVR is the distribution volume ratio (the parameter of primary interest), and int is the y-intercept (Logan *et al* 1990, Logan *et al* 1996). For some tracers, for example [C-11]-raclopride, the term in equation A.5 with k_2^{REF} can be ignored, as its inclusion makes no effective difference in the calculation of the DVR (Logan 2000). A linear fit to this equation after the intercept has achieved a state of equilibrium, at $t=t^*$, yields a slope equal to DVR, from which BP_{ND} is easily calculated.

A.1.2 Receptor Parametric Mapping

[C-11]PIB and [C-11]raclopride data presented in this work were also analyzed with RPM2. RPM is a basis function implementation of the simplified reference tissue method (Figure A.1b) (Lammertsma and Hume 1996, Gunn *et al* 1997). This assumes that all TACs in the data can be fit to the simplified reference tissue model using Equation A.6:

$$C_T(t) = R_1 C_{REF}(t) + R_1 (k_2^{REF} - k_{2a}) C_{REF}(t) \otimes \exp(-k_{2a} t) \quad (a)$$

$$R_1 = \frac{K_1}{K_1^{REF}} \quad (b) \quad (A.6)$$

$$BP_{ND} = R_1 \frac{k_2^{REF}}{k_{2a}} - 1 \quad (c)$$

where $C_T(t)$ and $C_{REF}(t)$ are the same as defined above, and K_1 , K_1^{REF} , k_{2a} , and k_2^{REF} are the efflux rate constants for the simplified one-tissue compartment model. RPM2 creates a set of exponential basis functions over a range of k_{2a} values to simplify the fitting process. In this work, minimum and maximum values for k_{2a} were determined from non-linear least squares fits to Eq. 3 of several ROI TACs from the data being analyzed. Variance can be improved by fixing k_2^{REF}

after an initial fitting of each voxel in the image to equation A.6 (RPM2) (Wu and Carson 2002). Although three parameters can be obtained from analysis with RPM2, this work is concerned only with BP_{ND} estimates.

A.2 Irreversible Tracers

The behavior of irreversible tracers, such as [F-18]FDOPA used in this work, is also typically described with a two-tissue compartment model. However, there is assumed to be no efflux of the tracer out of the specifically bound compartment (Figure A.1a). As is the case with the irreversible tracers in this work, [F-18]-FDOPA is modeled using a reference region input, where the reference region is assumed to have no specific binding (Figure A.1c). The parameter of primary interest in the [F-18]-FDOPA studies is the uptake rate constant, K_i^* , another aggregate parameter that describes the net influx of tracer from the plasma into the tissue of interest, relative to the influx in a reference region. It is defined as:

$$K_i^* = \frac{k_2 k_3}{(k_2 + k_3)} \quad (\text{A.7})$$

A.2.1 Patlak Graphical Analysis

Patlak graphical analysis with a reference region input was used to analyze the irreversible kinetics of the [F-18]-FDOPA data presented in this work (Patlak *et al* 1983, Patlak and Blasberg 1985). Patlak graphical analysis is similar to Logan analysis, but it relates the measured TACs from tissues with irreversible binding behavior to the TAC of a reference region:

$$\frac{C_T(T)}{C_{REF}(T)} = K_i^* \frac{\int_0^T \exp(-k_b(T-t)) C_T(t) dt}{C_{REF}(T)} + \text{int} \quad (\text{A.8})$$

$C(t)$ and $C_{REF}(t)$ are the same as defined above, k_b is a constant that accounts for a small degree of reversible binding behavior (assumed to be 0 in this work), int is the y-intercept term, and K_i^* is the parameter of interest as defined above. A linear fit to this equation yields K_i^* .

References

- Gunn, R N, Lammertsma, A A, Hume, S P and Cunningham, V J 1997 Parametric imaging of ligand-receptor binding in PET using a simplified reference region model *Neuroimage* **6** 4 279-87
- Lammertsma, A A and Hume, S P 1996 Simplified reference tissue model for PET receptor studies *Neuroimage* **4** 3 Pt 1 153-8
- Logan, J 2000 Graphical analysis of PET data applied to reversible and irreversible tracers *Nucl. Med. Biol.* **27** 7 661-70
- Logan, J, Fowler, J S, Volkow, N D, Wang, G J, Ding, Y S and Alexoff, D L 1996 Distribution volume ratios without blood sampling from graphical analysis of PET data *J. Cereb. Blood Flow Metab.* **16** 5 834-40
- Logan, J, Fowler, J S, Volkow, N D, Wolf, A P, Dewey, S L, Schlyer, D J, MacGregor, R R, Hitzemann, R, Bendriem, B and Gatley, S J 1990 Graphical analysis of reversible radioligand binding from time-activity measurements applied to [N-11C-methyl]-(-)-cocaine PET studies in human subjects *J. Cereb. Blood Flow Metab.* **10** 5 740-7
- Patlak, C S and Blasberg, R G 1985 Graphical evaluation of blood-to-brain transfer constants from multiple-time uptake data. Generalizations *J. Cereb. Blood Flow Metab.* **5** 4 584-90
- Patlak, C S, Blasberg, R G and Fenstermacher, J D 1983 Graphical evaluation of blood-to-brain transfer constants from multiple-time uptake data *J. Cereb. Blood Flow Metab.* **3** 1 1-7
- Wu, Y and Carson, R E 2002 Noise reduction in the simplified reference tissue model for neuroreceptor functional imaging *J. Cereb. Blood Flow Metab.* **22** 12 1440-52

Appendix B. A Kinetic Model for the Cancer Imaging and Therapy Agent NM404

B.1 Introduction

NM404 is a radioiodinated phospholipid ether analog that has demonstrated selective uptake and prolonged retention in 52 of 54 cancers in preclinical and clinical studies (Weichert *et al* 2005, Pinchuk *et al* 2006). This gives the compound great potential as a diagnostic agent that can be used for both imaging diagnosis and targeted radionuclide therapy (TRT). [I-124]NM404 was presented in Chapter 7 of this thesis as an example [I-124] PET imaging agent that could benefit from novel denoising methods.

The chemical properties and pharmacokinetics of NM404 have been well studied (Pinchuk *et al* 2006). However, there has been no attempt to describe the pharmacokinetics of NM404 with a compartmental model. Such a model could serve as a standard for quantifying the uptake of the compound in different tumors. This in turn could be useful in estimating radiation dosimetry for NM404, and predicting and assessing response to TRT with [I-131]NM404 or other therapies. In addition, a complete mechanism the compound's uptake and retention has yet to be elucidated. A compartmental model that accurately describes the kinetics could thus yield clues about the biological processes involved. The aim of this appendix is to present pharmacokinetic data of [I-124]NM404 obtained with PET imaging, and to establish a compartmental model that describes its uptake in solid tumors.

B.2 Methods

B.2.1 Animal Preparation

Eight nude mice (Harlan, Madison, WI) were inoculated with 1×10^6 human colon adenocarcinoma LS180 cells suspended in PBS between the shoulder blades. Mice were selected for imaging 7-14 days later when tumor volumes were between 22.3 and 259 mm³ (mean 104 mm³).

At the start of the imaging experiment, mice were injected with 7.4-14.8 MBq of [I-124]NM404 via tail vein. NM404 was prepared and radiolabeled with [I-124] as previously described (Pinchuk *et al* 2006). Tail veins were catheterized to ensure clean bolus injection using catheters constructed in house with 30 gauge needles and PE-1 tubing (Scientific Commodities, Lake Havasu, AZ). Catheters were filled with heparin during their placement to ensure patency of the line, and flushed with 100-150 μ L normal saline following [I-124]NM404 injection.

B.2.2 Imaging Procedure

Following injection of [I-124]NM404, mice were imaged on an Inveon microPET/CT system (Siemens Healthcare, Inc.) at 1, 6, 12, 24, 36, 48, 72, 120, 168, and 240 hours post-injection (p.i.). Mice were anesthetized with 2% isoflurane prior to and during image acquisition. PET emission scans were acquired in 3-dimensional (3-D) mode to 30-40 million detected events. Images were reconstructed using the system's 3-D ordered subset expectation maximization/Maximum *a posteriori* (3-D OSEM/MAP) algorithm (2 EM iterations, 16 subsets, 18 MAP iterations, β smoothing factor = 0), to a matrix size of 128x128x159 with voxel sizes of 0.8x0.8x0.8 mm³. Corrections for deadtime, randoms, attenuation, and scatter were applied using the system software. Attenuation and scatter corrections were applied using the co-registered CT

scans. Animal experiments were conducted under a protocol approved by the local Institutional Animal Care and Use Committee.

B.2.3 Data Analysis and Kinetic Modeling

Volumes of interest (VOIs) of the tumor and left ventricle were drawn on each CT image and time-activity curves (TACs) were generated from the co-registered PET data. Input functions were generated from the left ventricle VOIs, assuming a hematocrit of 30%, no uptake in red blood cells, and no metabolites present in the blood. TACs were decay corrected to the time of injection.

Tumor TACs were fit to either a one or two-tissue compartment model (see Appendix A, **Error! Reference source not found.**) using the image derived input functions. The one-tissue compartment model can be described by the differential equation:

$$\frac{dC_{Tumor}}{dt} = K_1 C_{Plasma}(t) - k_2 C_{Tumor}(t) \quad (B.1)$$

where $C_{Tumor}(t)$ is the concentration of [I-124]NM404 in the tumor, $C_{Plasma}(t)$ is the concentration in the blood plasma (including tracer bound to albumin), and K_1 and k_2 are rate constants. In the case of the two-tissue compartment model, the concentration in the tumor can be described as:

$$C_{Tumor}(t) = C_1(t) + C_2(t) \quad (B.2)$$

where $C_1(t)$ and $C_2(t)$ are the concentrations of [I-124]NM404 in tissue compartments 1 and 2, respectively. The differential equations for $C_1(t)$ and $C_2(t)$ are:

$$\begin{aligned} \frac{dC_1}{dt} &= K_1 C_{Plasma}(t) - k_2 C_1(t) \\ \frac{dC_2}{dt} &= k_3 C_1(t) - k_4 C_2(t) \end{aligned} \quad (B.3)$$

Fits of the measured tumor TACs to these models were performed using the COMKAT software package (Muzic and Cornelius 2001). Time points were equally weighted as all PET acquisitions were performed to the same number of detected events.

B.2.4 Akaike Weights

The appropriateness of each model was assessed using Akaike weights, a normalized expression for the Akaike information criterion (AIC) (Burnham and Anderson 1998, Turkheimer *et al* 2003). The AIC rewards models that fit the data well in the least-squares sense, and penalizes models based on their complexity (Akaike 1983). The AIC can be calculated from PET data as:

$$\begin{aligned} \text{AIC} &= n \log(\hat{\sigma}^2) + 2P \\ \hat{\sigma}^2 &= \frac{\sum \hat{\varepsilon}_i^2}{n} \end{aligned} \quad (\text{B.4})$$

where n is the number of data points, $\hat{\varepsilon}_i$ are the residuals from the fitted model, and P is the number of parameters in the model. The Akaike weight, w_i , for the model i can then be found as:

$$\begin{aligned} w_i &= \frac{\exp(-\Delta_i / 2)}{\sum_{r=1}^M \exp(-\Delta_r / 2)} \\ \Delta_i &= \text{AIC}_i - \min \text{AIC} \end{aligned} \quad (\text{B.5})$$

where $\min \text{AIC}$ is the minimum value of the AIC for the model set being studied, and M is the total number of models in the set. A lower Akaike weight indicates a better model fit to the data.

B.3 Results

Tumors show slow but significant uptake of [I-124]NM404. Tumor activity exceeds that of the image-derived blood TAC at approximately 24 hours, and peaks around 72-96 hours. After

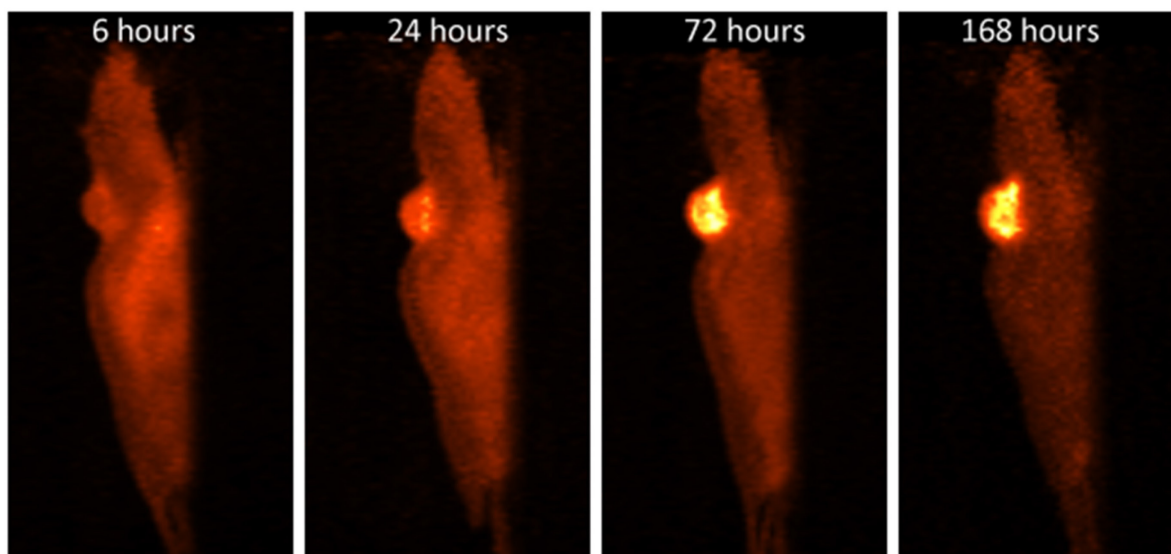


Figure B.1. A visual illustration of the pharmacokinetics of [I-124]-NM404. Projection images of the PET data are showed at 6, 24, 72, and 169 hours post-injection.

its peak, tumor activity steadily declines at approximately the same rate as the blood activity (Figure B.1 & Figure B.2).

A two-tissue compartment model better fits the tumor TACs than the one-tissue compartment model (Figure B.2), as evident by a substantially larger mean Akaike weight. The Akaike weight was greater for the one-tissue compartment model in one dataset (Table B.1).

The mean results of the two-tissue compartment model fits to the eight tumor TACs studied are summarized in Table B.2. The individual rate constants k_1 and k_2 were not identifiable, though their ratio was. NM404's relatively low K_1/k_2 ratio, small k_3 , and very small k_4 reflect its long plasma half-life and the slow but significant uptake of the compound by tumors.

B.4 Discussion and Conclusions

This appendix has evaluated the pharmacokinetics of [I-124]-NM404 using PET imaging, determined that a two-tissue compartment model best describes the kinetics of the data using the

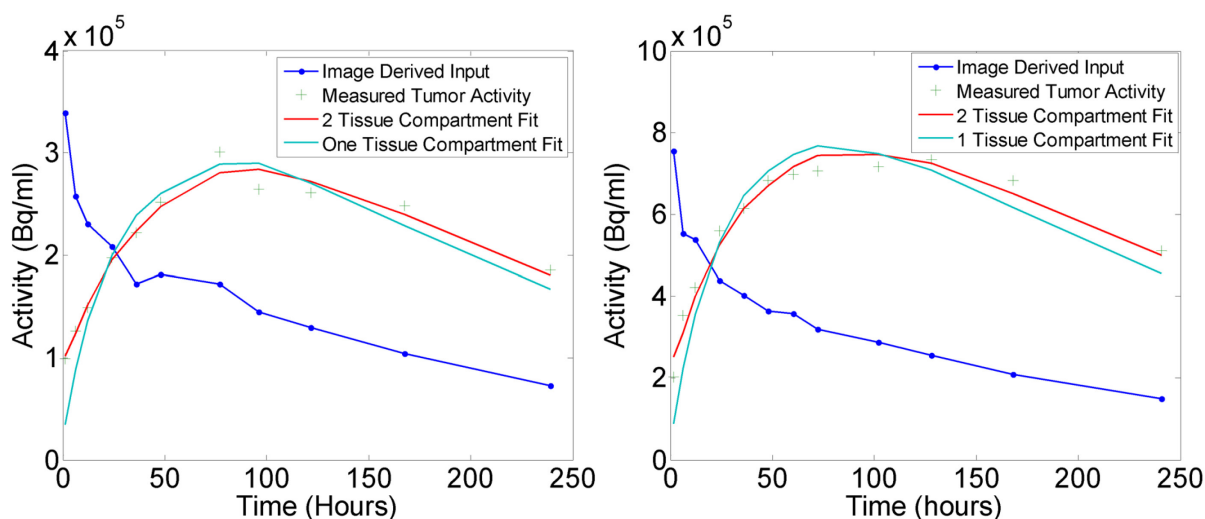


Figure B.2. Representative curves for image derived plasma input functions, measured tumor activities, and one and two-tissue compartment fits. The two-tissue compartment model provides a superior fit, confirmed by an Akaike weight of 0.711 vs. 0.289 for the one-tissue compartment model for the data on the left, and and 0.999 vs. 1.87×10^{-5} for the data on the right.

Table B.1. Appropriateness of the one and two-tissue compartment models for the kinetics of [I-124]NM404 as assessed by the AIC. The mean and standard deviation of the Akaike weights from the eight datasets analyzed are shown for each of the models studied. A lower Akaike weight indicates a better model fit.

	Mean Akaike Weight	Akaike Weight Standard Deviation
One-Tissue Compartment Model	0.776	0.358
Two-Tissue Compartment Model	0.225	0.335

AIC, and measured the pharmacokinetic parameters of fits to this model. In this colorectal cancer model, NM404 behaves much like the reversible tracers typically seen in dynamic PET scans, but with a time course of hours to days instead of minutes.

This kinetic behavior supports what is known about the compound's physiologic mechanism. Namely, the compound is highly bound to albumin in plasma (Pinchuk *et al* 2006), as evident by

Table B.2. Rate constants from fits of the [I-124]NM404 data to the two-tissue compartment model. The mean, standard deviation, and range of the parameters from the eight mice studied are shown. K1 and k2 were not individually identifiable, but their ratio was.

	K1/k2	k3 (min ⁻¹)	k4 (min ⁻¹)	DV (ml/cm ³)
Average	0.28	0.0013	0.00028	1.6
SD	0.036	0.00028	5.1x10 ⁻⁵	0.28
Range	(0.22-0.32)	(9.3x10 ⁻⁴ -1.9x10 ⁻³)	(2.1 x10 ⁻⁴ -3.6 x10 ⁻⁴)	1.2-2.0

its very gradual uptake by tumors, relatively low K₁/k₂ ratio, and small k₃. The small k₃ reflects the slow but specific uptake of [I-124]NM404 by tumors, and the even smaller k₄ reflects how the compound is retained. The underlying mechanism of this specific uptake and retention has not yet been fully elucidated, but the results presented here suggest that such a mechanism does exist. There is also apparently some mechanism by which the compound is cleared. This may be true physiologic clearance, but may also represent cells that die as aggressive tumors become necrotic, or tumor growth that results in the same amount of radioactivity being dispersed over a larger volume. If a complete mechanism for NM404 is found, the ability to quantify individual rate constants could provide insight into important tumor biology.

The two-tissue compartment model proposed here provides a means of quantifying NM404's uptake in different tumor models non-invasively using PET imaging. This might be useful in predicting dosimetry for TRT with ¹³¹I-NM404, predicting tumor response to any therapeutic modality, and quantifying an underlying biological process that is apparently widespread in human cancers, and therefore potentially of significant importance to malignancy.

References

- Akaike, H 1983 Information Measures and Model Selection *Int Stat Inst* **44** 277-91
- Burnham, K and Anderson, D R 1998 *Model Selection and Inference: A Practical Information-Theoretic Approach* (New York, NY: Springer-Verlag)
- Muzic, R F, Jr and Cornelius, S 2001 COMKAT: compartment model kinetic analysis tool *J. Nucl. Med.* **42** 4 636-45
- Pinchuk, A N, Rampy, M A, Longino, M A, Skinner, R W, Gross, M D, Weichert, J P and Counsell, R E 2006 Synthesis and structure-activity relationship effects on the tumor avidity of radioiodinated phospholipid ether analogues *J. Med. Chem.* **49** 7 2155-65
- Turkheimer, F E, Hinz, R and Cunningham, V J 2003 On the undecidability among kinetic models: from model selection to model averaging *J. Cereb. Blood Flow Metab.* **23** 4 490-8
- Weichert, J P, Moser, A R, Weber, S M, Qi, C and Logino, M 2005 Radioiodinated NM404-a Universal Tumor Imaging Agent? *Acad Rad* **12** 5, Supplement 1 S58-S59

Appendix C. Evaluation of the Diapetic Agent NM404 in a Rat Glioma Model with PET and MRI

C.1 Introduction

Malignant gliomas are a virulent form of brain cancer that carry a very poor prognosis (Nieder *et al* 2004b). This poor prognosis is due to the fact that gliomas are exceptionally difficult to treat (Nieder *et al* 2004b, Stupp *et al* 2005, Nieder *et al* 2004a), and current modalities for imaging gliomas are limited in their ability to both evaluate the cancer and guide therapy (Pirrotte *et al* 2006, Pirrotte *et al* 2009, Watanabe *et al* 1992, Wen *et al* 2010). NM404, the phospholipid ether analog introduced in Chapter 7 of this thesis, has demonstrated avidity for glioma cells in xenograft tumor models. Thus, NM404 is a potentially useful agent for both evaluating gliomas, either with PET using [I-124] or optically using fluorescent moieties, and treating it with [I-131] or [I-125]. This could include using [I-124]NM404 PET to both guide and evaluate targeted radionuclide therapy (TRT) with [I-131]NM404. However, to date no study has evaluated NM404 in an orthotopic animal model of glioma. Such a study could provide insight into and information about NM404's behavior in gliomas and other brain cancers that cannot easily be obtained from the human studies presented in Chapter 7. This appendix presents data collected to evaluate the diagnostic and therapeutic potential of NM404 in gliomas using an orthotopic rat model with [I-124]NM404 and positron emission tomography (PET). [I-124]NM404 uptake is compared to gadolinium contrast enhanced (CE) magnetic resonance imaging (MRI), and [F-18]-3-deoxy-3-fluorothymidine (FLT) PET. These data are not used to evaluate the novel denoising methods developed in this thesis, but are instead presented to provide additional information about the behavior of [I-124]NM404 in malignant brain tumors.

C.2 Methods

C.2.1 Cancer Model

Fourteen nude rats (*rmu*) were inoculated intra-cranially with 10^6 U87 cells suspended in 5 μ l of phosphate buffered saline (PBS). Cells were injected at the following coordinates with respect to the bregma: 4mm lateral, 1 mm posterior, and 5 mm deep. Rats were inoculated on 3 occasions using the same procedure and divided into two groups with separate imaging protocols as described below (group 1, n=10; group 2, n=3). Two rats in group 1 were injected with PBS only as controls. Rats were screened for the presence of tumors with T2 weighted MRI. The imaging experiment was begun when tumors were at least 2 mm in diameter (4-5 weeks post-inoculation).

C.2.2 MRI Imaging

At the start of the imaging experiment, all rats were first imaged with T1 weighted MRI before and after administration of 0.3 mg (1 mg/ml) of Multi-hance. Scanning was performed on a Varian 4.7 T small animal MRI with an in-house rat head coil. Images were acquired using a gradient echo pulse sequence (TR = 7 ms, TE = 4 ms, flip angle = 45° , number of experiments = 4) and reconstructed to an image matrix size of 128x128x256 with isotropic voxel sizes of $0.2 \times 0.2 \times 0.2$ mm³. MRI was repeated before sacrifice.

C.2.3 PET Imaging

NM404 was prepared and radiolabeled with [I-124] as previously described (Pinchuk *et al* 2006). [F-18]FLT was prepared as described by Martin *et al.* (Martin *et al* 2002), modified for synthesis on a Scansys (Denmark) radiochemistry module.

Rats in group 1 were injected with 7.88-21.4 MBq (213-579 μCi) [I-124]NM404 via a tail vein catheter and imaged with PET/CT 24, 48 and 96 hours post-injection. Immediately prior to injection of [I-124]NM404, 5 rats in group 1, including one control, were imaged with PET/CT following injection of 13.3-22.6 MBq (358-610 μCi) [F-18]FLT using a dynamic PET acquisition ($t=90$ minutes) initiated at the time of tracer injection. Rats in group 2 were injected with 8.40-24.1 MBq (227-651 μCi) of [I-124]NM404 and imaged with PET/CT every 24 to 48 hours up to 240 hours post-injection. All PET/CT scanning was performed on an Inveon hybrid PET/CT system (Siemens Healthcare, Inc.).

PET images were reconstructed with filtered back-projection (FBP) to a matrix size of $256 \times 256 \times 159$ with voxel sizes of $0.4 \times 0.4 \times 0.8 \text{ mm}^3$. Corrections for normalization, deadtime, attenuation, and scatter were applied using the system software. Attenuation correction was performed using the co-registered CT scan.

Uptake of tracers was quantified in regions of interest (ROIs) using mean and maximum SUV. SUV was measured for each tracer (60-90 minutes for [F-18]FLT, 96 hours for [I-124]NM404) in tumor regions of interest (ROIs) showing high tracer uptake and in regions identified as possible tumor on MRI but showing low tracer uptake. [I-124]NM404 uptake at 96 hours was compared to gadolinium enhancement on the MRI scan acquired on the same day, and to uptake of [F-18]FLT prior to [I-124]NM404 injection.

C.2.3 Histology

Following sacrifice, tumors were characterized histologically by tissue specimens stained with H&E. Immediately after the final MRI scan, animals were sacrificed, brains were removed, and fixed in formalin for 24 hours. Following formalin fixation, samples were stored in

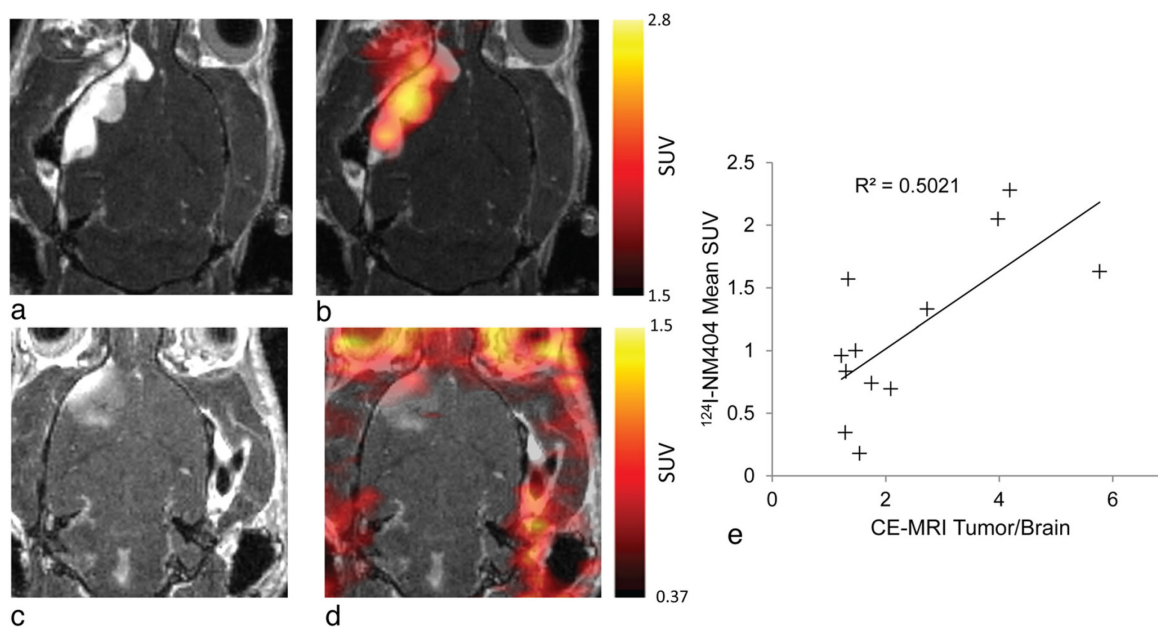


Figure C.1. A comparison of [I-124]NM404 uptake and gadolinium enhancement. Example images of a lesion that shows intense enhancement with gadolinium on T1 weighted MRI (a) and high [I-124]NM404 uptake (b), and a lesion that shows little enhancement with gadolinium (c) and correspondingly low uptake of [I-124]NM404 (d). [I-124]NM404 uptake at 96 hours post-injection is correlated with the tumor-to-healthy brain ratio on CE-MRI acquired on the same day ($p=0.01$) (e).

PBS. Samples were then embedded in paraffin, cut into 10 micron slices in regions with lesions confirmed on MRI and/or PET, and stained with H&E.

C.3 Results

C.3.1 [I-124]NM404 Uptake versus CE-MRI

The mean SUV ($t = 96$ hours) of [I-124]NM404 in the suspected tumor ROIs showing high and low uptake of the agent is well correlated with the degree of gadolinium enhancement in the same regions. (Figure C.1). Regions with high [I-124]NM404 uptake tend to show significant enhancement following the administration of gadolinium, and regions with minimal [I-

¹²⁴I-NM404 uptake show minimal gadolinium enhancement. However, not all regions of high gadolinium enhancement show high ¹²⁴I-NM404 uptake (Figure C.1b).

C.3.2 [I-124]NM404 versus [F-18]FLT Uptake

Maximum [F-18]FLT SUV trends toward correlation with the maximum SUV for [I-124]NM404 at 96 hours p.i. (Figure C.2), though the sample presented here is not large enough for this trend to reach significance. There was no uptake of [F-18]FLT and [I-124]NM404 in the brain of the control animal, and those data are not included in Figure C.2. [F-18]FLT and [I-124]NM404 uptake do not perfectly overlap (Figure C.2a & b). These results must be considered alongside the fact that [F-18]FLT PET scans were acquired 96 hours before the [I-124]NM404 scans, and during this time the tumor likely changed.

C.3.3 Longitudinal Scanning with [I-124]NM404

In the rats scanned over the course of 10 days (group 2), tumors continue to show [I-124]NM404 uptake as they grow (Figure C.3). The degree of uptake appears to be related to tumor size. This is likely due in part to volume averaging effects.

C.3.4 Histology

Regions of high and low [I-124]NM404 uptake show different pathologic characteristics (Figure C.4). Namely, tumor regions with high uptake on PET tend to be subarachnoid (particularly in group 2), have higher cellular density, a greater degree of extracellular proteinaceous material, and tend to be more nodular and not infiltrative. The tumors from the

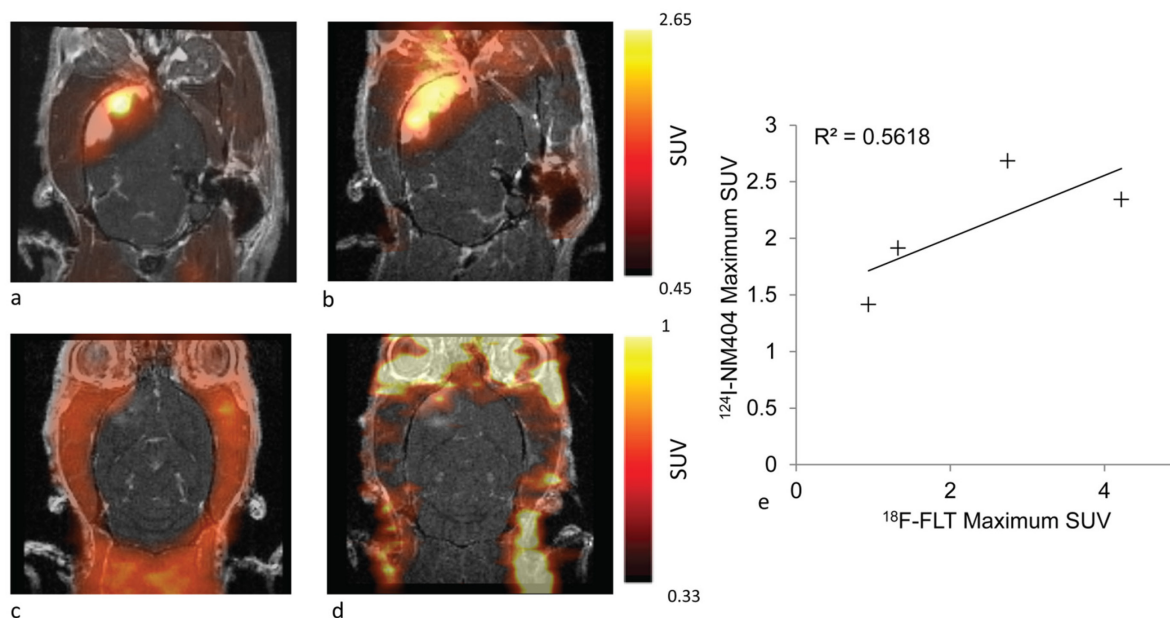


Figure C.2. Comparison of [I-124]NM404 and [F-18]FLT uptake. Example images of a lesion that shows high [I-124]NM404 uptake (a) and high [F-18]FLT uptake, and a lesion that shows low uptake of [I-124]NM404 (c) and low uptake of [F-18]FLT uptake. The maximum SUV of [I-124]NM404 at 96 hours shows a correlation with the maximum SUV of [F-18]FLT, but it does not reach significance ($p=0.250$) (e).

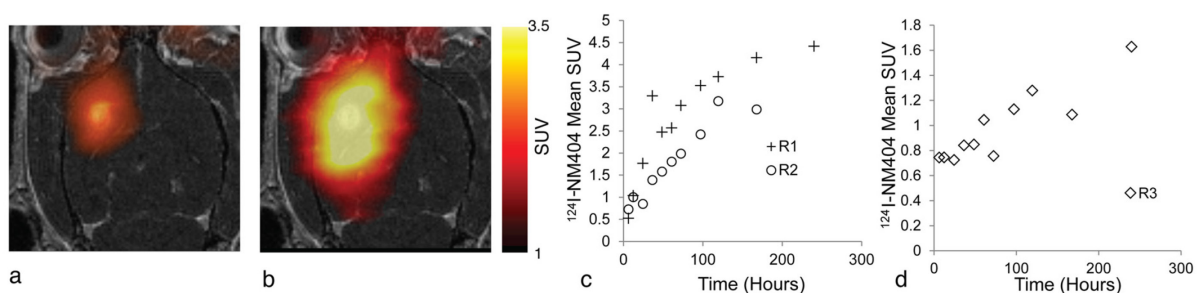


Figure C.3. Longitudinal uptake of [I-124]NM404. An example animal shows increased tumor uptake and size on the [I-124]NM404 PET image from 96 hours (a) to 240 hours (b) post-injection. Increasing tumor uptake over time was seen in all animals scanned up to 240 hours (c and d). Mean SUV is dependent on tumor size, likely due in part to volume averaging (c versus d).

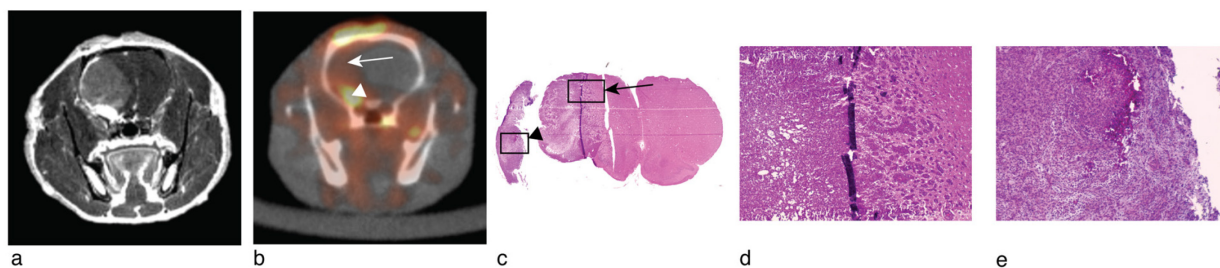


Figure C.4. Example histologic specimen. A representative tumor with regions of high and low gadolinium enhancement (a), and high and low ^{124}I -NM404 uptake (b). The histologic specimen shows that the region of low uptake is intraparenchymal with perivascular infiltration (arrow, d), and the region of high uptake is subarachnoid and has a more significant extracellular proteinaceous component (arrow head, e).

animals in groups 1 and 2 also show different pathologic characteristics. Tumors in group 1 had both sub-arachnoid and infiltrative intraparenchymal components, and tumors in group 2 were entirely intraparenchymal and were largely spherical with little infiltration.

C.4 Discussion and Conclusions

This appendix has presented data evaluating the uptake of [I-124]NM404 in an orthotopic rat glioma model. These results could provide useful information about the mechanism of [I-124]NM404 uptake in malignant brain tumors, and histopathological information that cannot be easily obtained from current trials involving human subjects.

In this orthotopic rat glioma model, regions with [I-124]NM404 uptake have a mean SUV that is correlated with gadolinium enhancement on MRI (Figure C.1). The maximum SUV of [F-18]FLT before [I-124]NM404 injection also shows a correlation with the maximum SUV of [I-124]NM404, though this does not reach statistical significance with the limited number of subjects studied (Figure C.2). Although gadolinium enhancement and [F-18]FLT uptake appear to correlate with [I-124]NM404 uptake, the distributions of these agents do not perfectly match. Thus, contrast enhanced MRI and [F-18]FLT PET may be useful for predicting [I-124]NM404

uptake, but [I-124]NM404 PET also gives information that cannot be obtained with the other modalities. The relationship between [I-124]NM404, [F-18]FLT, and gadolinium enhancement may also prove useful in determining the biological mechanism of [I-124]NM404 uptake in brain cancers. These preclinical results suggest how [I-124]NM404 might behave in human brain cancers, must this must be verified with ongoing clinical trials in humans.

The histology results give further insight into the cause of the variability of [I-124]NM404 uptake seen in the tumors studied. There appear to be morphologic differences between regions of high and low [I-124]NM404 uptake (Figure C.4). This implies that there are differences in the tumor environment in these regions. This observation must be confirmed by further study and a quantitative analysis of the histology results.

Finally, the continued uptake of [I-124]NM404 over the course of several days, including as the tumor grows (Figure C.3), might be a very useful characteristic for imaging and therapy with NM404. Continued uptake could be useful for monitoring tumor progression, or perhaps response to therapy, after a single injection of the agent. It is also a desirable trait for TRT with [I-131] or [I-125] labeled NM404, as the agent will continue to be taken up as cancer cells proliferate.

NM404 is a promising agent for evaluating and treating malignant brain tumors. This preclinical study provides insight into the uptake characteristics of NM404 in brain tumors, including characteristics that might prove useful, and characteristics that will require further investigation.

References

- Martin, S J, Eisenbarth, J A, Wagner-Utermann, U, Mier, W, Henze, M, Pritzkow, H, Haberkorn, U and Eisenhut, M 2002 A new precursor for the radiosynthesis of [18F]FLT *Nucl. Med. Biol.* **29** 2 263-73
- Nieder, C, Andratschke, N, Wiedenmann, N, Busch, R, Grosu, A L and Molls, M 2004a Radiotherapy for high-grade gliomas. Does altered fractionation improve the outcome? *Strahlenther. Onkol.* **180** 7 401-7
- Nieder, C, Grosu, A L, Mehta, M P, Andratschke, N and Molls, M 2004b Treatment of malignant gliomas: radiotherapy, chemotherapy and integration of new targeted agents *Expert Rev. Neurother* **4** 4 691-703
- Pinchuk, A N, Rampy, M A, Longino, M A, Skinner, R W, Gross, M D, Weichert, J P and Counsell, R E 2006 Synthesis and structure-activity relationship effects on the tumor avidity of radioiodinated phospholipid ether analogues *J. Med. Chem.* **49** 7 2155-65
- Pirotte, B *et al* 2006 Integrated positron emission tomography and magnetic resonance imaging-guided resection of brain tumors: a report of 103 consecutive procedures *J. Neurosurg.* **104** 2 238-53
- Pirotte, B J, Levivier, M, Goldman, S, Massager, N, Wikler, D, Dewitte, O, Bruneau, M, Rorive, S, David, P and Brotchi, J 2009 Positron emission tomography-guided volumetric resection of supratentorial high-grade gliomas: a survival analysis in 66 consecutive patients *Neurosurgery* **64** 3 471,81; discussion 481
- Stupp, R *et al* 2005 Radiotherapy plus concomitant and adjuvant temozolomide for glioblastoma *N. Engl. J. Med.* **352** 10 987-96
- Watanabe, M, Tanaka, R and Takeda, N 1992 Magnetic resonance imaging and histopathology of cerebral gliomas *Neuroradiology* **34** 6 463-9
- Wen, P Y *et al* 2010 Updated response assessment criteria for high-grade gliomas: response assessment in neuro-oncology working group *J. Clin. Oncol.* **28** 11 1963-72